Photofission of Heavy Nuclei from 0.2 to 3.8 GeV

By

Catalina Cetina

B.S. Physics, June 1981, University of Bucharest, Romania

M.S. Nuclear Physics, June 1982, University of Bucharest, Romania

A dissertation submitted to the faculty of

Columbian School of Arts and Sciences
The George Washington University

In partial satisfaction of the requirements for the degree of

Doctor of Philosophy

January 30, 2001

Dissertation directed by

Barry L. Berman

Professor of Physics

Abstract

Total photofission cross sections for ^{237}Np, ^{233}U, ^{235}U, ^{238}U, ^{232}Th, and ^{nat}Pb have been measured *simultaneously*, using tagged photons in the energy range $E_\gamma = 0.17$-3.84 GeV. This was the first experiment performed using the Photon Tagging Facility in Hall B at the Thomas Jefferson National Accelerator Facility. The fission fragments were detected using a novel kind of parallel-plate avalanche detector (PPAD), designed and built in the Nuclear Detector Laboratory of The George Washington University.

Our results show that ^{237}Np has the largest photofission cross section per nucleon, and that the photofission cross section for ^{238}U relative to that for ^{237}Np is about 80% over the entire energy range. This contradicts the general assumption that the photofission probability for uranium and all transuranic nuclei is equal to unity at these energies.

We also observe that the relative cross sections do not depend strongly on the incident photon energy over this entire energy range, suggesting a common mechanism responsible for the photofission process. The relative photofission cross sections per nucleon increase with the fissility parameter Z^2/A, approaching an asymptote at the Z^2/A value for ^{237}Np.

These results, together with the comparison of the ^{237}Np photofission cross section per nucleon with total photoabsorption data, indicate that the photofission probability for ^{237}Np is almost unity. If we make this assumption, we observe a significant shadowing of the interior nucleons by the ones on surface, starting below 1.5 GeV and decreasing to less than 80% near 4 GeV.

Contents

List of Tables

List of Figures

Part I

Motivation, Theory, and Experiment

Chapter 1

Physical Motivation

1.1 Introduction

The report of the official discovery of fission is generally considered to be the paper of Hahn and Strassmann [Hah39]. The new phenomenon was first interpreted in the framework of the liquid drop model by Meitner and Frisch [Meu39]. The first theoretical explanation of the mechanism of nuclear fission was presented shortly thereafter by Bohr and Wheeler [Boh39a].

As Bohr describes it [Boh39b], fission takes place in two separate stages. The first of these is "the formation of a compound nucleus in which the energy is stored in a way resembling the heat motion of a liquid or solid body: the second consists either in the release of this energy in a form of a radiation or in its conversion into a form suited to produce the disintegration of the compound nucleus. In the case of ordinary reactions, resulting in the emission of proton, neutron, or α-particle from the nucleus, we have to do with a concentration of a considerable part of the energy on some particle at the nuclear surface, sufficient for its escape, which resembles the evaporation of a molecule from a liquid drop. In the case of the fission phenomenon, the energy has to be largely converted into some special type of motion of the whole nucleus causing a deformation of the nuclear surface sufficiently large to lead to rupture of the nucleus, comparable to the division of a liquid drop into two droplets."

At excitation energies below the fission "threshold," the fission process proceeds via barrier penetration, and the energy dependence of the fission cross section in this energy region reflects the shape of the fission barrier [Kno82]. For actinide nuclei excited to energies above the fission barrier, competition occurs between fission and neutron and γ-emission ($B_F \approx B_n \approx$ 5-6 MeV). In the region of the giant dipole resonance (GDR), in the vicinity of about 12 MeV, the (γ, nF) and $(\gamma, 2n)$ processes become possible [Cal80a, Ber86], and already at 18 MeV second-chance fission (*i.e.* fission after the emission of a neutron) is as probable as first-chance fission [Cal80b]. Beginning with $E_\gamma \approx 50$ MeV and up to the pion-production threshold, the photon absorption is dominated by the quasideuteron mechanism [Rie84, Lep87]. This range of excitation energies was not explored in the present experiment.

As we saw, beginning with the GDR region, as higher-chance fission channels open, the total fission probability of heavy nuclei increases rapidly towards unity. It has been a common belief [Ahr84, Lep87, Fro92] that for uranium and transuranic isotopes and for incident photons above 50 MeV, the total photofission cross section $\sigma_{\gamma,F}$ exhausts the total photoabsorption cross section $\sigma_{\gamma,A}$. Therefore, photofission has been used to study the photon absorption process [Ber92], and $\sigma_{\gamma,F}$ has been used as a substitute for $\sigma_{\gamma,A}$, which is very difficult to measure by other methods for the case of high-Z nuclei.

The energy range available at Jefferson Lab begins in the Δ resonance region, where photoabsorption leads to the excitation of bound nucleons and continues up through the production of other baryon resonances. These resonances may behave quite differently inside the nuclear medium, compared with the case for free nucleons. Here, the cross section can be used to study possible modifications induced by the nuclear medium on the intrinsic properties of nucleons inside nuclei, including the interaction between the nucleons and their resonances in nuclei and the propagation of nucleon resonances inside nuclei.

Above the resonance region, the interaction between the incident photon and the target nucleus starts to resemble a hadronic process, the total cross section being almost energy independent. Similar to the situation encountered in the scattering of hadrons from nuclei, the incident photon will mainly interact with the nucleons situated on the nuclear surface, while the nuclear volume will be "shadowed." The onset of this effect is still under scrutiny and there is no good agreement between data and recent model predictions [Bia99].

1.2 Present status of the topic

1.2.1 Previous photofission measurements

For almost 50 years after the discovery of the fission phenomenon, particle-induced fission (especially neutron-induced fission) provided most of the available experimental information. Photon-induced fission reactions share the advantage of all photonuclear reactions of being initiated by the simple electromagnetic interaction. Moreover, weakly interacting probes, such as photons and electrons, allow the study of the photon absorption mechanism not only on the nuclear surface, but inside the nuclear volume as well. In spite of the advantages offered by electromagnetic probes, this weak interaction with the nucleus had its experimental drawbacks due to the difficulties in obtaining high fluxes of monochromatic photons using *e.g.* positron annihilation, Compton back-scattering, sharp (n,γ) lines, *etc.* Many of the past experiments used continuous energy photon beams (such as bremsstrahlung), implying the necessity of a complicated unfolding analysis procedure. This problem has been overcome by using the photon-tagging technique (see Sec. 3.3.1) at the new high duty-cycle electron accelerators.

In the actinide region of the periodic table, most of the new generation of photofission measurements were done for two of the uranium isotopes, ^{238}U and ^{235}U. For ^{238}U several sets of measurements have been done in the past two decades spanning the energy region from 50 MeV to 2.6 GeV. Older measurements were done at the Bonn 500-MeV synchrotron in the energy range E_γ = 120-460 MeV [Ahr84]. There are four data points for E_γ = 0.3-2.6 GeV from a Yerevan experiment [Ara90], but the precision and the number of these data points are not sufficient for a detailed analysis. Using a Compton back-scattered laser photon beam and low-pressure multiwire proportional chambers, a Novosibirsk group has produced $\sigma_{\gamma,F}$ results [Ilj92a] for E_γ = 60-240 MeV. At the 855-MeV Mainz Microtron (MAMI) [Fro92, Fro94], $\sigma_{\gamma,F}$ has been measured for E_γ = 50-800 MeV using tagged photons and a 4π array of position-sensitive fragment detectors. The fragment mass distributions also were determined in this experiment via the time-of-flight technique. At Frascati [Bia93a], measurements were carried out with the Jet-Target tagged-photon beam for E_γ = 0.2-1.2 GeV. The PPADs used to detect the fission fragments had the target material deposited on one of the electrodes.

For ^{235}U, the Bonn experiment [Ahr84] had several targets in the beam line at the same time as the ^{238}U targets. The Yerevan experiment [Ara90] gives $\sigma_{\gamma,F}$ results for E_γ = 0.3-3.3 GeV, but again with low precision. The other set of data for this isotope comes from Mainz [Fro94] and spans the same energy region as for ^{238}U.

For both previously discussed uranium isotopes, we have made simultaneous measurements in our photofission experiment at the Saskatchewan Accelerator Laboratory (SAL) [San00b] for E_γ = 60-260 MeV. The fission-fragment detectors used in this lower-energy experiment are the same as the ones used in the Jefferson Lab experiment reported here. For ^{238}U and ^{235}U, the data from all of the previously mentioned experiments are presented in Fig. 1.1. During the SAL experiment we also measured a third uranium isotope, namely, ^{233}U.

In the Novosibirsk experiment [Ilj92a], measurements were done simultaneously for ^{237}Np and ^{238}U. These are the only existing photofission results for ^{237}Np, besides the SAL ones. Both experiments agreed in measuring a higher photofission cross section per nucleon for ^{237}Np, compared with ^{238}U, as shown in Fig. 1.2.

As for ^{232}Th, the only existing results besides the SAL ones come from the photofission experiment at Frascati [Bia93b], and here too, measurements were done simultaneously for ^{238}U and ^{232}Th. Thorium, an actinide nucleus with Z only two units below uranium, has a fission cross section only 70% of that for uranium, as one can see in Fig. 1.3.

Photofission of ^{nat}Pb has been studied only in our SAL experiment, for E_γ = 120-

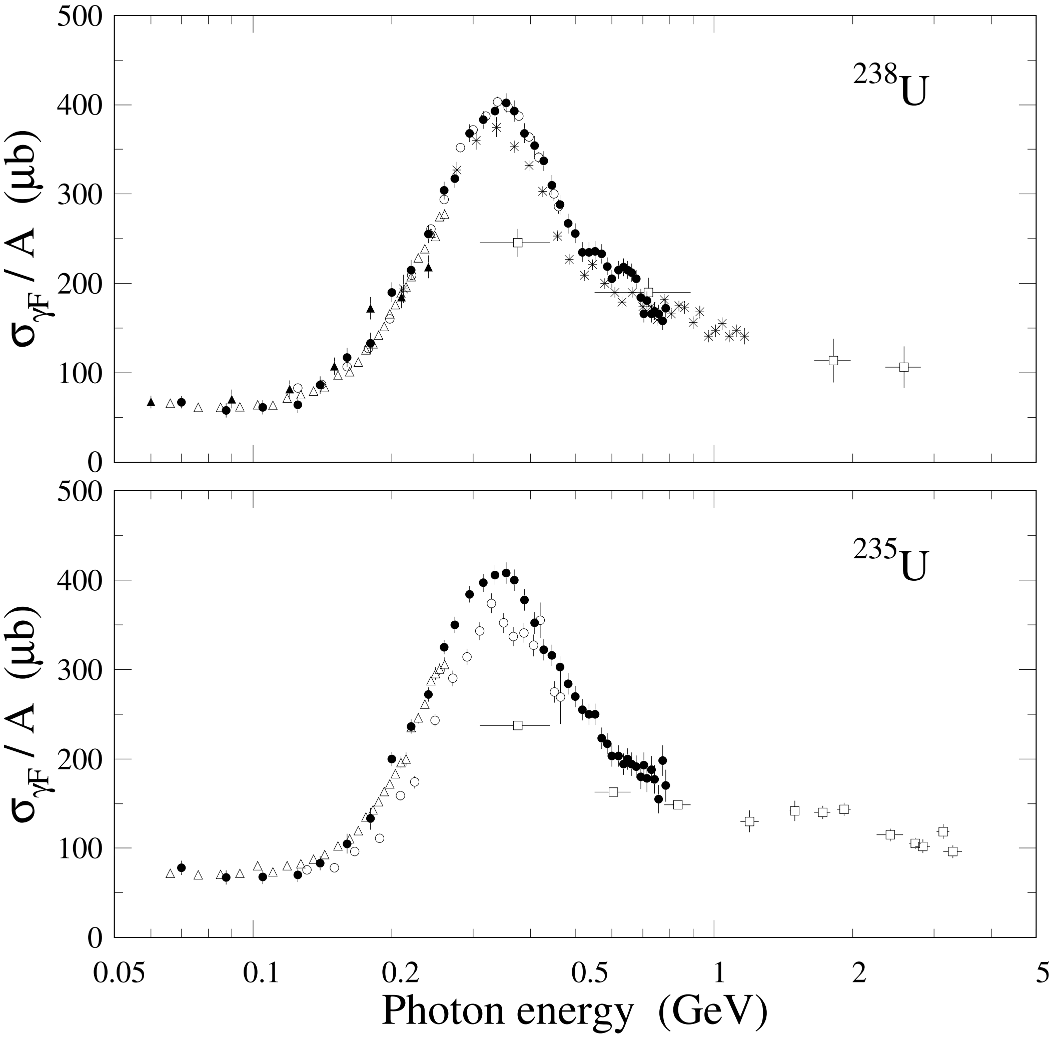

Figure 1.1: Previous photofission data for ^{238}U and ^{235}U: ($\triangle$) [San00b], (closed triangles) [Ilj92a], ($\circ$) [Ahr84], ($\bullet$) [Fro94], ($\square$) [Ara90], and ($*$) [Bia93a].

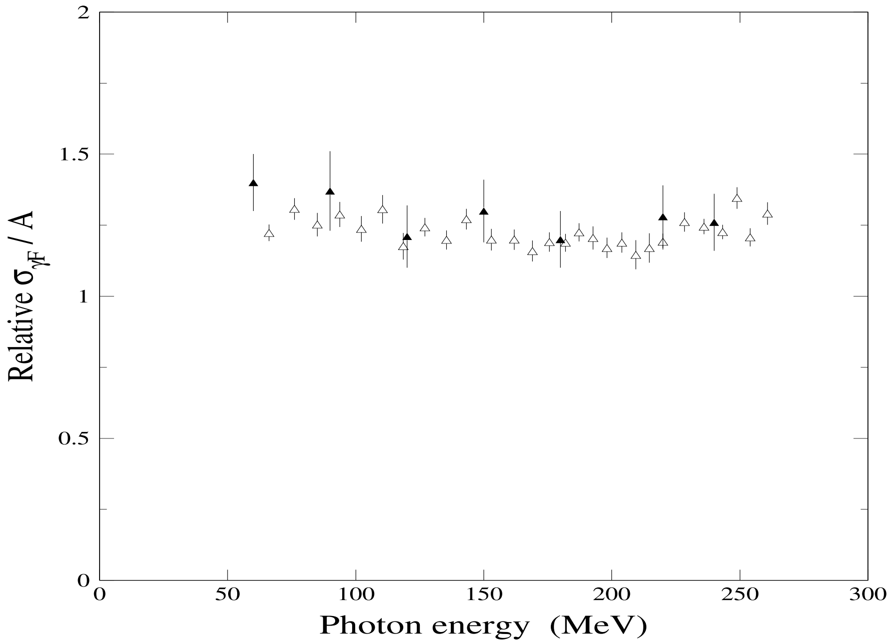

Figure 1.2: Photofission cross section per nucleon for ^{237}Np relative to ^{238}U: (open triangles) [San00b], (closed triangles) [Ilj92a].

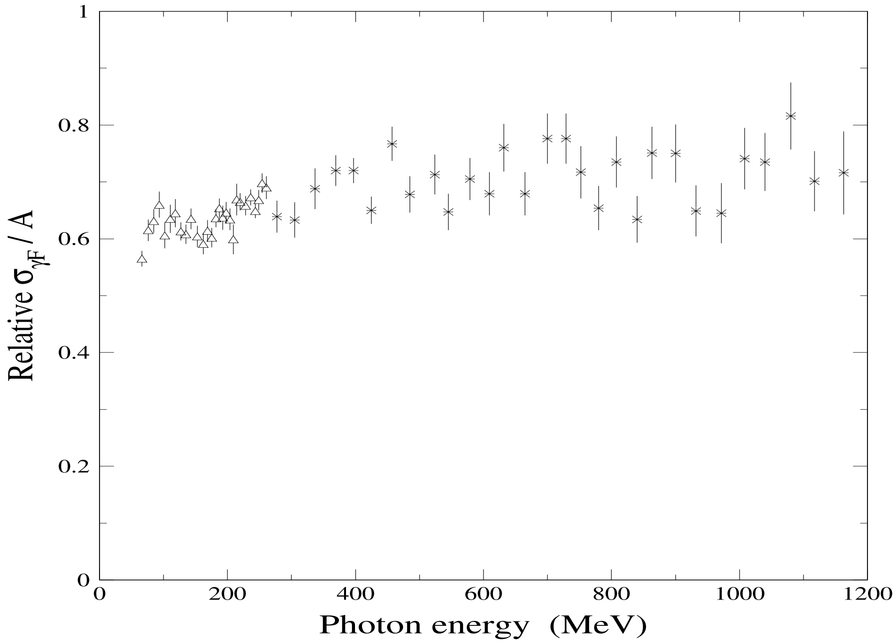

Figure 1.3: Photofission cross section per nucleon for ^{232}Th relative to ^{238}U: ($\triangle$) [San00b], ($*$) [Arr95].

220 MeV. Additionally, data were obtained by deconvolution of inclusive electrofission data [Arr90], but the uncertainty in the unfolding procedure makes these data less reliable. There is photofission data for Bi [Gua87] and Au [Luc89] in the energy range 100-300 MeV, and for both nuclei the fission cross sections are monotonically increasing functions of incident photon energy.

Thus, if we exclude the Yerevan data as inconclusive, we can say that the previous existing photofission data go up to 1.2 GeV for ^{238}U and ^{232}Th, up to 800 MeV for ^{235}U, up to 260 MeV for ^{233}U and ^{237}Np, and up to 220 MeV for ^{nat}Pb, as summarized in Table 1.1. The present experiment extends the photofission measurements for all six of these nuclei up to 3.8 GeV.

Isotope	E_γ^{max} (MeV)
^{238}U, ^{232}Th	1200
^{235}U	800
^{233}U, ^{237}Np	260
^{nat}Pb	220

Table 1.1: Maximum photon energies for the previously existing photofission data, excluding those of Ref. [Ara90].

1.2.2 Comparison with photoabsorption data

Without attempting a comprehensive presentation of the existing photoabsorption data, we will show the results from the most recent experiments and will discuss some aspects in the resonance region and above.

Above the pion threshold, the absolute cross section $\sigma_{\gamma,A}$ is dominated by the transition to the first excited state of the nucleon, the Δ resonance $P_{33}(1232)$, located about 300 MeV above the nucleon ground state. In this energy region, several sets of measurements for various nuclei ranging from lithium to uranium have been done, using different experimental techniques, such as detection of the outgoing hadrons, measurement of the neutron multiplicities, transmission, and photofission. For all of the nuclei studied, a resonance-like cross section has been observed. Moreover, the cross sections scaled by the mass number have a very similar behavior, following the so-called “universal curve” [Mac97]. However, even without taking into account the systematic uncertainties, the results of different experiments vary by at least 10%.

While $\sigma_{\gamma,A}/\mathrm{A}$ is almost independent of A for A$\geq$6, it differs clearly from the proton, as we can see in Fig. 1.4. The decrease and broadening of the cross section have been explained within 10% in the framework of the Δ-hole model [Car92], taking into account the propagation of the Δ isobar in the nuclear medium. Other contributing

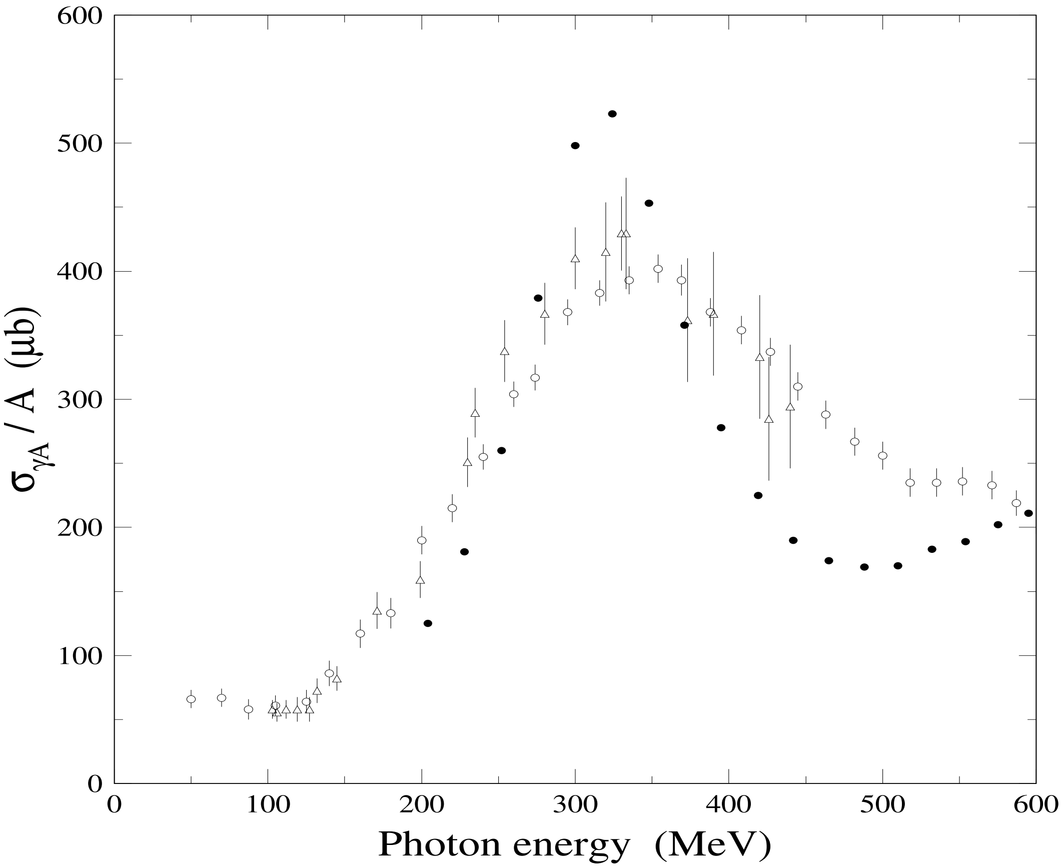

Figure 1.4: Photoabsorption data in the Δ resonance region for the proton ($\bullet$) [Mac96] and Pb ($\triangle$) [Car84]. Photofission data for ^{238}U ($\circ$) [Fro94] in the same energy region.

effects include the Fermi motion (which suppresses the peak height and increases the width of the resonance), the Pauli blocking (which has the opposite effect of reducing the resonance width by decreasing the phase space available for the resonance decay products), and possibly the partial deconfinement of quarks in nuclei (which can reduce the strength of nucleon resonances) [Bia96, Gia94], although the existence of this last effect is controversial.

While the Δ resonance is only slightly distorted by the nuclear medium, higher excited-nucleon states are completely washed out. The D_{13} and F_{15} resonances, clearly seen in the photoabsorption on the proton and the deuteron [Arm72], and still seen in ^{3}He [Mac96], are not observed in total cross sections for A$\geq$4 nuclei [Ang93, Fro94,

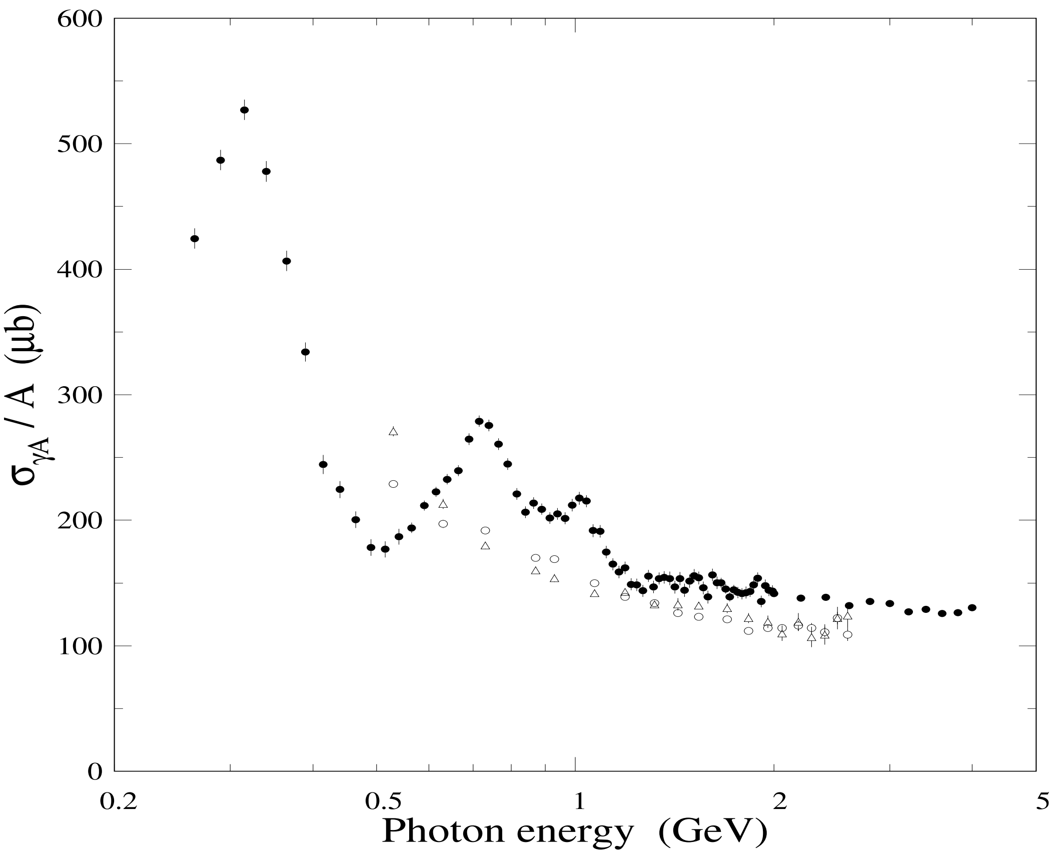

Figure 1.5: Photoabsorption data in the higher-resonance region for the proton (●) [Arm72], C (○) and Pb (△) [Muc99].

Bia96, Mac97, Muc99]. In Fig. 1.5 we present data from the recent Bonn experiment [Muc99], where the total photoabsorption cross section was measured for C, Al, Cu, Sn, and Pb in the energy range 0.5-2.6 GeV, using the hadron-detection technique.

Above the nucleon-resonance region the nuclear photoabsorption cross section appears to be structureless and slowly decreasing with energy. The reduction in the nonresonant cross section relative to the proton for high-energy photons interacting with nuclei is known as the "shadowing effect" [Wei74]. This effect is generally described by considering the photon to be a superposition of a bare photon and a hadronic fluctuation with the same quantum numbers ($J^{PC} = 1^{--}$). It is assumed that the photon fluctuates into a quark-antiquark pair which can manifest itself as a vector meson. The fluctuation lifetime (or the fluctuation length λ) depends on the incident photon energy and on the mass of the vector meson $\lambda \sim 2E_\gamma/m_{VM}^2$, so that the fluctuation length becomes comparable to nuclear dimensions for high enough photon energies (for a ρ meson and for $E_\gamma = 4\ GeV$, $\lambda \approx 3\ fm$).

Within this model the shadowing is produced by coherent multiple scattering of the hadronic intermediate state on different nucleons inside the nucleus. In vector-meson dominance (VMD) models [Bro69, Got69], the hadronic component of the photon is given by the low-mass vector mesons ρ, ω, and ϕ, while generalized vector-meson dominance (GVMD) models [Dis76, Sha96] include higher-mass vector mesons as well as excited vector-meson states, which also contribute to the nucleon collisions. The GVMD predictions seem to be closer to the experimental data below 3 GeV [Bia99].

Since the hadronic behavior of the photon results in greatly increased interaction strength for the photon with hadronic matter, shadowing in nuclei manifests itself as the total absorption cross section gradually evolves from purely volume absorption ($\propto A$) towards purely surface absorption ($\propto A^{2/3}$). The shadowing effect can be evaluated quantitatively by use of the expression

$$\frac{A_{eff}}{A} = \frac{\sigma_{\gamma A}}{(Z\sigma_{\gamma p} + N\sigma_{\gamma n})}$$

where A_{eff} represents the effective number of nucleons seen by the incident photon, while $\sigma_{\gamma p}$ and $\sigma_{\gamma n}$ are the free-nucleon photoabsorption cross sections for the proton and neutron, respectively. Earlier experiments [Bro73, Mic77] found values of $A_{eff}/A \leq 1$ starting around 2 GeV and decreasing with increasing energy. The recent Bonn experiment [Muc99] gives the A_{eff} dependence between 0.5 and 2.6 GeV for C, Al, Cu, Sn, and Pb shown in Fig. 1.6, indicating a low-energy onset of the shadowing effect (as low as 1 GeV). Recent calculations [Fal00] agree with these results.

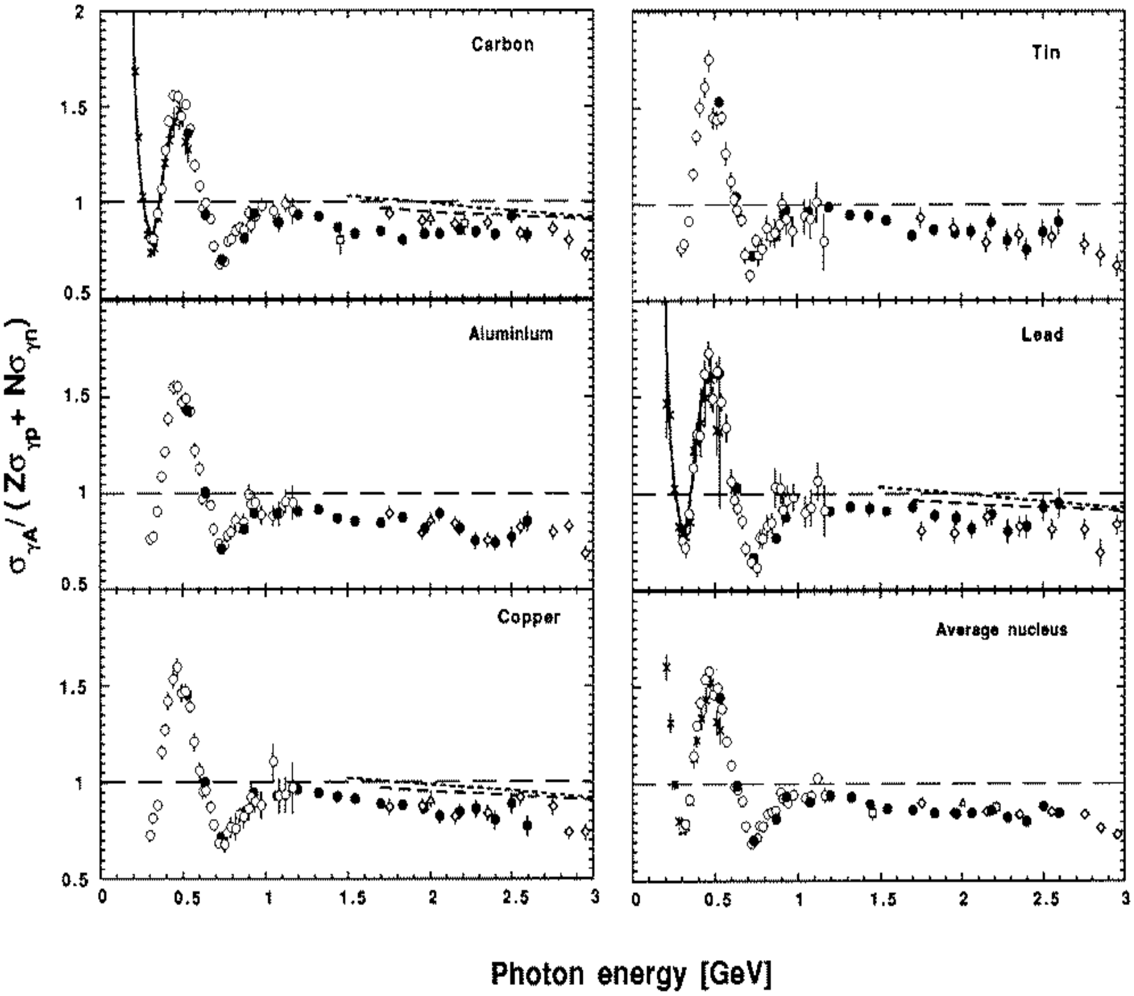

Figure 1.6: Ratios of photonuclear to photonucleon absorption cross section for C, Al, Cu, Sn, and Pb (•)[Muc99], (○)[Bia96], (∗)[Car85], (△)[Mic77], (◇)[Bro73], (□)[Hey71]. Solid line is a Δ-hole model calculation [Car92], dashed [Pil95] and dotted [Bof96] are two VMD predictions.

1.3 Goals and significance

By analyzing the photofission cross section of heavy nuclei in the few-GeV energy region, we aim not only at extracting new physics, but at bringing more information related to interesting and sometimes controversial existing lower-energy results, as well as checking their validity at higher photon energies. On one hand, there are issues related to the fission process itself; on the other hand, the microscopic mechanism governing photoabsorption at these energies is not completely understood.

1.3.1 Photofission and photofissility

From the photofission point of view, the main question we are asking is whether at the energies available at Jefferson Lab the photofission cross section $\sigma_{\gamma,F}$ for uranium and transuranic isotopes exhausts the total photoabsorption cross section $\sigma_{\gamma,A}$. If we define the *photofissility* W_F of a nucleus as the probability that this nucleus undergoes fission, then we can express W_F as the ratio

$$W_F = \frac{\sigma_{\gamma F}}{\sigma_{\gamma A}} \,. \tag{1.1}$$

For nuclei $Z \geq 3$, the concept of "universal behavior" [Mac97], or A-independent $\sigma_{\gamma,A}/A$, implies that, for two nuclei, the ratio of their photofissilities is given by the ratio of their photofission cross sections per nucleon

$$\frac{(W_F)_1}{(W_F)_2} = \frac{(\sigma_{\gamma F}/A)_1}{(\sigma_{\gamma F}/A)_2} \tag{1.2}$$

As was said before, it has long been assumed [Ahr84, Lep87, Fro92] that for uranium and transuranic isotopes $\sigma_{\gamma,F} \simeq \sigma_{\gamma,A}$ for $E_\gamma \geq \; 50 \; MeV$. However, the assumption $W_F \simeq 1$ had to be reconsidered after the Novosibirsk group reported that the fission cross section per nucleon for ^{237}Np is about 30% higher than that for ^{238}U up to 240 MeV. The subsequent SAL measurements corroborated these results in the same energy range. The validity of this trend up to the GeV region is not a trivial assumption; this experimental study represents an important goal of the present experiment. If it is true, then the photofissility of uranium is less than unity, which invalidates the use of the photofission cross section alone to determine the total photoabsorption cross section.

Moreover, as we saw in the previous section, there are differences in the literature for the fission cross sections of various uranium isotopes. As for all nuclei, one can assume that these differences are largely due to different values of the fissility parameter Z^2/A. The present experiment evaluates the differences among three uranium isotopes, neptunium, thorium, and lead, over a wide range of photon energies. This addresses the question of whether there is a Z^2/A scaling of the fission probability and whether it is photon energy dependent.

^{232}Th is an actinide nucleus with a fissility parameter $Z^2/A \approx$ 35. Thorium lies in the transition region between the preactinide nuclei (with $Z^2/A < 35$ and single-humped high fission barriers of 25-30 MeV), and heavier actinide nuclei (with $Z^2/A >$ 35 and double-humped low fission barriers of 5-6 MeV). The existing measurements show a fissility for ^{232}Th relative to ^{238}U slowly increasing from about 0.6 at 100 MeV to almost 0.8 at 1200 MeV. The present measurements can tell whether the fission probability of thorium relative to heavier nuclei saturates in the GeV energy region, and what its asymptotic value would be.

The same is true for lead. For the preactinide nuclei, due to their higher fission thresholds, the fissility is a strong function of the excitation energy, and consequently it is more directly related to the photoexcitation process. The SAL data show values of the lead fissility relative to neptunium increasing from 0.015 at 120 MeV to almost 0.035 at 220 MeV. As for thorium, we ask what are the values of this relative fissility up to 4 GeV, and whether it becomes energy independent or not. Additionally, since there are recent measurements of the total photoabsorption for lead up to 2.5 GeV, we will be able to determine the photofissility for lead up to this energy.

1.3.2 The photoabsorption mechanism

The interest in photofission studies in the intermediate-energy region is also due to the fact that the photofission process is related to the absorption and excitation mechanism of nuclei by photons, as well as to the subsequent process of nuclear deexcitation. Intermediate-energy photons ($\sim$ 1 GeV) interact mainly with single nucleons in the nucleus. On the other hand, fission is a collective process of the nucleus. Thus, photofission studies can yield information about the propagation of a local excitation in nuclear matter and its transfer to collective nuclear excitation. Interesting studies will be possible by comparing our data with the predictions of the intranuclear cascade evaporation model, generally used to describe intermediate-energy photoreactions, and which will be outlined in the next chapter.

In the Δ-resonance region, as mentioned in the previous section, there are many sets of experimental data, interpreted in a satisfactory way using the Δ-hole model. The absence of the higher D_{13} and F_{15} resonances has recently been confirmed experimentally for C, Al, Cu, Sn, Pb [Bia96], Th [Bia93b], and U [Bia93a, Fro94]. The new experimental information to be obtained from the present experiment is the cross section for ^{237}Np. Its photofission cross section is probably close if not equal to the photoabsorption cross section. A more definite answer will be given by comparing $\sigma_{\gamma,F}/A$ for ^{237}Np with the bulk of photoabsorption data on other nuclei.

Experimental results regarding the shadowing effect in heavy nuclei will also be forthcoming. Both the onset of the shadowing effect and its energy dependence up to 4 GeV will be addressed. Absolute values are to be extracted for neptunium, if its cross section is a close approximation to the total absorption cross section. For the other nuclei, the fission cross section is scaled by the values of their relative fissilities.

Chapter 2

Theoretical Aspects

2.1 A model of the fission reaction mechanism

The experimental photofission results can be compared with intranuclear-cascade (INC) and statistical-deexcitation model calculations. This two-step picture of the fission reaction mechanism was first suggested by Bohr and Wheeler [Boh39b], and later confirmed using evidence from compound-nucleus studies, as well as medium-energy heavy-ion reactions [Gav87, Eck90]. A schematic representation is given in Fig 2.1 and the explanations follow below.

Photon absorption and intranuclear cascade

Below the pion threshold, the first stage of the reaction mechanism has been explained using precompound-decay models [Bla83, Bla75, Gri66]. For higher energies the foundation of the INC model and details of the calculation are given in Refs. [Ilj94, Ilj97]. The absorption of photons by nuclei is assumed to generate a cascade of sequential two-body collisions of fast particles with nucleons. High-energy products of these collisions (nucleons, pions, *etc.*) mostly escape from the nucleus, carrying away both energy and charge. The low-energy particles are trapped by the nuclear potential. This stage of the INC development is fast, the cascade time τ_{cas} being of the order of magnitude of τ_0, the time needed for a fast particle to cross the nucleus ($\tau_0 < 10^{-22}$ s).

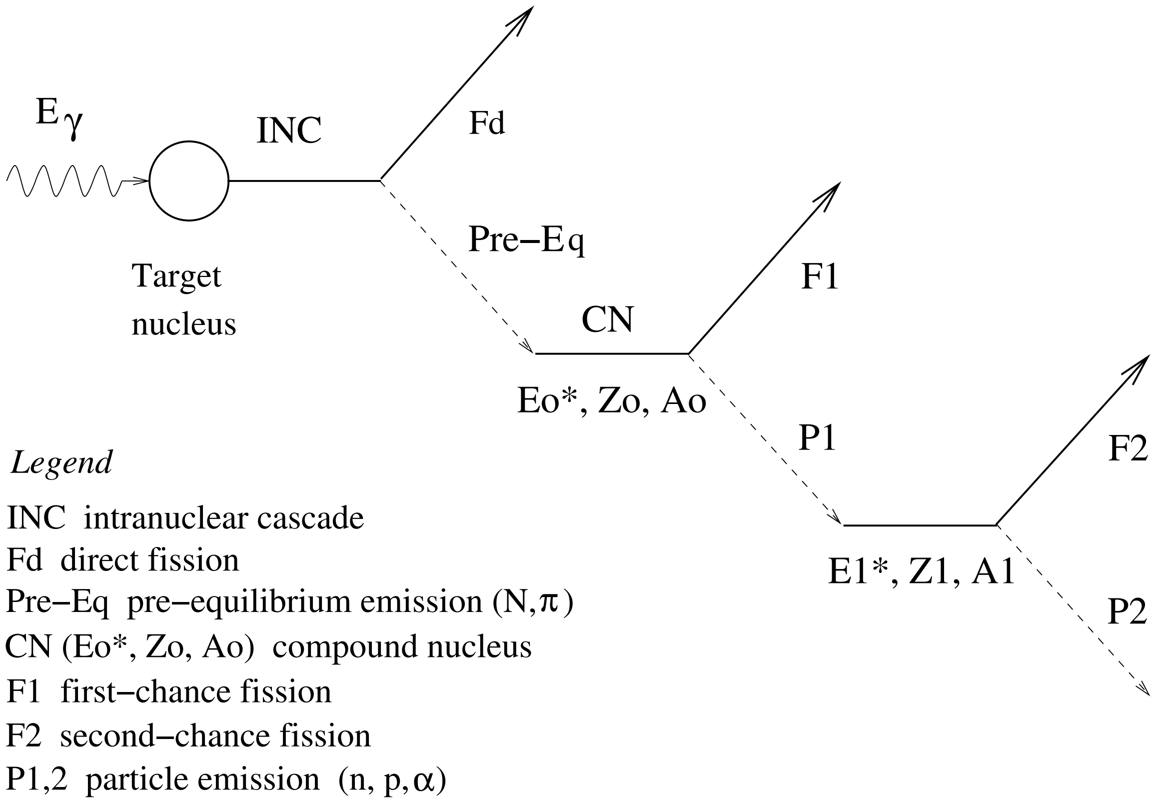

Figure 2.1: Schematic representation of the fission reaction mechanism. The photon absorption in the target nucleus generates an intranuclear cascade (INC) followed by pre-equilibrium particle emission (Pre-Eq) and formation of an excited compound nucleus (CN), which decays by particle emission (P1, P2, *etc.*) and/or fission (F1, F2, *etc.*).

For photonuclear reactions at GeV energies the INC model describes the elementary γN interaction by taking into account the following processes:

a. the resonant contribution from two-body channels with production of baryon B^* and meson M^* resonances

$$\begin{aligned} \gamma N &\rightarrow \pi\, B^* \\ \gamma N &\rightarrow N M^* \end{aligned}$$

(the lower $\gamma N \rightarrow B^* M^*$ cross section being neglected);

b. the nonresonant statistical contribution from many-body channels

$$\gamma N \to i\pi N,\ 2 \le i \le 8.$$

The pions, nucleons, and η, ρ, ω mesons produced in γN interactions are allowed to undergo rescattering and absorption in the nucleus. The production of a multipion system inside the nucleus is a specific feature of photonuclear reactions at high energies. Fast INC pions can knock out nucleons, so that the slower nucleons pass through a lower-density nuclear region, undergoing less scattering (the so-called "trawling effect"). This makes it necessary to take into account local depletion of nuclear density during the development of the cascade.

In the INC model, the solution of the kinetic equation with the many-body distribution function describing the hadron transport in a nuclear medium is calculated by a numerical (Monte-Carlo) method. It includes the cascade shower and determines the yield of residual nuclei $Y_0(A_0, Z_0, E_0^*, \mathbf{P_0})$, where A_0 and Z_0 are the number of nucleons and protons of the residual nucleus, and E_0^* and $\mathbf{P_0}$ are its excitation energy and momentum respectively. Some interesting features of the residual nuclei are the broad distributions of A_0, Z_0, E_0^*, and $\mathbf{P_0}$ [Hof94], due to particle fluctuations in the cascade flow.

Evaporation cascade

After the INC, it takes an additional time τ_{eq} until quasi-thermodynamic equilibrium is reached in the residual nucleus; typically $\tau_{eq} \approx 5 - 10\tau_0$ [Bun80].

In the last, slow stage ($\tau_{ev} \gg \tau_0$), the compound nucleus successively evaporates particles or undergoes fission. Fission involves rearrangement of the nuclear structure and therefore is a relatively slow process, with fission time $\tau_f \ge 10^{-20}$ s [Spe83].

The deexcitation of the highly excited compound nucleus is described using a statistical-evaporation model [Ilj92b], and the calculations employ the Monte-Carlo method. In this model, competition between different decay channels in each step of the evaporation chain is determined by the partial widths for fission Γ_f or for emission of particles Γ_j, where the emitted particle can be of any kind j, with $j = n, p, \alpha, \gamma$. The decay widths Γ_f and Γ_j are in turn expressed in terms of the nuclear level densities, which are the most important quantities of the model:

$$\Gamma_f = \frac{1}{2\pi} \frac{1}{\rho_0(E^*)} \int_0^{E^*-B_f} \rho_f(E^* - B_f - E)\, dE \tag{2.1}$$

and

$$\Gamma_j = \frac{g_j m_j}{(\pi\hbar)^2} \frac{1}{\rho_0(E^*)} \int_{V_j}^{E^*-B_f} \sigma_{inv}(E) \rho_j(E^* - B_f - E)\, EdE. \tag{2.2}$$

In Eqs. 2.1 and 2.2, ρ_0, ρ_f, and ρ_j are the level densities of the compound nucleus, the nucleus at the top of the fission barrier (saddle point), and the nucleus produced after emission of particle j, respectively; B_f is the fission-barrier height; g_j, m_j, V_j, and B_j are the spin factor, mass, Coulomb barrier, and binding energy of particle j, respectively; $\sigma_{inv}(E)$ is the cross section of the inverse reaction for absorption of the particle with energy E.

The nuclear level densities are in turn given by the Fermi gas expression, taking into account the collective and pairing effects, as well as the thermal damping of shell effects in the nuclear level density.

$$\rho(E^*) = \frac{\sqrt{\pi}}{12} \frac{k_{rot}\, k_{vib}}{a^{1/4}(E^* - \Delta)^{5/4}}\, exp\Big[2\sqrt{a(E^* - \Delta)}\Big], \tag{2.3}$$

where k_{rot} and k_{vib} are the coefficients of rotational and vibrational enhancement of the nuclear level densities and Δ is the pairing energy. The level-density parameter a depends on the shell correction in the nuclear mass formula $\delta W_g(N, Z)$ and on the excitation energy E^*

$$a(E^*, Z, N) = \tilde{a}(A) \left[1 + \delta W_g(N, Z) \frac{f(E^* - \Delta)}{E^* - \Delta}\right], \tag{2.4}$$

where $\tilde{a}$ is the asymptotic Fermi-gas value of the level-density parameter at high excitation energy, and $f(x) = 1 - exp(-cx)$ with c=const [Ign75].

The parameters in Eqs. 2.3 and 2.4 are fixed according to the analysis of the total bulk of data on level densities, decay widths, and lifetimes of excited compound nuclei [Ilj92b]. The free parameter of the model is the ratio a_f/a_n of the asymptotic values of the level density parameter a_f at the fission saddle point and the a_n for the neutron-emission channel. The values for the parameter r range between 1.05 and ~1.30 [Van73]. Using low-energy data, different linear relationships were found between $r = a_f/a_n$ and the fissility parameter Z^2/A, for different ranges of Z^2/A [Mar90].

Fission of the compound nucleus

The dynamics of the descent of highly excited fissioning nuclei from saddle point (or the top of the fission barrier) to scission point is described by the diffusion model developed in Ref. [Ade88]. The fission process is described in the diffusion model by a small number of collective degrees of freedom which interact with the heat bath formed by the remaining single-particle degrees of freedom. The basic dynamical equation of this model is the Fokker-Planck equation for the distribution function of collective coordinates and conjugate momenta, which is the distribution of the observables of the fission process. The distribution function is assumed to have a Gaussian form, and the coefficients are given by the tensors of inertia, friction, and diffusion.

The diffusion model allows one to calculate the yield $Y(E_k, A)$ of fission fragments as a function of kinetic energy E_k and mass number A. The one-dimensional energy $Y(E_k)$ and mass $Y(A)$ distributions are approximated rather well by Gaussians [Ade88].

Multifragmentation of the hot compound nucleus

For excitation energies $E^* \geq\ 2-3$ MeV/nucleon, the fission-evaporation decay mechanism of the compound nucleus starts to give way to other decay processes. Up to energies $E^* \approx\ 2-3$ MeV/nucleon, breakup into a small number (2-4) of fragments plays the dominant role. Significant contributions come from "quasievaporation" (breakup into a large residual nucleus and one or two light clusters) and from "quasifission" (breakup into two fragments with comparable masses and one or two light clusters). When the excitation of the nucleus gets close to its total binding energy ($E^* \geq\ 2-3$ MeV/nucleon), an explosion-like process dominates, leading to the total disintegration of the nucleus and the emission of multiple nuclear fragments of various masses.

Nuclear multifragmentation is described by several models [Bon95]. The statistical approach [Bot90, Bon95] is based on the idea that at high excitation energies, when a large number of degrees of freedom is involved, the probabilities of different decay channels are mainly determined by statistical weight rather than by the detailed dynamics of the process. In addition to its simplicity, the statistical model has the advantage of generalizing the concept of a compound nucleus and liquid-drop description to the case of highly excited nuclei. Thus, the evaporation-fission and the fragmentation mechanisms can be treated on a similar basis. The predictions of the cascade-fragmentation-evaporation model have been successfully compared with mass spectra of fragments produced in proton-nucleus collisions in the proton energy range 1.0-11.5 GeV [Bot88].

2.2 The photofission cross section

The photofission cross section $\sigma_{\gamma F}$ is the simplest integral characteristic of the fission process. Its ratio to the total photoabsorption cross section $\sigma_{\gamma A}$ represents the probability that a nucleus will undergo fission, and it is called the photofissility W_F.

Within the framework of the two-stage description which forms the basis for the INC-evaporation model, assuming that the events in the decay chain occur independently and without quantum interference, we can express the fission cross section

$$\sigma_{\gamma F} = \sum_{A_c} \sum_{Z_c} \sum_{I} \int \sigma_{CN}(A_c, Z_c, E^*, I)\ P_F(A_c, Z_c, E^*, I)\ dE^* \ , \tag{2.5}$$

where σ_{CN} is the cross section for formation of a compound nucleus which has A_c

nucleons, Z_c protons, the excitation energy in the interval $(E^*,\ E^* + dE^*)$, and angular momentum I. P_F is the probability that this compound nucleus undergoes fission during a transition from an excited state to the ground state, and it is given by the expression

$$P_F = \sum_k \ P_k(E^*)\ P_k^F(A_c, Z_c, E^*, I)\ , \tag{2.6}$$

where P_k is the probability that the compound nucleus emits k particles as it passes to the ground state, and P_k^F is the probability that, in this process, the fission takes place in any link of the evaporation chain. This in turn is given by

$$P_k^F = 1 - \prod_{i=1}^{k} \left[1 - \frac{\Gamma_F(A_i, Z_i, E_i^*, I_i)}{\sum_j \Gamma_j(A_i, Z_i, E_i^*, I_i)}\right]\ , \tag{2.7}$$

where i denotes a given link in the evaporation chain; $j = F, n, p, \alpha$, and Γ_F and Γ_j are the decay widths for fission and particle emission, as defined and expressed in the previous section.

These expressions, together with the INC calculations of Iljinov and Mebel were used to calculate the fissilities for various reactions, induced not only by photons, but also by protons, pions, and stopped antiprotons. Some of these results are shown in Fig. 2.2 [Ilj94], proving that the cascade-evaporation model gives a unified description of a large number of data on the fissility of nuclei excited by various intermediate-energy particles (p, π, γ, $\bar{p}$, and α).

The same formalism was used for ^{232}Th and ^{238}U in the photon energy range $E_\gamma = 60 - 1200\ MeV$ [Arr95]. It is interesting to note that their results show that for photon energies above about 200 MeV, the fission probability of all the compound nuclei formed from the two actinide target nuclei *saturates*, that is

$$P_F(A_c, Z_c, E^*, I)\ \rightarrow\ 1\ , \tag{2.8}$$

so that the photofission cross section will be given essentially by the sum over all possible compound nuclei. This means that at intermediate energies, the magnitude and the energy dependence of the photofissility of actinide nuclei is mainly determined

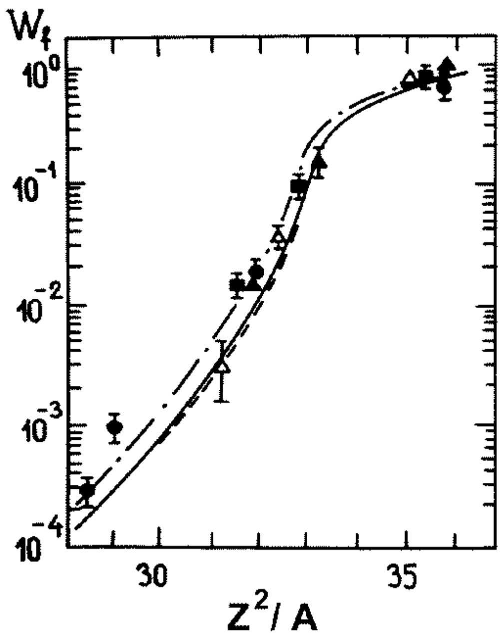

Figure 2.2: Calculated and experimental fissilities ([Ilj89] and references therein) for heavy nuclei in interaction with 200-MeV photons (dash-dotted line and closed squares), 190-MeV protons (solid line and closed circles), 80-MeV π^+ (closed triangles) and π^- (open triangles) mesons (dashed line).

by the equilibration process leading to compound-nucleus formation. Furthermore, following the formalism developed by Kituchi and Kawai [Kit68], the authors [Arr95] find for photonuclear reactions an expression for the photofissility W_F^{CN} corresponding to compound-nucleus formation

$$W_F^{CN}(E_\gamma) \cong C \frac{E^*}{E_\gamma} , \qquad (2.9)$$

where C=C(A,Z) is a parameter with almost no energy dependence. The existing photofission data seem to indicate an almost energy-independent fissility for photon energies above 300 MeV. Thus, provided that the Kituchi-Kawai formalism is correct and still valid at GeV energies, the ratio E^*/E_γ should also be almost constant under the above-mentioned conditions.

Chapter 3

Experimental Aspects

3.1 Introduction

The experimental data reported in this thesis were collected during the first measurements performed in Hall B at the Thomas Jefferson National Accelerator Facility (Jefferson Lab) using the photon-tagging facility. The experiment served as the commissioning experiment for the Photon Tagger. The experimental run took place in April 1998 and used approximately 200 hours of beam time, out of which ~110 hours were available for data-taking (see Fig. 5.1). The experiment consisted of measuring the absolute photofission cross section for six different nuclei: ^{237}Np, ^{233}U, ^{235}U, ^{238}U, ^{232}Th, and ^{nat}Pb. One of the two fission fragments produced by the interaction of an incident photon with one of the target nuclei was detected using a novel kind of anode-grid parallel-plate avalanche detector (PPAD). The PPADs were designed, built, and tested at GW. Data for the six nuclei were collected *simultaneously*, allowing a very reliable comparison among them. The experiment also represents a continuation of the photofission measurements done by the GW group at SAL in January-February 1997 [San00b] using the same fission-fragment detectors.

3.2 The electron beam

The Continuous Electron Beam Accelerator Facility (CEBAF) at Jefferson Lab is a superconducting recirculating electron accelerator with a duty factor of 100%. The accelerator consists of two parallel linear accelerators (LINACs) connected by semi-circular bending sections, such that the whole accelerator tunnel is racetrack-shaped and almost a mile long (see Fig. 3.1). The linear sections provide an acceleration up to 0.6 GeV over a 80-m effective length, while the 9 semicircular sections allow for passing the electron beam through the LINACs up to five times, increasing its energy up to 6 GeV. The accelerator uses superconducting niobium RF cavities to produce the electric field that accelerates the electron beam. With a high duty factor and high intensities (up to 200 μA), CEBAF can presently provide electron beam energies between 0.8 and 6 GeV. By using more superconducting cavities, an upgrade to 12 GeV is proposed.

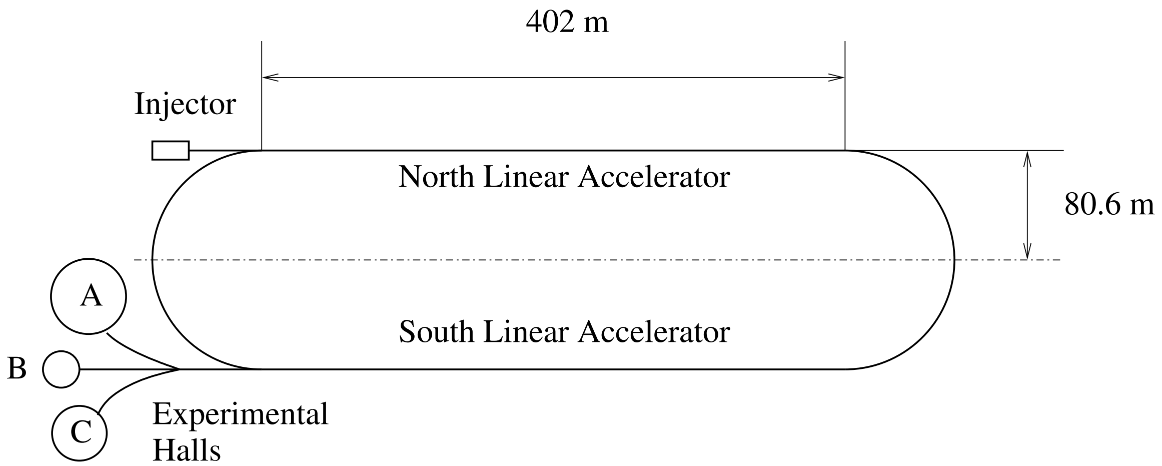

Figure 3.1: Jefferson Lab accelerator site plan.

The electron beam can be split in order to be used in three simultaneous experiments taking place in the three separate experimental halls, each equipped to perform different experimental tasks. Hall B, in addition to the CEBAF Large Acceptance Spectrometer, is also equipped with a bremsstrahlung photon tagger for the production and monitoring of a photon beam. Doing photon tagging experiments, which involve a coincidence between a photo-induced reaction product and the tagging electron, is only possible because of the continuous-wave nature of the primary electron beam. This ensures a relatively low level of background due to accidental coincidences, permitting at the same time a high data-acquisition rate.

3.3 The photon beam

3.3.1 The photon-tagging technique

The quasi-monochromatic photon beam used in the experiment was produced by the *photon-tagging* technique, schematically presented in Fig. 3.2. An electron beam of well-defined energy E_0 is passed through a thin radiator to produce bremsstrahlung. The scattered electrons in turn pass through a magnetic spectrometer and are detected in the spectrometer focal plane. The residual energy E of the scattered electron is deduced from its measured position in the focal plane.

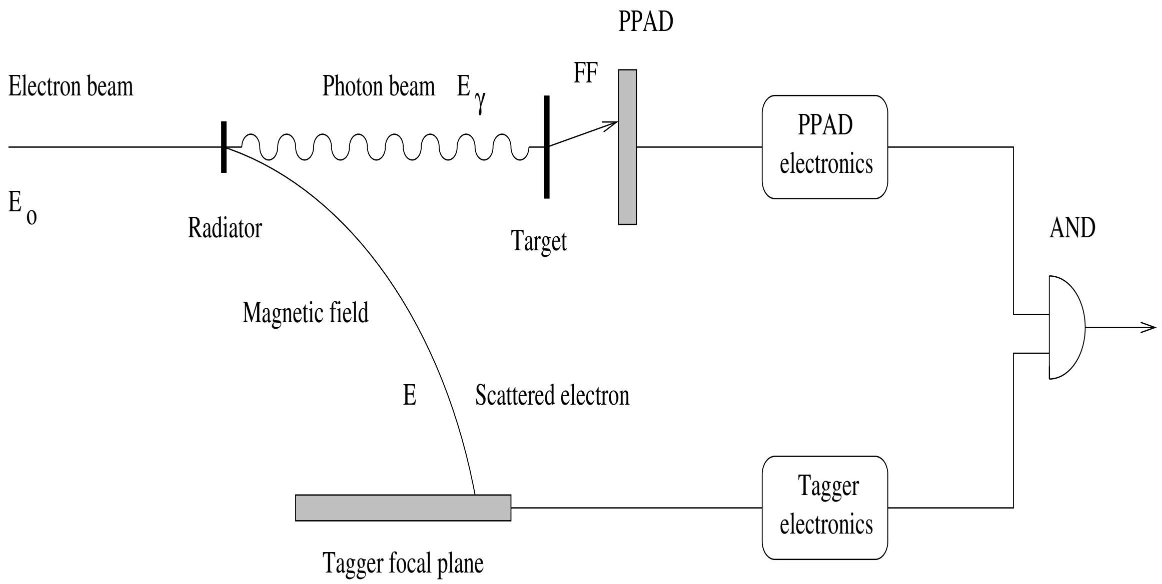

Figure 3.2: Conceptual diagram of the photon-tagging technique.

The tagged-photon beam was incident on the fission targets. If a photon is absorbed in a target, it might cause the nucleus to fission. One of the two fission fragments emitted will be within the geometrical acceptance of the PPAD. The coincidence required between a scattered electron detected in the focal plane of the tagging spectrometer and the fission product detected in the PPAD provides the way to *tag* the photon which has produced the photofission reaction. Using conservation of energy, the photon energy can be determined as $E_\gamma = E_0 - E$.

3.3.2 The Photon Tagger at Jefferson Lab

General description

A schematic diagram of the photon-tagging system at Jefferson Lab is shown in Fig. 3.3. The system is described in detail in Ref. [Sob00]. The bremsstrahlung radiator is placed immediately upstream from the magnetic spectrometer. At the energies above 800 MeV which are available at Jefferson Lab, both the scattered electrons and the bremsstrahlung photons have very small characteristic angles, so that after passing through the radiator they travel approximately along the electron beam line. The electron beam then enters the tagger magnet and scattered electrons are bent according to individual electron energies. The photon beam travels through a channel in the tagger magnet towards the reaction chamber where it can induce photofission reactions in the various fission targets.

The tagger magnet is a single, uniform-field dipole. Electrons which did not produce bremsstrahlung travel along the curved edge of the dipole towards the beam dump, while the trajectories of scattered electrons have larger curvatures. The magnet geometry covers a very large dynamical range of photon energies: 20% to 95% of the incident electron energy. The mapping of the magnetic field was performed for 10 different magnet currents. The three magnet currents closest to the values used in the present experiment, their corresponding incident electron energies, and magnetic field strengths are given in Table 3.1.

The scattered electrons pass through a vacuum box attached below the magnet and ending very near the focal plane of the magnet. The uniform magnetic field of the magnet is configured such that its focal surface can be well approximated by a flat plane. Along the focal plane, the hodoscope, consisting of two successive planes of plastic scintillators, detects the deflected electrons. The two layers provide two kinds of information: the energy and the timing of the deflected electrons. The electron

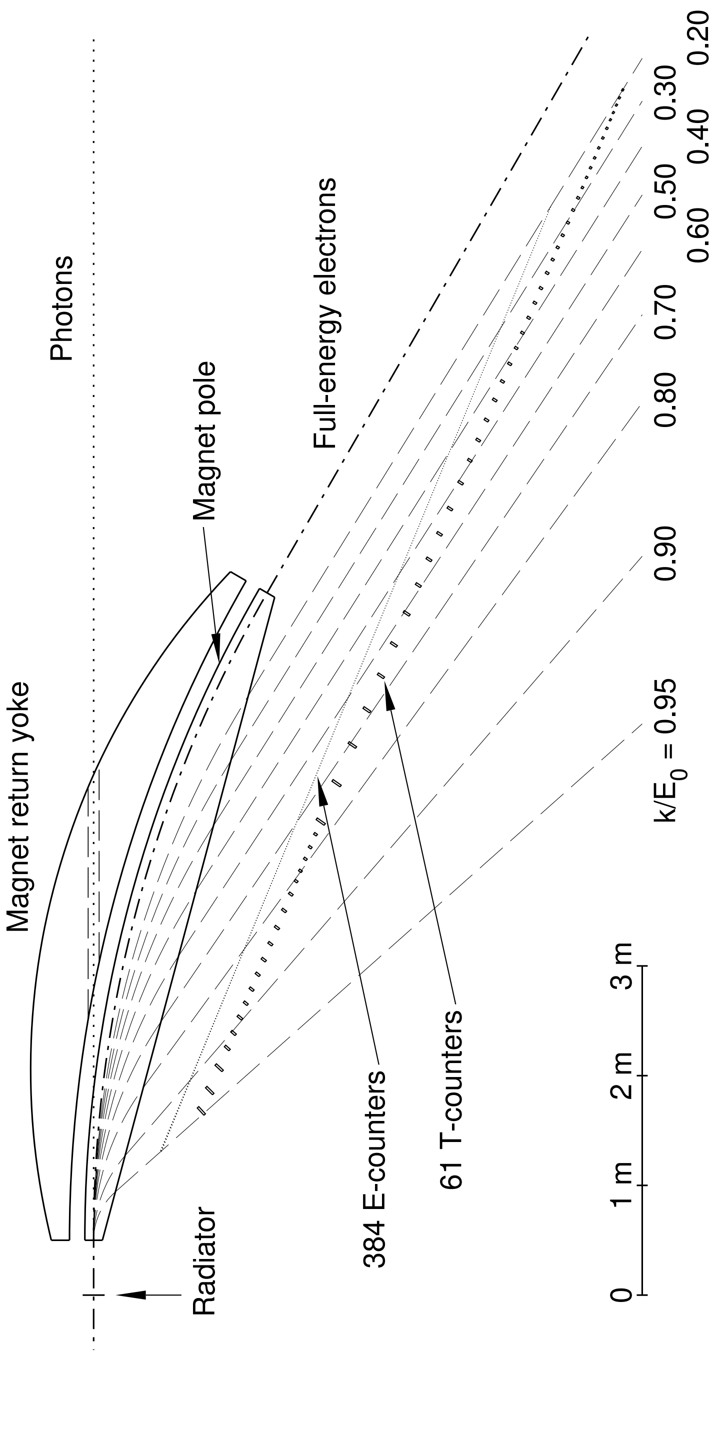

Figure 3.3: Schematic view of the overall geometry of the Jefferson Lab tagging system.

I (A)	E_0 (GeV)	B (T)
300	0.900	0.26
600	1.795	0.51
1400	4.144	1.17

Table 3.1: Tagger-magnet excitation data.

energy is used to determine the energy of the corresponding photon, while the time is used when requiring a coincidence between a tagging electron and a downstream event induced by the associated tagged photon.

The first scintillator layer lies essentially in the focal plane and consists of 384 small overlapping scintillators called *E-counters*, where E stands for energy. The dimensions of the E-counter scintillators are 0.4 x 20 x (0.6-1.8) cm. The signal from an E-counter is collected at one end of the scintillator and is sent through optical fibers to a photomultiplier tube (PMT.) Due to its high segmentation and overlapping design, the E-plane provides a very good energy resolution of 0.1% of E_0. On the other hand, because of their variable width, the E-counters subtend approximately constant energy intervals of 0.003 E_0.

The time-to-digital converter (TDC) hit spectrum of the E-counters, reflecting the shape of the bremsstrahlung spectrum, is shown in Fig. 3.4(a). The E-counters were not all functioning properly at the time when the photofission experiment took place. Four E-counter PMTs receive the high voltage from a single voltage supply. Thus, a malfunctioning high-voltage supply was compromising all four corresponding E-counters. Additionally, there were individual PMTs counting either too low or too high.

The *T-counters*, called T for timing, comprise the second scintillator plane. There are 61 large overlapping scintillators, each of which is read at both ends using fast photomultiplier tubes. The T-counters are 2 cm thick and have variable widths, such that they have approximately the same counting rates. There are two distinct

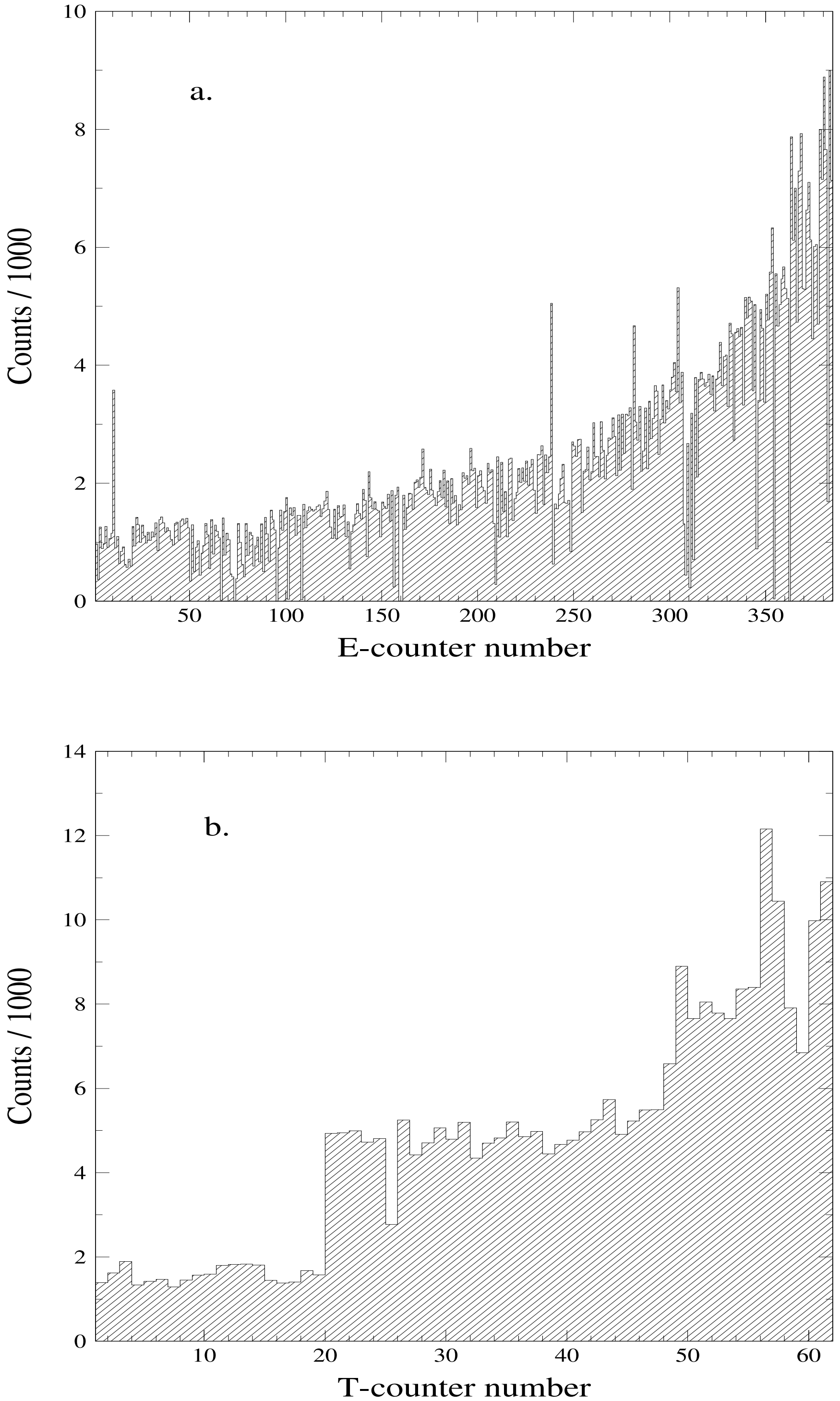

Figure 3.4: Hit distributions for (a) E-counters, reflecting the shape of the bremsstrahlung spectrum; (b) T-counters, having approximately the same counting rates within two different groups. The higher rates at the end of the focal plane reflect the presence of beam-related background.

groups of T-counters. The first 19 detectors cover the photon energy range $E_\gamma = (0.75 - 0.95)\ E_0$. The next 42 counters span the range $E_\gamma = (0.20 - 0.75)\ E_0$ and count about 3 times faster than the ones in the first group, as can be seen in Fig. 3.4(b). The slower counting group was designed for experiments using only the highest-energy photons and operate at high tagger rates. Figure 3.4(b) shows a problem in T-counters 48-61, which was quite serious for our experiment. The higher counting rates in the T-counters 48-61 are due to fission or (γ, α) events caused by untagged low-energy photons in accidental coincidence with electrons that struck the vacuum pipe or flange at the exit of the tagger vacuum box, towards the low-photon-energy end of the hodoscope. A correction for these background events has to be applied to the data. The very low counting channel no. 25 was not used for further analysis.

The photon-tagger electronics

The logic diagram of the tagger electronics is presented in Fig. 3.5. The PMT signals from the E-counters are sent to a specifically designed amplifier-discriminator-multiplexer logic (ADML) module. The output from each discriminator goes to a multi-hit FASTBUS TDC (LeCroy 1877) with a resolution of 500 ps/channel. The TDCs are operated in common-stop mode, with the stop signal given by the trigger signal.

The signals from the T-counter PMTs are sent to fast constant-fraction discriminators (Phillips 715) and then to FASTBUS (LeCroy 1872A) TDCs with a resolution of 50 ps/channel. These TDCs are operated in common-start mode. The start signal comes from the experimental trigger, which was a signal either from one of the PPADs or from the Master OR (see below), depending on whether a data run or a tagging-efficiency run was being performed (see next section). The discriminator signals provided the stop for the individual T-channels.

Signals from the E-counter discriminators and from both left and right T-counter discriminators also go to a fast AND logic unit (Phillips 754). During this experiment, if two of the three hits were present, a signal was sent to the Master OR. Another

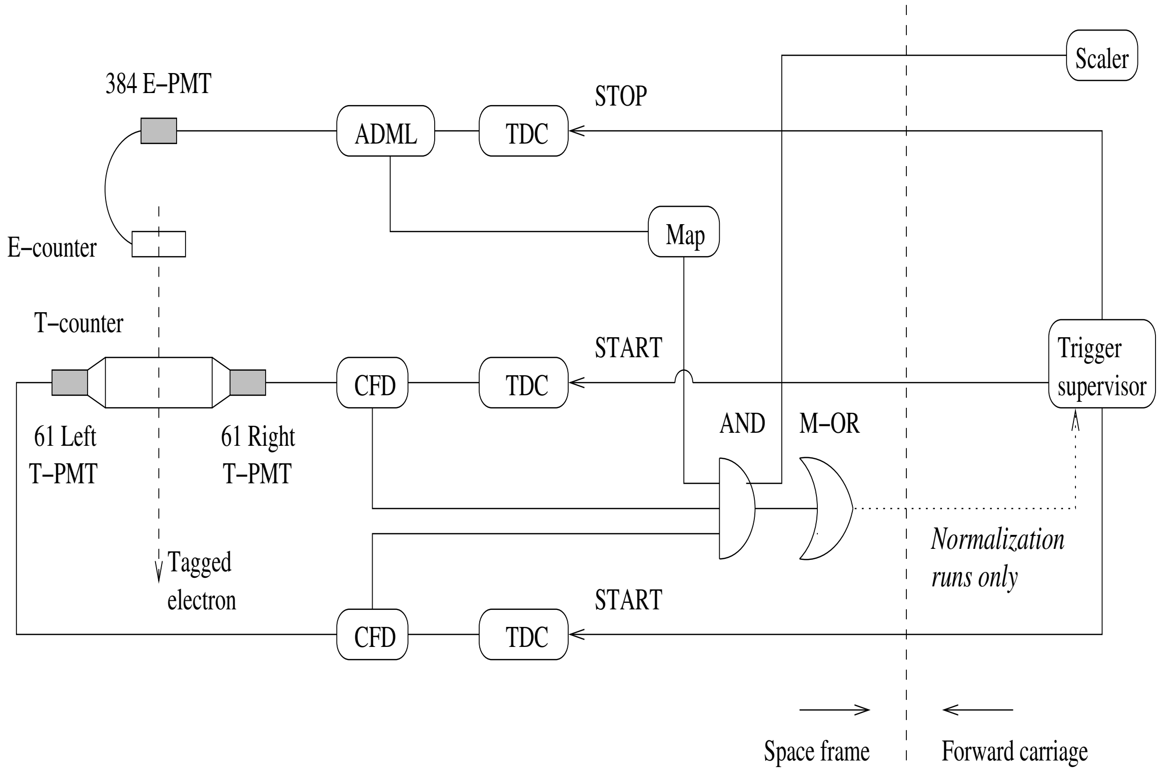

Figure 3.5: Logic diagram of the tagger electronics. After discrimination, the signals are sent to time-to-digital converters, then counted by scalers. For the normalization runs, the logic OR of the T-counter signals provides the experimental trigger.

output of the AND gate was scaled using a 100 MHz scaler (CAEN V560E). The Master OR generator is a cascade of 4-input fast OR gates (Phillips 754). The Master OR provides the signal that a tagging electron was detected. For our normalization runs (and for the CLAS data runs), this gave the experimental trigger.

3.3.3 Photon flux measurement

The number of photons which actually strike the fission detectors is slightly smaller than the total number of electrons which have been detected. The ratio of photons which actually illuminate the target to the tagging electrons is called the *tagging efficiency*. In order to determine this ratio, we used a total-absorption lead-glass detector placed in the same position as the reaction chamber. By adjusting the high voltage supplied to the PMT associated with the lead-glass detector, we made sure that all pulses were well above the discriminator threshold of the detector. Thus, for a given tagger channel, the tagging efficiency is given by the ratio between the number of photons detected by the lead-glass detector and the number of electrons detected in the tagger focal plane.

Since a high photon flux could damage the lead-glass detector, special tagging-efficiency runs were necessary. The lead-glass detector and the reaction chamber were placed parallel to the beam line on a remotely controlled moving table, which moved perpendicular to the beam line: thus we could insert either one along the beam line. For the tagging-efficiency runs, the incident electron beam current was reduced, and the lead glass was positioned along the beam line in the same position as the reaction chamber; thus the photon flux was measured at the exact same location where the photofission reactions took place. The electronics readout of the lead glass was one of the channels of the data readout, but in this case the experimental trigger was given by the Master OR. Thus, the lead-glass TDC was started by electrons detected in the focal plane and stopped by photons detected in the lead glass. In Sec. 5.1.1 we discuss the way we analyze the data from these tagging-efficiency runs.

3.4 The fission-fragment detectors

3.4.1 Introduction

Although photofission cross sections have been extracted from neutron-multiplicity measurements [Cal80a, Car84, Ber86], direct fragment detection is by far the more desirable method to measure the photofission cross section. Special characteristics are required for fission-fragment detectors used in photofission experiments:

- Their time resolution must be better than 1 ns. This is important for the time coincidence required in tagged-photon experiments at Jefferson Lab, where the time interval between beam bursts is 2 ns

- Their total energy or energy-loss resolution must be sufficient to provide good discrimination between fission fragments and α-particles

- They have to be insensitive to photon and neutron backgrounds
- The usable solid angle must be as large as possible in order to reduce long measuring times
- Their efficiency for fission fragments must be high
- The detector must be capable of sustaining high counting rates for fission fragments
- A high integrated dose of fission fragments should not cause a significant deterioration of the detector properties
- The production cost must be low. This makes it easy to replace them if detector contamination or damage occurs.

A multiwire proportional counter would fulfill most of these demands, but its time resolution would be too poor, thus precluding the use of the photon-tagging technique. Another possibility would be thin-film plastic scintillators, but their energy resolution would be insufficient for an effective separation of fission fragments from lighter particles. Large-area surface-barrier detectors have good time and energy resolution; however, they are highly sensitive to background radiation and deteriorate from radiation damage after a dose of only about 10^8 fission fragments/cm^2, preventing the accumulation of data having the desired statistical accuracy. The best compromise in fulfilling all the above demands is achieved by choosing gas-filled proportional counters, in particular parallel-plate avalanche detectors (PPADs). Their applicability in detecting fission fragments has been demonstrated in several experiments [Hem75, Arr81, Dre84, Gar86].

Moreover, the total thickness of such a counter can be kept rather small, due to the low operating gas pressure. This feature, together with the finite range of the fragments and the fact that the PPADs are almost transparent to a high-energy photon beam, allows a multiple-target-detector set-up to be used. Placing several target-detector pairs in the beam line enables one to achieve multiple objectives. First, by using several targets of the same isotope, one can increase the number of counts per isotope acquired in a given beam time. Furthermore, by doing simultaneous measurements for various isotopes, the relative comparisons among them will be more reliable.

3.4.2 Principle of operation

The operation mechanism and characteristic properties of PPADs have been known since the early 1950s [Chr52], and the basic theory of these detection systems is given in several publications [Rae64, Arr86]. A PPAD is basically a proportional counter. The two electrodes have parallel-plane geometry, are separated by a small distance, and are placed in a gaseous atmosphere. An almost homogeneous electric field is produced between the plates by applying an external high voltage, the value of which must be below the sparking threshold of the system. The ionizing particle to be detected (*e.g.*, the fission fragment) traverses the gap between the electrodes and produces a track of primary electron-ion pairs in the gas. These pairs, accelerated in the strong electric field, start Townsend-type avalanches of electrons. For an avalanche induced by a single electron along a drift path of length x, the average number of secondary electrons $n_e(x)$ is given by

$$n_e(x) = exp(\alpha x) \tag{3.1}$$

where α denotes the first Townsend coefficient. For organic gases and reduced electric field strength E/p between 50 and 150 V/cm-Torr, the following expression is valid for the mean ionization probability per unit length α:

$$\alpha/p = A\ exp(-\frac{B}{E/p}) \tag{3.2}$$

where p is the gas pressure and E is the electric field, while A and B are constants specific to a given gas. By integrating the contribution of single-electron avalanches, the number of electrons between the plates at a given time t is

$$N_e(t) = N_0(d - v_e t)\ exp(\alpha v_e t) \tag{3.3}$$

where N_0 is the number of primary electron-ion pairs produced per cm by the ionizing particle, d is the distance between the plates, and v_e is the drift velocity of the electrons, which is assumed to be constant. Note that the above integration is valid only if $N_0 \simeq const$ as a function of x, which is true since the energy lost by a fission fragment crossing the PPAD gap is very small compared with its total kinetic energy.

The electron charge migrating towards the anode generates a current I_e with a time dependence

$$I_e(t) = e\frac{v_e}{d}N_e(t) = ev_e N_0\ (1 - \frac{v_e t}{d})\ exp(\alpha v_e t) \tag{3.4}$$

The signal described by $I_e(\mathrm{t})$ has an amplitude proportional to $exp(\alpha v_e t)$ and a width proportional to $1/\alpha v_e$. Thus, to maximize the amplitude and to minimize the width one has to maximize the product αv_e. This is done by choosing the gas and the operating parameters judiciously.

Positive ions are created simultaneously with the secondary electrons. The slow pulse (rise time $\geq 1\mu s$) which they induce in the external circuit is suppressed electronically, and only the fast pulse (rise time $\approx$ few ns) due to electron migration is used for further processing.

3.4.3 Detector design

Constructional aspects

The constructional details of a PPAD are shown schematically in Fig. 3.6. The main novelty in the design of our detectors is that the anode has been replaced by a wire grid. This solution was adopted because of the very short range of the fission fragments. If the fragments have to pass through one of the electrodes in order to reach the detector gap, this electrode has to be a very thin film (usually a few μm), and this can be a very challenging technical problem. Alternatively, PPADs have been built with the target itself acting as an electrode, but then other solutions have to be found for non-conducting materials and oxidation of the foils. Thus, by having one electrode made of a grid of thin wires, only a very small fraction ($\sim 2\%$) of the fission fragments will hit the wires, while most of them will be able to enter the active region of the detector without having suffered any energy loss. We chose 25-μm diameter gold-plated tungsten-rhenium wires, vertically oriented and spaced 1 mm apart.

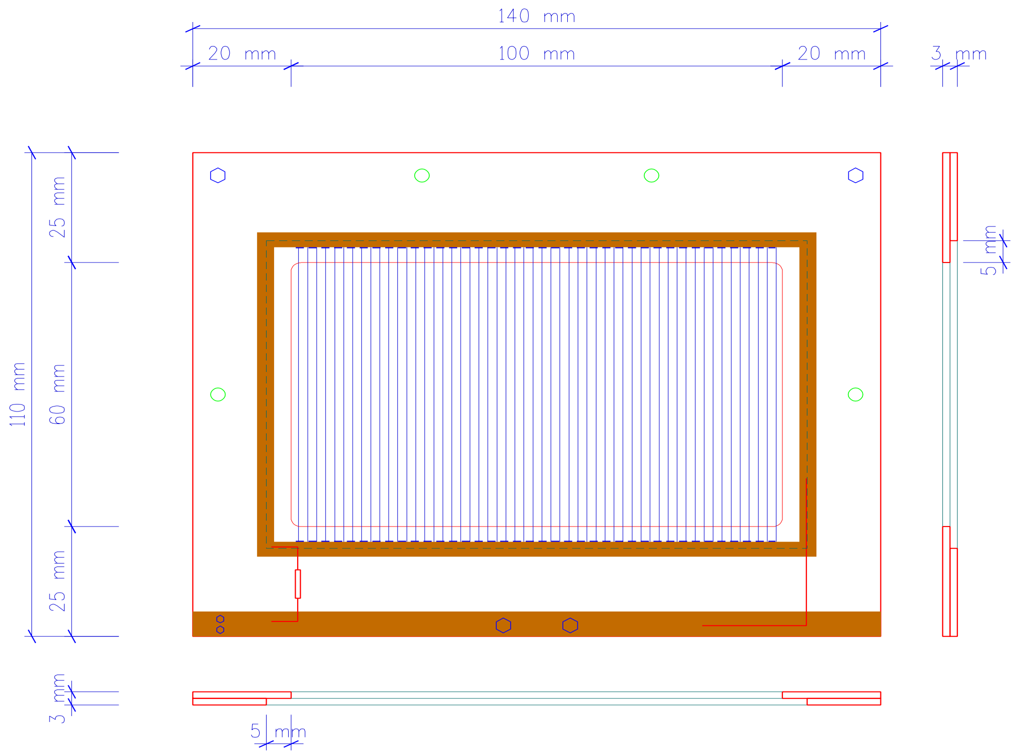

Figure 3.6: Constructional details of the PPAD design. The anode consists of a wire grid, the cathode is an aluminized mylar foil, and both are attached to copper-plated FR4 frames.

The cathode plane is a 25-μm foil of aluminized mylar. Both anode wires and the cathode foil are stretched on rectangular 1.5-mm thick copper-plated FR4 frames. The frames were placed back to back so that the 3-mm combined thickness provided the detector gap. In order to obtain well stretched wires and foils having constant tension, both wires and foils were first stretched on bigger frames and then the detector frames were glued using only the central parts of the large frames. For both electrodes the electrical connection with the copper side of the frame is made by using silver-filled epoxy glue, while the stretching tension is secured by applying regular glue.

Several precautions were necessary in order to prevent electric discharges. All of the sharp edges were rounded, and all metallic surfaces were covered with a layer of nonconducting glue, the copper at the edges of the frame window was removed, and the anode window was made smaller than the cathode one. This last feature replaces the straight path which breakdown electrons would take by a longer and curved path.

Fig. 3.7 shows the electric circuit used to collect the signal from a PPAD. The electrodes are charged by means of a low-pass filter consisting of a protective resistor R_p = 100 kΩ and a coupling capacitor C_c = 20 nF. This filter protects the rest of the circuit against noise from the high-voltage power supply. The parameters of the electric components were chosen to match the 50-Ω input impedance of the amplifier (R = 820 kΩ).

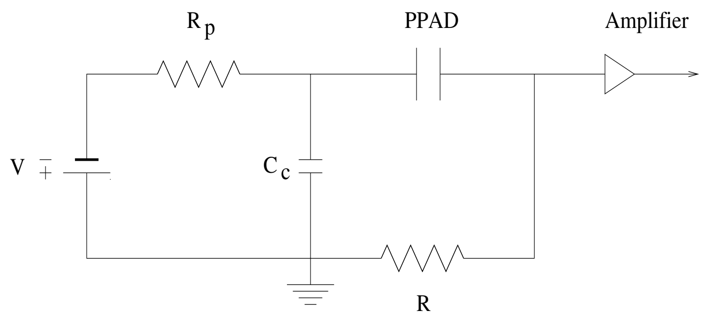

Figure 3.7: Electric circuit for PPAD signals. Negative high voltage (V) is supplied through a protective resistor (R_p) with a coupling capacitor C_c; the output impedance is adjusted by a resistor (R), and the signals collected from the anode wires are sent to an amplifier

Choice of operating conditions

From the previous section we recall that the PPAD signal depends strongly on the characteristics of the gas, as described by α and v_e. On the other hand, the parameters α and v_e depend on the ratio E/p (electric field strength to gas pressure). Therefore, we must choose both gas and operating conditions so that we get a maximum value of the product of α and v_e.

Pure hydrocarbons seem to be best suited for low-pressure gas-filled proportional counters. Isobutane has been shown to provide very stable operation [Bre77]; it is also inexpensive and easy to handle. The high density of isobutane (2.67 g/l) yields high primary ionization, which is important for precise timing measurements. Also, due to its good quenching properties, the amplification can be pushed to higher values than in other gases for similar electric breakdown thresholds.

However, once the gas is chosen, there is no possibility to vary the electron drift velocity v_e by means of the operational parameters; except for methane, the drift velocity v_e for hydrocarbons saturates quickly with increasing E/p. On the other hand, the first Townsend coefficient α has a maximum value for gas pressures around 10 Torr. Thus, the most effective way to increase α is by increasing the high voltage, while keeping it below the electric breakdown threshold.

Using ^{252}Cf as a spontaneous-fission-fragment source, we measured the PPAD counting rates for three different gas pressures p = 10, 15, and 20 Torr, varying the applied high voltage accordingly, as shown in Fig. 3.8. The counting-rate curve for each pressure has an almost flat region as a function of the applied voltage, over an interval of about 60 V; we picked the central value of this plateau to ensure stable operation. Thus, our PPADs were operated with isobutane at 15 Torr and an applied high voltage of about 750 V.

Reaction chamber / Target mounting

Each of the fission targets consists of a thin layer ($\sim 1\ mg/cm^2$) of the fissionable isotope deposited on a backing foil. For the actinide isotopes, the backing was a 100-μm aluminum foil; for lead the backing was a 25-μm mylar foil. The actinide targets were held between two rectangular frames, with an inner window of 5 cm $\times$ 10 cm, the same as the detector itself. The lead foils were glued onto similar frames. The technique used was the same as for preparing the cathode planes of the PPADs, that is, by stretching a larger foil on a bigger frame first, and then gluing the frames in the central part. All the frames were made of FR4, which is the material used for

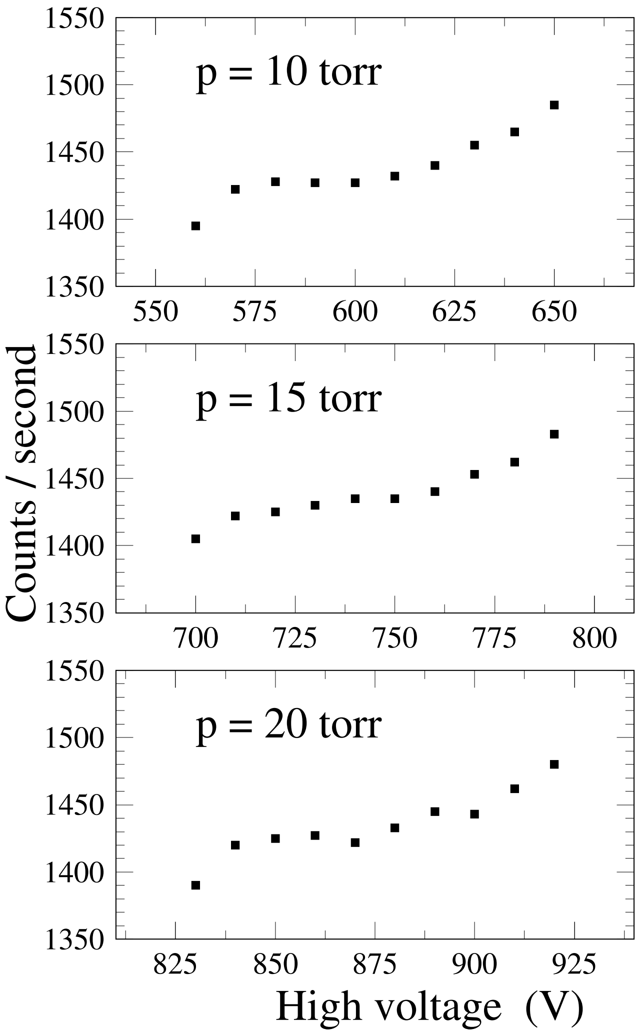

Figure 3.8: PPAD counting rate as a function of applied high voltage for three different isobutane pressures: 10, 15, and 20 Torr. This test was done using a ^{252}Cf source.

printed-circuit boards (for which case it is copper-plated).

Each target was mounted in front of its own detector, using Teflon screws through the corner holes in the frames. Additionally, for the actinide isotopes, two circular 4-cm diameter collimators were used. One was placed immediately after the target, although it may not have been absolutely necessary, in view of the very small size of the photon beam at Jefferson Lab. However, especially for the highly α-radioactive ^{233}U isotope, it helped to reduce the rate of α particles reaching the detector. By placing the second collimator just in front of the anode wire plane, the geometrical acceptance of the detector was well defined. The collimators were not used for lead because the lead targets and their associated PPADs were tilted by 45^o with respect to the beam line. Moreover, because of the small photofission cross section of lead, we needed to maximize the detector acceptance by placing each target as close as possible to its associated detector. Thus, the distance between the lead foil and the anode wire grid was 0.4 cm, while the distance from one of the actinide foils to the second collimator was 1.3 cm. Fig. 3.9 shows the different parts of a target-PPAD

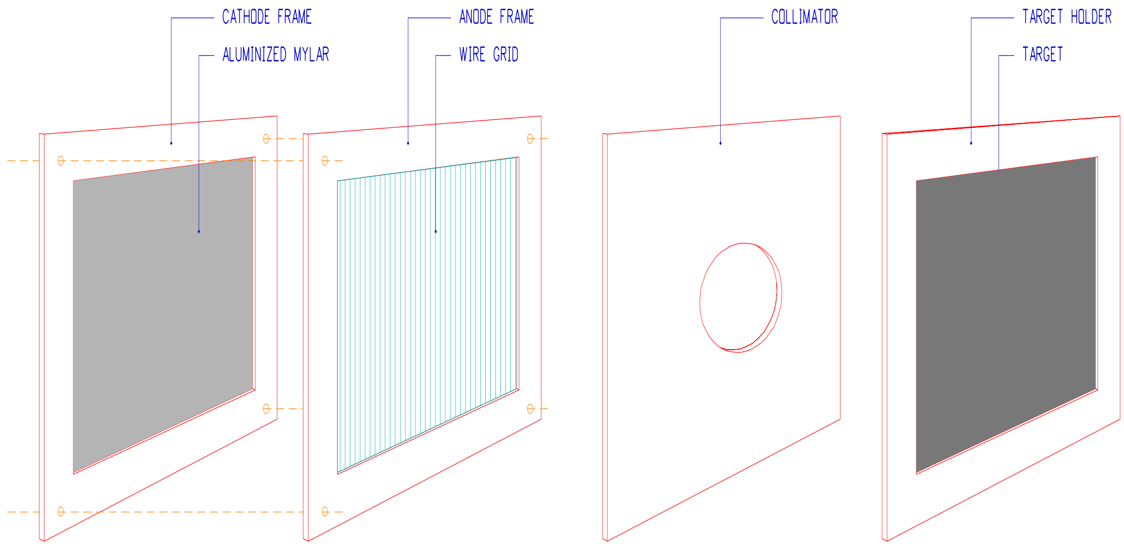

Figure 3.9: Different parts of a target-PPAD pair: Target and target holder, collimator, anode frame with wire grid, cathode frame with aluminized mylar foil.

pair.

All of these target-detector combinations shared the same reaction chamber and thus the same gas pressure. This arrangement has the important advantage of enabling us to study all of the fission targets simultaneously, under exactly the same experimental conditions. The reaction chamber (see Fig. 3.10) is a 120 cm $\times$ 20 cm $\times$ 16 cm steel box with an aluminum lid. Two parallel C rails were attached on the inner side of the lid, providing the support for the target-detector pairs, which were suspended so that their centers were aligned with the entrance and exit windows of the chamber. These were 0.5-mm-thick aluminum flanges. Thus, by aligning the two windows of the chamber with the photon beam line, we were sure that the beam passed through the center of the targets and detectors.

The lid of the chamber (see Fig. 3.10) also allowed for the possibility of mounting four electrical feed-throughs. One of them was used to provide 20 channels of high voltage to the detectors. In the other three we installed 10-channel LEMO connectors for the signals collected from the detectors, to be sent to the amplifiers.

Gas System

Figure 3.11 shows a schematic diagram of the gas-handling system. The gas supply consists of one cylinder of isobutane and one cylinder of nitrogen. The isobutane is the working gas for the detectors, while the nitrogen is necessary to produce a non-flammable mixture, and thus ensure safe evacuation of the isobutane. The pressure of the gas inside the chamber is measured by an MKS Baratron 626 absolute pressure transducer. The transducer was connected to a digital readout which could be viewed during the experiment using a video camera, thus allowing continuous monitoring of the gas pressure from the counting room.

The flow restrictor and the needle valve on the supply side were required in order to meet the safety standards of Jefferson Lab. For the same reason we had a relief valve on the evacuating side. The chamber was evacuated first through the small-conductance branch (in order to avoid big differences in pressure), and then through the large-conductance branch (in order to achieve a good vacuum in a short time).

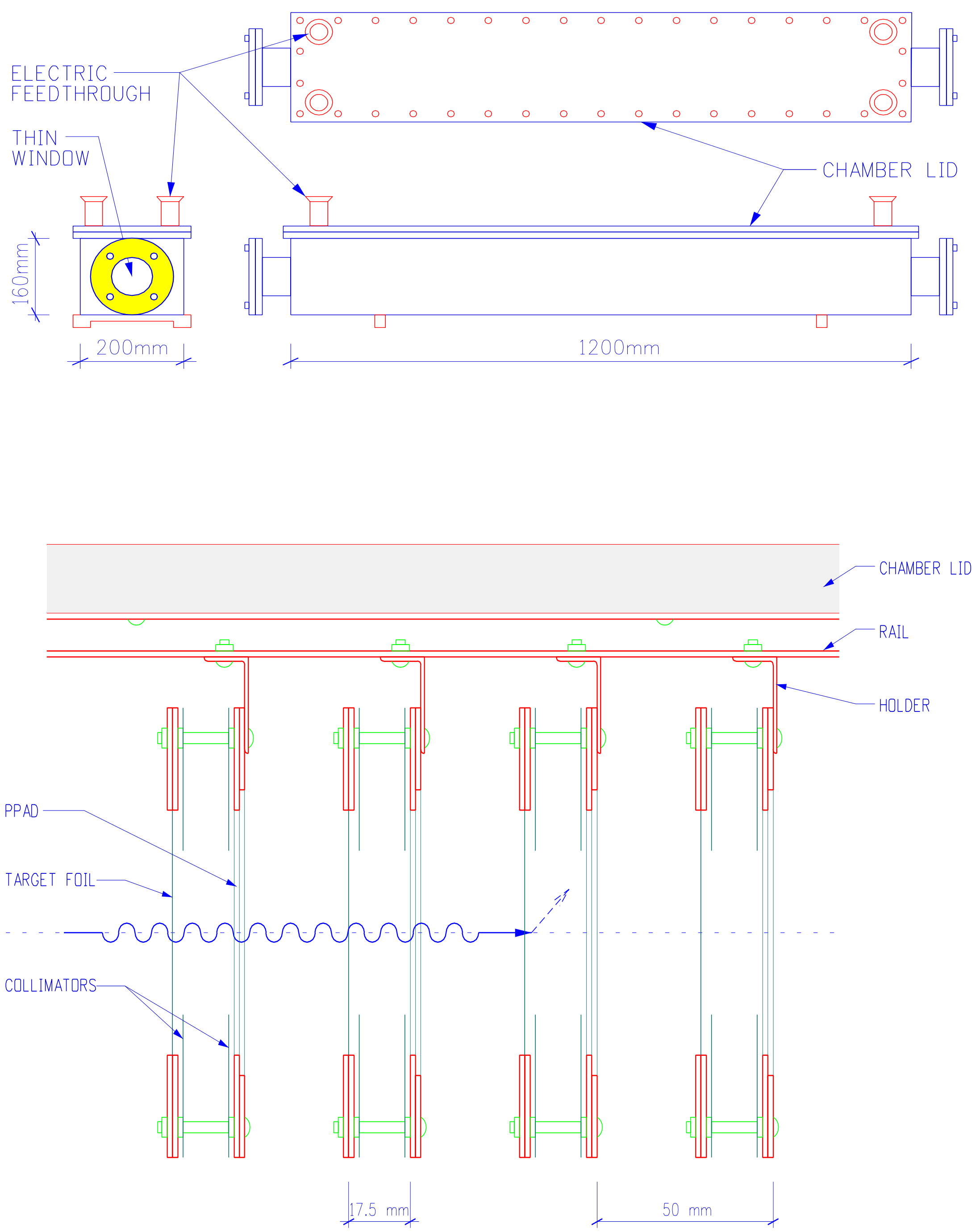

Figure 3.10: Schematic view of the photofission reaction chamber. The target-PPAD pairs were attached to the chamber lid and their centers were aligned with the chamber windows.

Our previous photofission measurements at SAL proved that the PPADs would operate in a stable regime as long as the gas pressure was kept between 15 and 16 Torr. We also learned that the gas pressure could be kept within these limits for a longer time by carefully cleaning the chamber and keeping it under vacuum for a few days before the experiment. During the nine days of data-taking, the gas had to be exchanged four times.

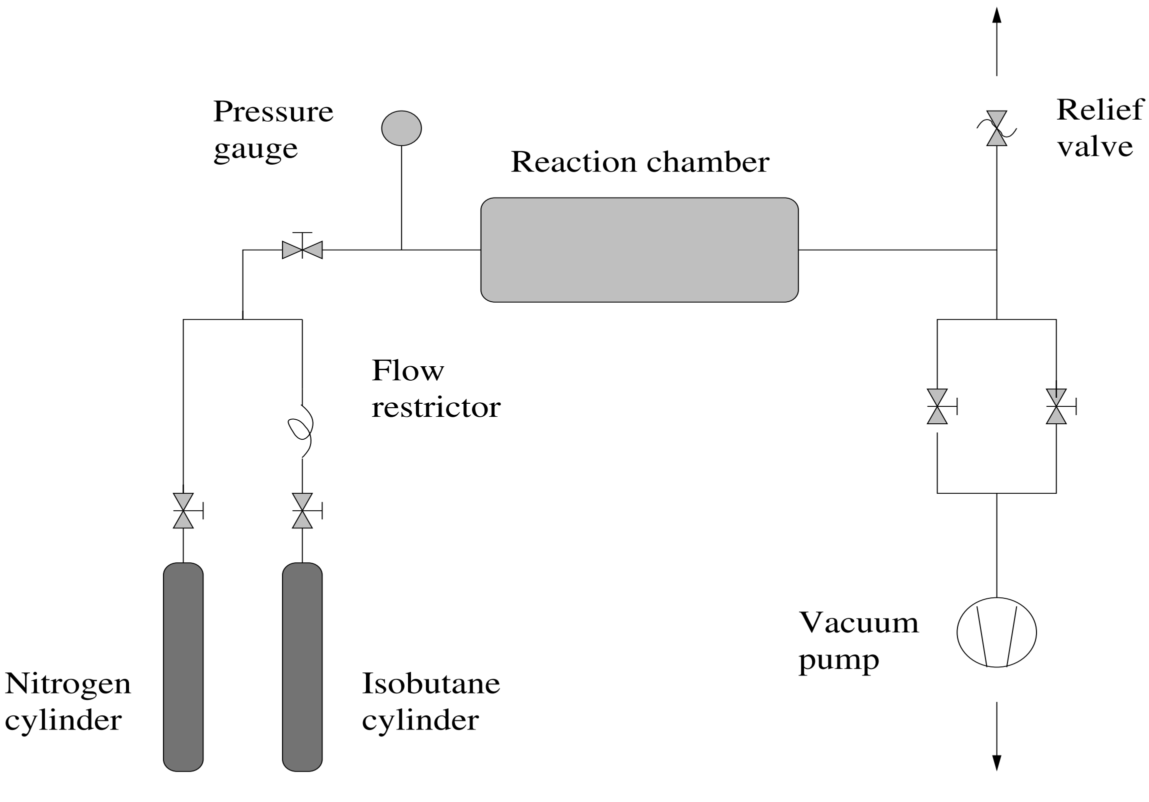

Figure 3.11: Schematic diagram of the gas-handling system.

3.4.4 PPAD electronics setup

The experimental setup in Hall B at Jefferson Lab made it necessary to divide the electronics readout into two stages. The modules processing the signals coming directly from the detectors were NIM standard and were placed immediately below the reaction chamber. The final stages were CAMAC/FASTBUS standard and were placed at the opposite end of the experimental hall, about 50 m away (see Fig. 3.12).

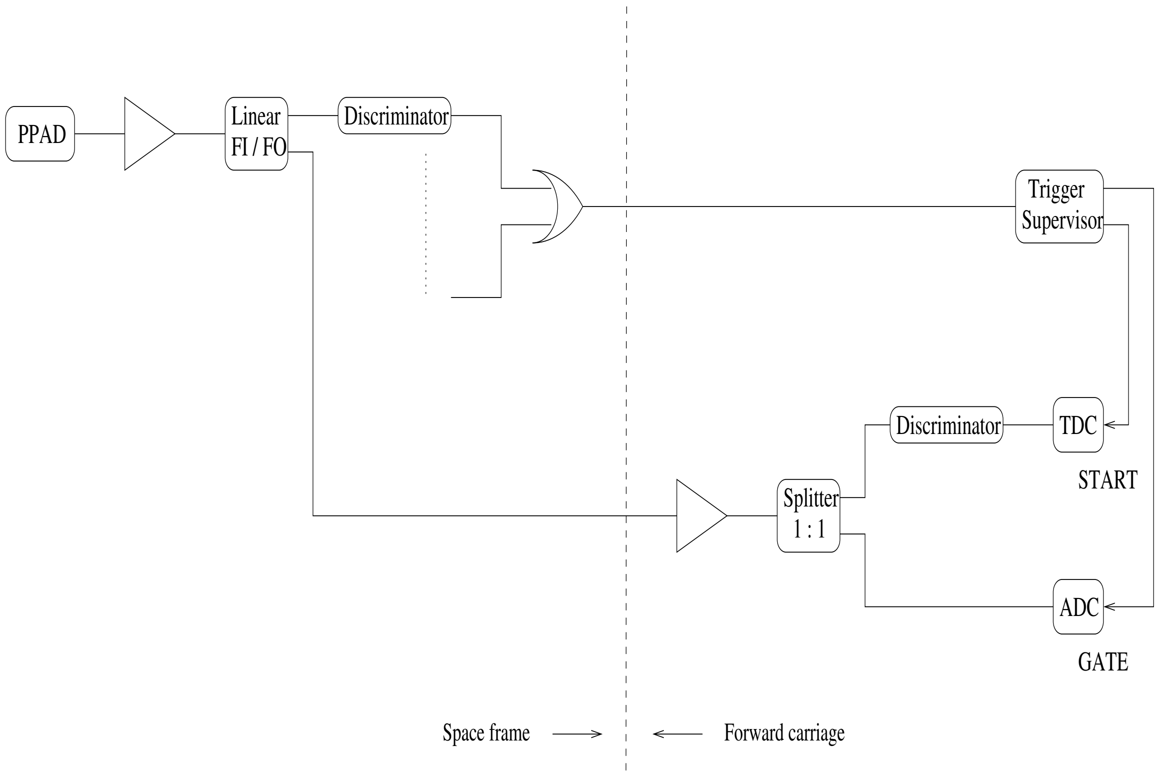

Figure 3.12: Logic diagram of the trigger signal. One copy of the amplified PPAD signals was sent to the PPAD ADCs and TDCs. The trigger was generated by the logical OR of all of the digitized PPAD signals.

The anode signal from each PPAD was sent directly to one of the channels of an octal fast-timing linear amplifier (EG&G ORTEC FTA820A). The fixed gain of these amplifiers is 200, which means that the 5-mV pulses generated by a fission fragment passing through the detector were amplified to 1 V, while the 1-mV pulses due to α particles were amplified to 200 mV.

The amplified pulses were split passively, using linear FanIn/FanOut modules (LeCroy 428F). One output was converted to a standard signal by means of a leading-edge discriminator. The discriminator digital output was used to generate the trigger for fission data runs. All of the discriminator outputs were sent through a cascade of fast OR gates (Phillips 754), so that the logical OR of all of the PPAD signals produced the trigger signal. This signal was piped across the hall to the trigger-supervisor module.

After the FanIn/FanOut, the analog signal had to travel through long cables (250 ns) to reach the other end of Hall B. Because of the losses in the cables we had to use a second stage of amplification. We used variable-gain fast amplifiers (Phillips 777) with the gain set to 2. The analog signals were then split in two using custom-made signal splitters (UVA 122B) with a splitting ratio of 1:1. Half of the analog signal was used to record the energy deposition spectrum of the ionizing particles which produced a pulse in a PPAD using FASTBUS ADCs (LeCroy 1881M). The ADC time gate used to integrate the charge was given by the trigger supervisor. The other half of the analog signal was standardized by CAMAC discriminators (2313) and the timing information was recorded using FASTBUS TDCs (LeCroy 1872A). The TDCs were working in common-start mode, with the start signal coming from the trigger supervisor and the stop from individual PPADs. The raw ADC and TDC PPAD data were formatted and stored by CODA, the data-acquisition system used at Jefferson Lab.

One should also mention that, unlike most experiments using the photon-tagging technique, we did not need to require a hardware coincidence between our detectors and the photon tagger. Thus, any fission fragment detected by the PPADs produced an experimental trigger. This was possible because of the low counting rates of our experiment.

3.5 The photofission measurements

The experimental setup used for the photofission measurements is presented in Fig. 3.13. The reaction chamber was positioned in the photon beam path with the entrance window located 10 m downstream of the tagger radiator. The axis of the chamber was aligned to within approximately 1 mm with respect to the beam axis. For all of the experimental runs, the electron beam was incident upon a gold radiator foil having a thickness of 10^{-4} radiation lengths (646 $\mu g/cm^2$).

The photofission measurements were performed at three different electron beam energies. For each of them, the beam current was chosen so that the signal-to-

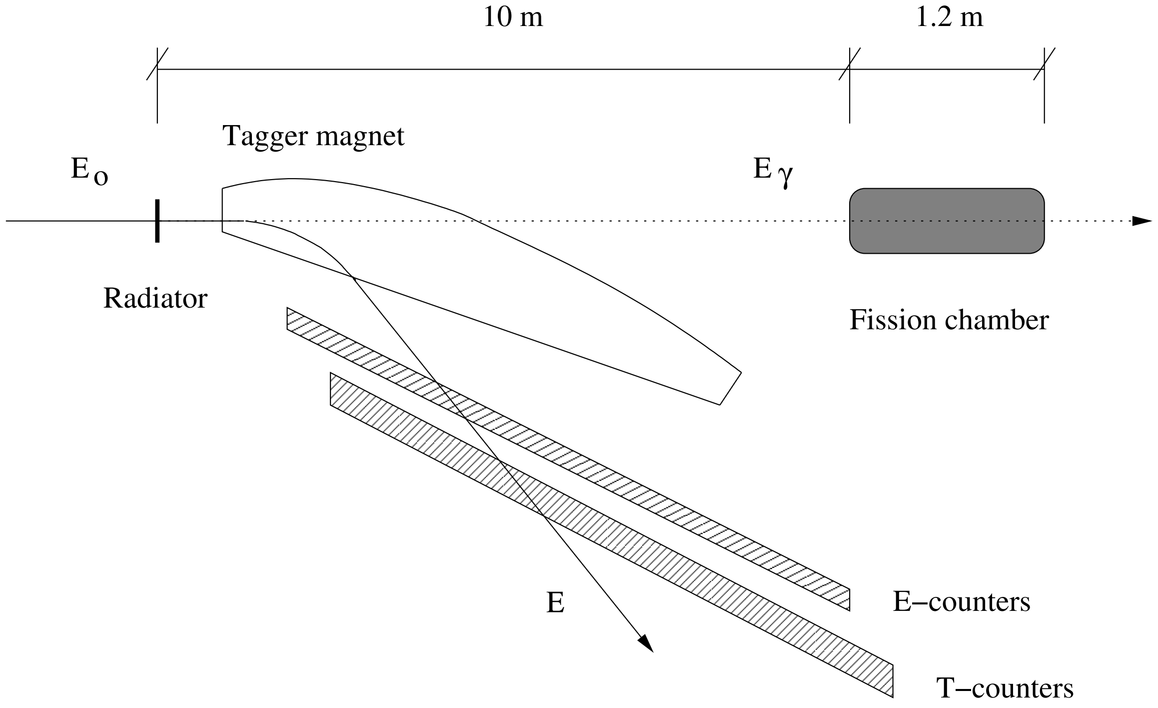

Figure 3.13: Schematic view of the experimental setup used for the photofission measurements. Drawing is not to scale.

background ratio was approximately 1:1 in order to optimize the counting statistics. The electron beam and tagger parameters for the three running sets are presented in Table 3.2.

For the tagging-efficiency runs, the beam current was reduced to 0.1 nA and the fission chamber was replaced by the lead-glass detector. We have two tagging-

E_0 (MeV)	I_0 (nA)	I_m (A)	E_γ (MeV)	Tag.rate (s^{-1})
4045.1	15	1366	809 - 3843	2.24×10^7
1705.1	22	566	341 - 1620	3.26×10^7
875.9	14	290	175 - 832	2.72×10^7

Table 3.2: Running conditions for photofission measurements, showing the electron beam energy and current, the tagger magnet current, the range of photon energies, and the corresponding tagger rate .

efficiency runs for the 4-GeV data and three for the 1.7-GeV data. Unfortunately, due to the lack of time, we did not succeed in obtaining a tagging-efficiency run for the 0.9-GeV data.

Table 3.3 shows, for the three running periods, the length of the data taking periods (in hours) and the total number of events registered.

Run period	E_0 (MeV)	Run length (h)	No. events
Apr 13-16	4045.1	30	13.65×10^6
Apr 18-20	1705.1	30	17.34×10^6
Apr 21	875.9	2	750×10^3

Table 3.3: Length of the runs and number of events registered for the three running periods (see also the time line presented in Fig. 5.1.)

As mentioned before, we had several target-detector pairs for each isotope. The way they were arranged in the reaction chamber is shown in Fig. 3.14 and the target positions are identified in Table 3.4.

All of the actinide targets, with the exception of the last thorium target, were placed perpendicular to the photon beam. The thorium target in position 15, together with all of the lead targets and the mylar one, were placed at an angle of 45° with respect to the beam line. By tilting one of the actinide targets, we established a consistency check for the geometrical acceptances of the detector in the two configurations. The choice of thorium was justified by the fact that it has both the lowest photofission cross section and the lowest α activity of the actinides studied. Thus, by increasing its effective thickness, its rate was still comparable with the non-tilted actinides.

Because of the limited space inside the reaction chamber, we did not include an aluminum foil, which is the substrate for the actinides, as a "blank". This was justified by our previous measurements at SAL, where we found that the contribution of the aluminum substrate to the fragment yield is negligible. However, this is not the case

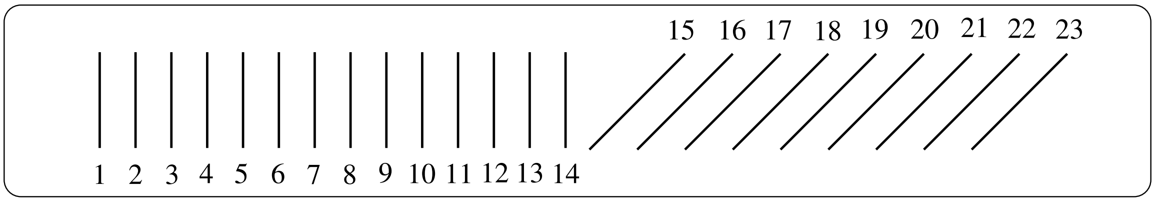

Figure 3.14: Top view of the reaction chamber, showing the arrangement of the 23 target-detector pairs. The isotopes for each of the 23 positions are given in Table 3.4.

Isotope	Position
^{233}U	1,6,11
^{235}U	2,7,12
^{238}U	3,8,13
^{237}Np	4,9,14
^{232}Th	5,10,15
^{nat}Pb	16-22
Mylar	23

Table 3.4: Positions of the target isotopes in the reaction chamber, where no. 1 is upstream and no. 23 is downstream, and they are 4 cm apart.

for the lead targets, where the Mylar foil contributes a background of a few percent to the lead yield. The Mylar foil used as a “blank” had the same 25-μm thickness as the one used as backing for the lead targets.

We checked the levels of background in the presence of beam, by doing three types of measurements: fission chamber out / radiator in; fission chamber in / radiator out; fission chamber out / radiator out. Additionally, we have a couple of runs with beam off, which ideally should be equivalent to the radiator out runs. The results of these runs, showing negligible background levels, will be presented in Sect. 6.3.

Part II

Data Analysis, Results and Conclusions

Chapter 4

Data Reduction

Typical raw ADC and TDC spectra for a PPAD are shown in Fig. 4.1. In the ADC spectrum, the sharp rise at low pulse height represents alpha particles with deposited energies above the hardware threshold, due to both natural α radioactivity and to induced (γ, α) emission. The broad peak centered around channel 3500 is composed mainly of fission fragments, emitted after the absorption of either a tagged or an untagged photon. Since the signals coming from the PPADs defined the trigger, each PPAD TDC spectrum should ideally be a δ function. Electronic noise and jitter widen this distribution ($\sigma \simeq 0.4$ ns).

Figure 4.2 shows the PPAD hit distribution. The target isotopes corresponding to each of the 23 positions are given in Table 3.4. Different PPADs have different counting rates depending on the natural α radioactivity of the associated target, on its photofission probability, and on the target thickness. For example, detectors 1, 6, and 11 correspond to ^{233}U targets which have very high natural α rates, while detectors 16-22 correspond to ^{nat}Pb targets, which have a low fission cross section. The different PPAD electronic thresholds and the different target thicknesses also affect the trigger rate, which explains why the same nuclei do not have identical counting rates.

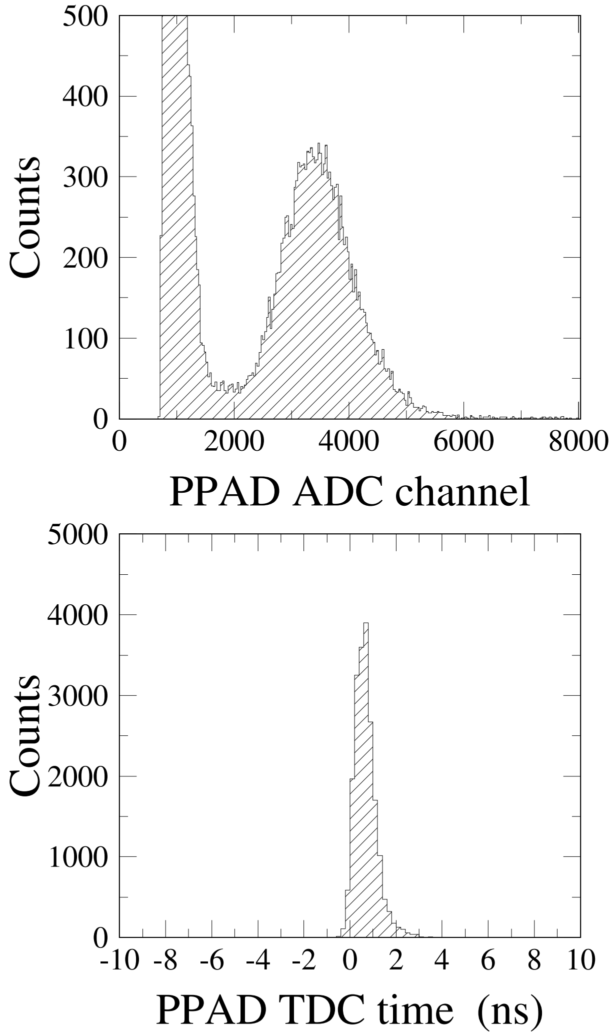

Figure 4.1: Raw PPAD ADC spectrum for ^{237}Np. The corresponding TDC spectrum was converted to a time spectrum (20 channels/ns).

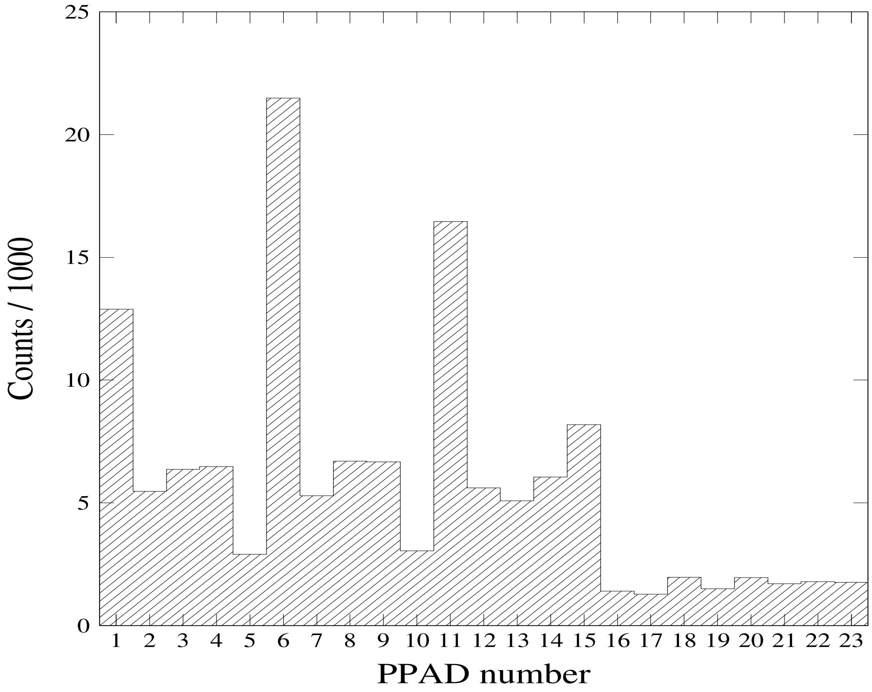

Figure 4.2: PPAD hit distribution. See Table 3.4 for the target isotopes corresponding to each PPAD position.

4.1 Timing calibration

Several time corrections have been made in order to achieve the best coincidence time resolution between the tagger TDCs and the PPADs.

In order to properly subtract background events, good statistics are needed. For this purpose we added the data for different PPADs having the same target isotope and also the data for the 61 tagger T-channels. If the signals from the various tagger channels as well as those corresponding to different PPADs are not well aligned in time, the resulting time spectra would not have an optimal time resolution. Thus, two timing corrections were necessary, one for the timing alignment of the 61 tagger T-counters and the other for the individual PPADs.

In order to determine these corrections, we fitted the time peak for the individual T-counters with a Gaussian distribution. The centroids of these Gaussians gave the offsets to be applied to the tagger timing. Similarly, 23 offsets were found for the individual PPADs.

The PPAD self-timing TDC spectra provided the correction for the trigger time jitter.

Lastly, a correction was made for the so-called discriminator walk, which occurs when regular leading-edge discriminators are used, and is due to different amplitude signals reaching the discriminator threshold at different times. This correction becomes more important when, as in the present experiment, there is a wide range in the energy distribution of the detected particles (*e.g.*, fission fragments).

Thus, the final tagger timing $\Delta t(k)$ for the k^{th} tagger channel is given by:

$$\Delta t(k) = t_T(k) * conv - \Delta t_T(k) - \Delta t_P(j) - t_P * conv - \Delta t_A(i) \qquad (4.1)$$

where $t_T(k)$ is the raw tagger TDC channel, $conv = 0.05$ ns/channel is the conversion factor, $\Delta t_T(k)$ is the correction factor due to T-counter alignment, $\Delta t_P(j)$ for the j^{th} PPAD is the correction factor due to PPAD alignment, t_P is the raw PPAD TDC channel, and $\Delta t_A(i)$ is the walk correction for the i^{th} PPAD ADC channel.

Figure 4.3 illustrates the effect of these four kinds of corrections individually. In each plot one of the corrections was turned off while the other three were applied. Figure 4.3(a) shows the tagger time versus the T-counter number for all the PPADs summed together, before the T-channels have been aligned in time. Similarly, Fig. 4.3(b) shows the tagger time versus the PPAD number for all the T-counters summed together, without the time correction for the PPAD alignment. As mentioned earlier, for statistical convenience, we added data from all T-counters. Also, though there is no reason to add data from all 23 PPADs, we did add data from the ones corresponding to the same target isotope (3 for each of the actinides and 7 for lead) when we determined the fission-fragment yield per isotope. This implies that the PPADs had to aligned as well. Figure 4.3(c) and (d) show how the timing spectrum would look without the walk and the jitter corrections respectively.

In Fig. 4.4 we present the global effect of all of our timing corrections. Figure

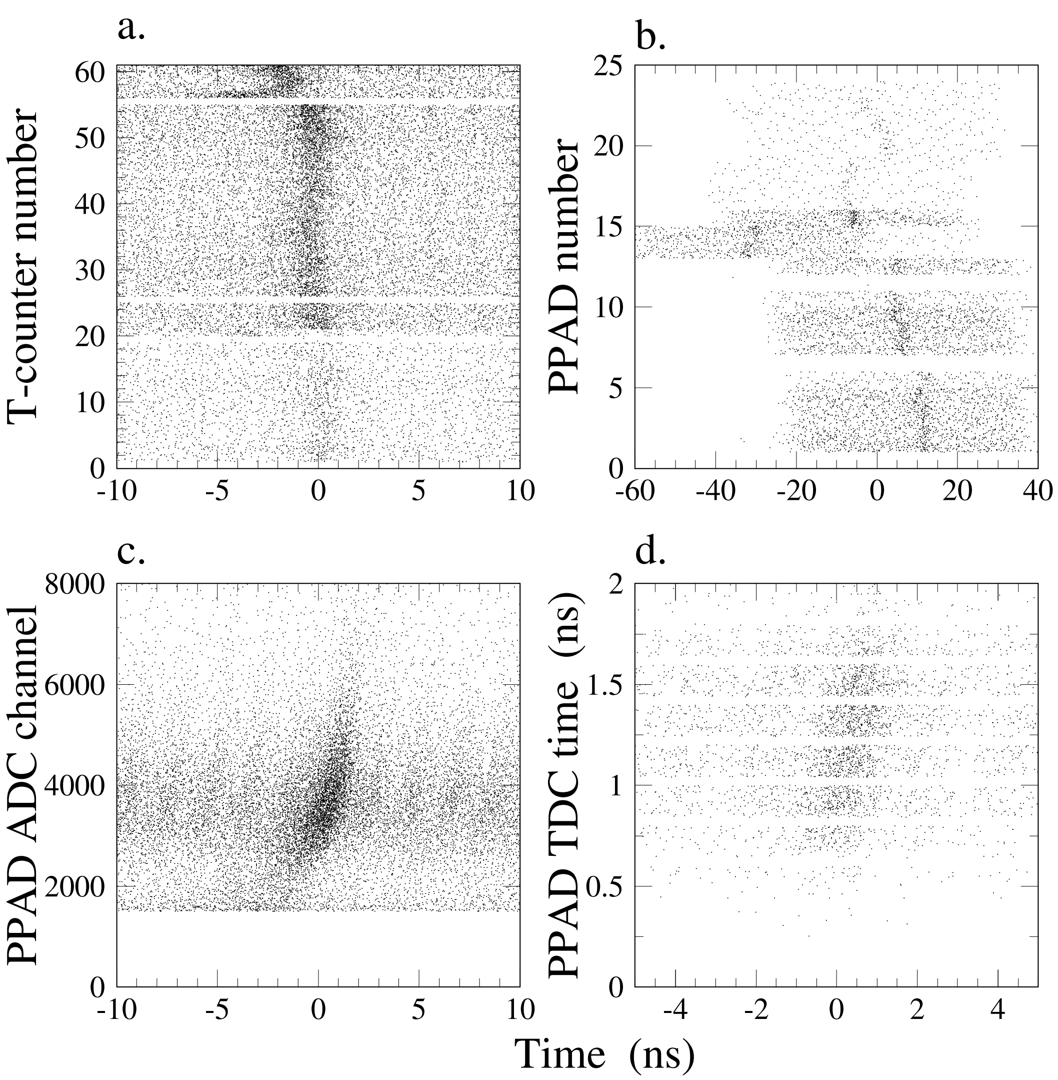

Figure 4.3: The effect of each timing correction on the tagger timing: (a) T-counter time alignment, (b) PPAD time alignment, (c) walk, (d) jitter.

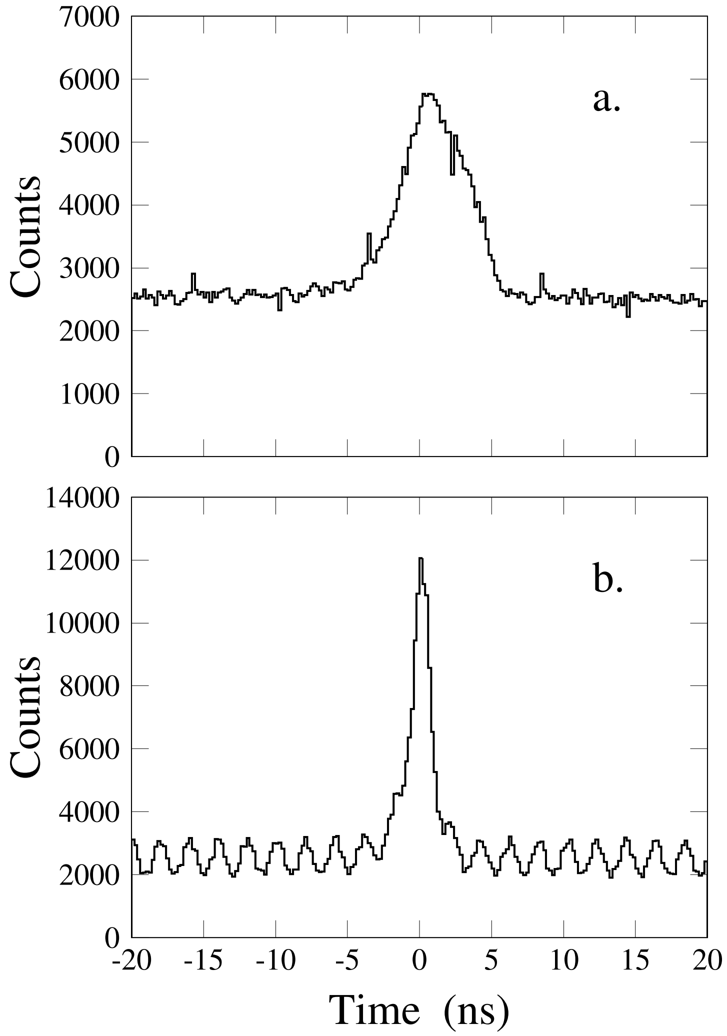

Figure 4.4: Tagger TDC spectrum before and after applying the timing corrections. Data from all T-counters and from all PPADs were added together.

4.4(a) shows the raw tagged TDC spectrum for all the tagger channels and all PPADs, before any correction was applied (FWHM = 5 ns). Figure 4.4(b) shows the same spectrum after all corrections have been applied (FWHM = 1.5 ns) and illustrates that the time resolution has been much improved and that the RF structure of the CEBAF beam can now be discerned clearly .

4.2 Event-selection criteria

4.2.1 Identifying the triggering PPAD

For a given event, there can be a signal in more than one PPAD, in which case the trigger would not be uniquely defined. In order to determine which of the detectors gave a signal, we required a count in both a PPAD ADC and TDC spectrum. Under these conditions, the multiplicity distribution of the PPADs consists of the number of detectors per event having a count in both ADC and TDC spectra. Fortunately, at the low rates of this experiment, the multiplicity distribution shows that 98.5% of the total events were events in which only one PPAD had given a signal. For further analysis we used only those events for which the PPAD multiplicity was equal to one and we applied a correction of 1.5% to compensate for the rest.

4.2.2 Energy threshold

The ADC spectrum (Fig. 4.1) shows a valley between the α particles and the fission fragments, but not a complete separation. A certain degree of overlap between the two distributions is present, depending on the nature of the target isotope but also on the characteristics of the particular detector. Figure 4.5 illustrates these differences for six detectors with different targets. While for the actinides, the tail of the α distribution contributes only a small amount into the fission peak region, this is not the case for lead.

In order to reduce the α background level in the TDC spectrum, one would like to eliminate the α events from the data as much as possible. For the actinide isotopes,

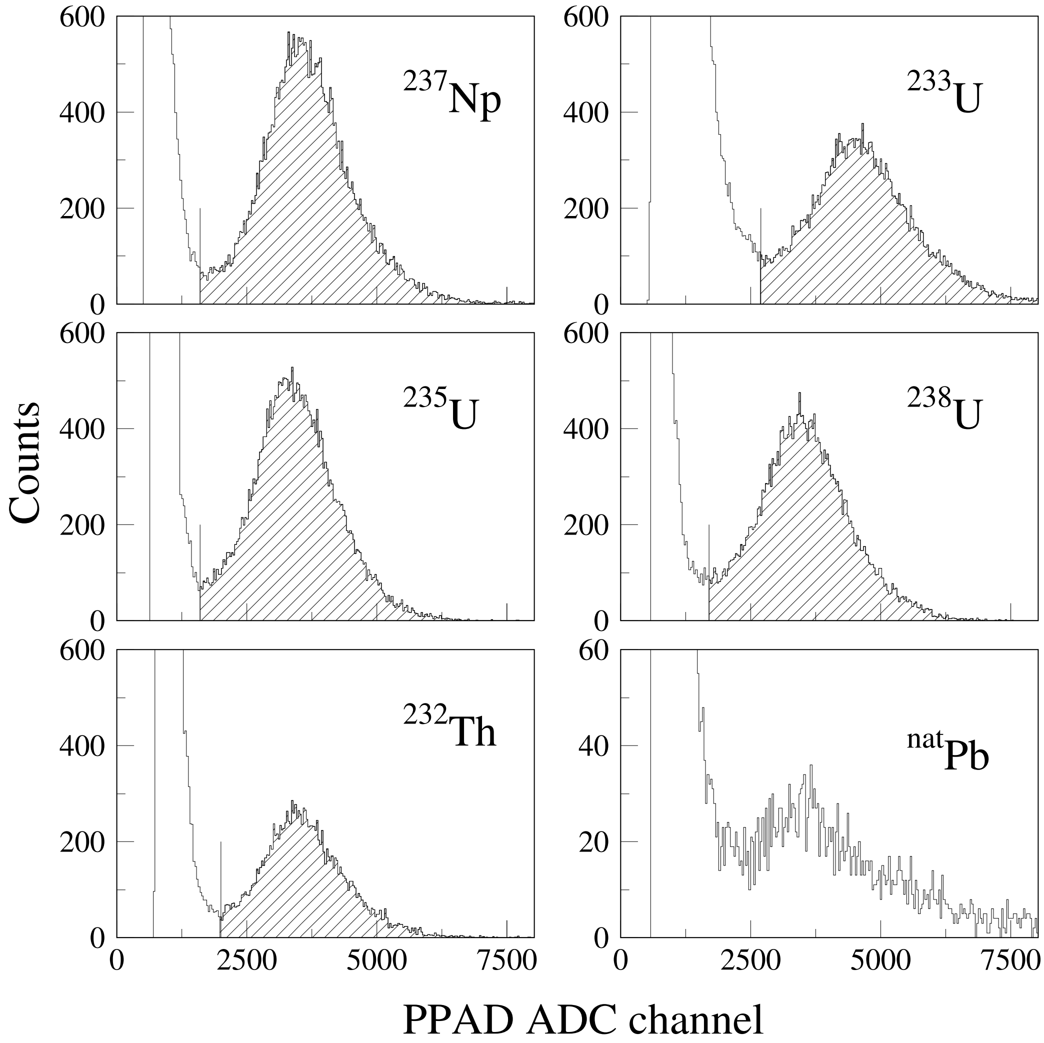

Figure 4.5: PPAD ADC spectra corresponding to the six target isotopes used in the present experiment.

the yield of coincidence events was estimated only after placing a cut in the lowest part of the valley. This assumes that the contribution of the α particles to the fission yield in the overlap region is compensated by the fission events with energies below the value of the ADC cut. Thus, the fission fragments are taken to be the events above this cut. For the case of lead, where the α count is high compared to the fission rate, a different procedure was applied, described in more detail in Sec. 6.2.2.

4.2.3 Left-right cut

From Sec. 3.3.2 we recall that the timing detectors of the photon tagger consist of thick scintillators with PMTs at both ends (called left and right T-counters). In Fig. 4.6 we show the number of events which had a signal in both the left and right T-counters relative to the total number of counts, both within the coincidence peak, for two runs at different incident energies. The very small difference between runs at

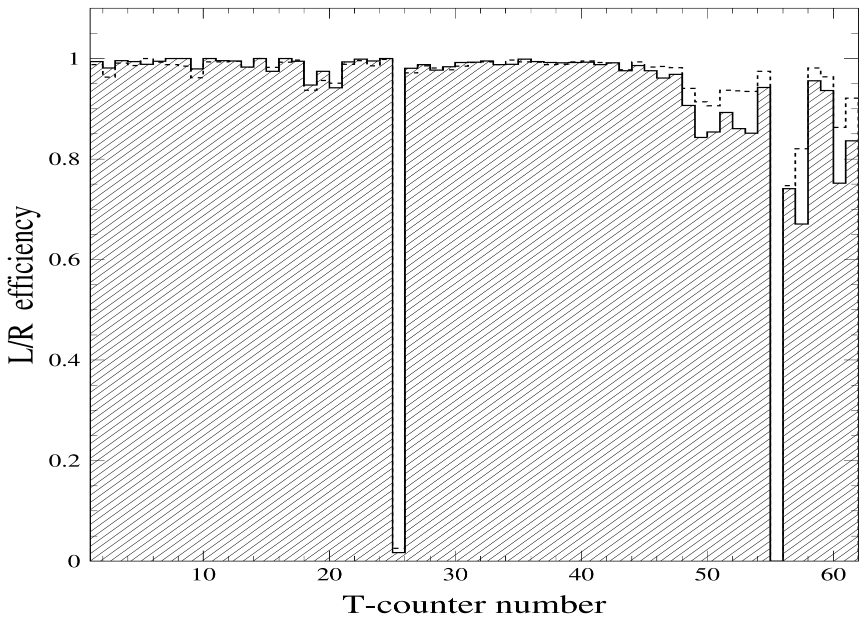

Figure 4.6: Number of events which had a signal in both the left and right T-counters relative to the total number of counts, within the coincidence peak for $E_0 = 1.7\ GeV$ (full histogram) and $E_0 = 4.0\ GeV$ (dotted histogram).

the two different energies provides an indication of the stability of the PMT gains. The ratio plotted in Fig. 4.6 drops to values below unity for T-channels above 48, which is also the region where high background rates are present (see Fig. 3.4(b) and Sec. 3.3.2 for explanation). The suppression of this background in T-counters 48-61 is discussed in the next section.

For our analysis we used only the events which had both left and right T-counters present. If the tagger time is defined as the average of the times from the left and right ends of the scintillator, then the sum of these two times is independent of the starting point in the scintillator. This implies that the time jitter due to lateral spread of the electrons is minimized.

4.2.4 E - T matching

Electrons coming from the radiator and bent by the tagger magnet pass through both the E- and the T-counters. These two detector planes are arranged such that electrons with appropriate trajectories can pass only through specific E- and T-counter combinations. This geometric correspondence is determined using a Monte-Carlo simulation with given magnetic field maps and measured positions of the detectors as input. The E-T geometric correspondence is displayed in Fig. 4.7. The E-counter number, on the abscissa, is approximately linear in electron energy, but the T-counter number, on the ordinate, is not (see Sec. 3.3.2). The discontinuity in the slope marks the transition from the small T-counters to the larger ones. The events which do not satisfy the geometric matching between the E-and the T-counters are due to background and are not included in the analysis.

In addition to the E-T geometric correlation, a narrow time coincidence is equally important for reducing the number of accidentals between the E- and the T-counters. Events are kept only if the time difference between the E- and the T-counter is within the time coincidence peak of the two, which is the hatched area in Fig. 4.8.

Figure 4.9 shows three histograms: 1) the T-counter hit distribution without any cut on the E-counters, 2) after requiring that the E-counter hits are the geometrically allowed ones, and finally 3) after adding the time coincidence requirement. By requir-

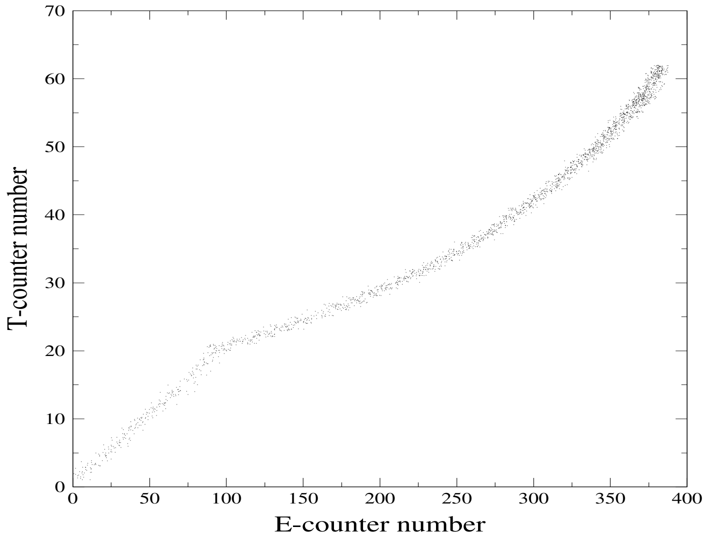

Figure 4.7: Geometric correspondence between the E- and the T-counters.

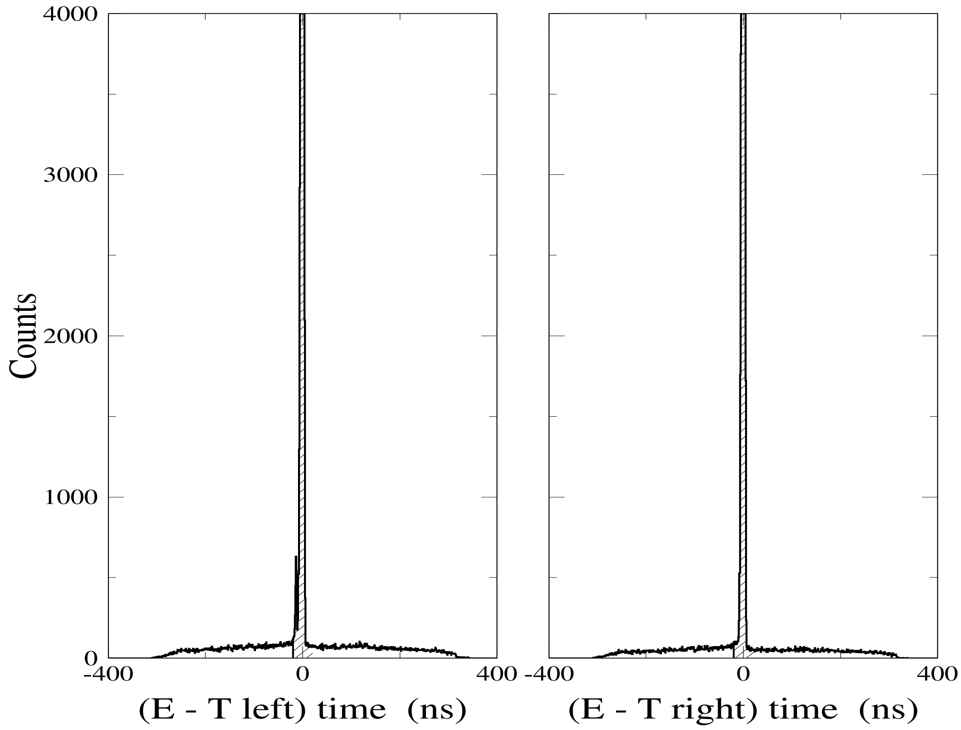

Figure 4.8: Time correspondence between the E- and the T-counters. The ordinate was suppressed by a factor of 10. The maximum value of the E-T coincidence peak extends up to 3×10^4 counts. The secondary peak is due to the out-of-range timing of T-counter 22 left.

ing a tight time coincidence between a T-counter and the corresponding E-counters, the background from secondary sources in the tagger focal plane was significantly reduced, especially for T-counters 48-61.

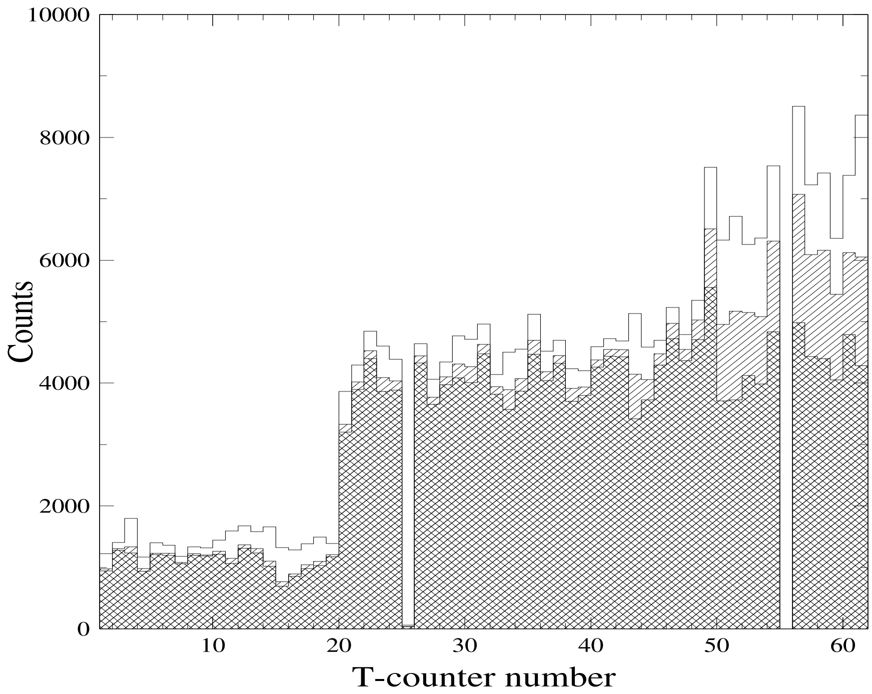

Figure 4.9: T-counter hit distribution (open histogram), with geometrically matching E-counters (hatched histogram), and with time matching as well (double-hatched histogram).

4.3 Background subtraction

The time coincidence between a PPAD signal and the associated electron detected in the tagger focal plane results in a peak in the tagger TDC spectrum, as shown in Fig 4.4. This peak rests on an extended background of random coincidences due to events caused by untagged photons and by un correlated radioactive decay products. The 2-ns RF structure of the electron-beam bunches is evident.

Because of their different levels of natural radioactivity, the background subtraction has been done for each isotope separately. To get better statistics (and thus a better fit), data from all targets of a given isotope, as well as from all T-counter channels, have been added together. This spectrum is shown in Fig. 4.10(a) for ^{238}U.

The random background has been fitted with a function consisting of a sum of Gaussians at regular 2-ns intervals, added to a linear function. In order to estimate the amount of background under the true coincidence peak, this fit has been interpolated through the region of the coincidence peak. By subtracting the random background given by the fit-function from the experimental spectrum, we obtain the spectrum shown in Fig. 4.10(b), where the coincidence peak is now seen to rest on essentially zero background.

After a good fit has been achieved for the high-statistics spectrum, the fit function was then subtracted from individual tagger-channel spectra, taking into account the appropriate scaling factors. This scaling factor was calculated by integrating the same background regions in the two spectra and taking the ratio of the two areas. For illustration, the resultant peak after the subtraction for a single tagger channel is shown in Fig 4.11. For each tagger channel, the *yield of real fission-fragment events* is then given by the area underneath this peak.

To evaluate the *statistical uncertainty* δY_{FF} of the fission-fragment yield Y_{FF}, one has to write the yield as

$$Y_{FF} = N_P - S \cdot N_B \tag{4.2}$$

$$(\delta Y_{FF})^2 = (\delta N_P)^2 + S^2(\delta N_B)^2 \tag{4.3}$$

where N_P are the counts in coincidence peak region before background subtraction; N_B are the counts in the random region that was fitted; and $S = \Delta t_P/\Delta t_B$ is a scaling factor taking into account the difference of the time intervals for the two regions. These quantities are illustrated in Fig. 4.12. Both N_P and N_B have statistical uncertainties proportional to the square root of the number of counts, so that

$$\delta Y_{FF} = \sqrt{N_P + N_B \cdot S^2} = \sqrt{N_P + N_B \cdot (\Delta t_P/\Delta t_B)^2}$$

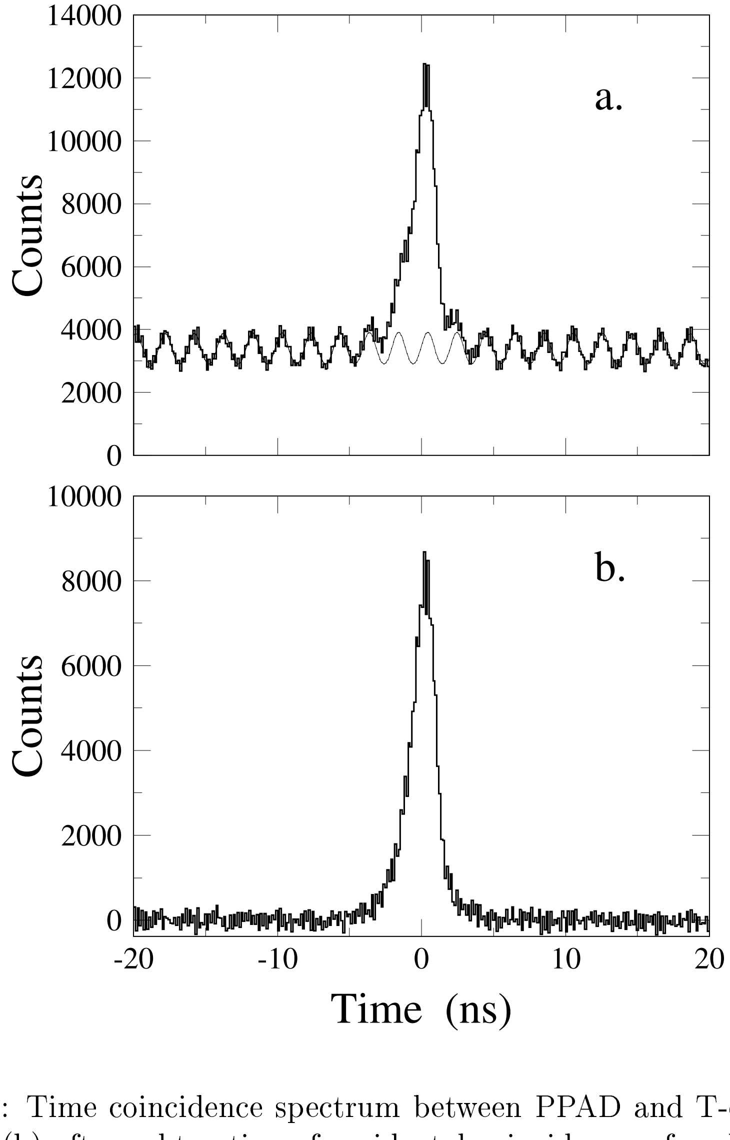

Figure 4.10: Time coincidence spectrum between PPAD and T-counter signals: (a) before and (b) after subtraction of accidental coincidences, for all T-channels added together.

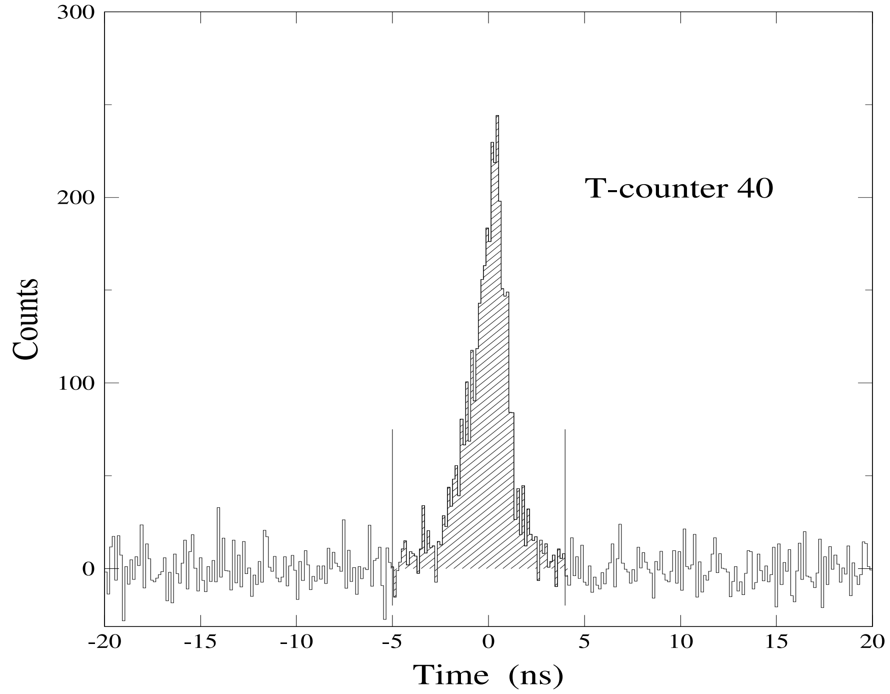

Figure 4.11: Fission-fragment coincidence peak for ^{238}U and T-channel 40. The vertical lines define the time interval for which the yield of real fission-fragments events was determined.

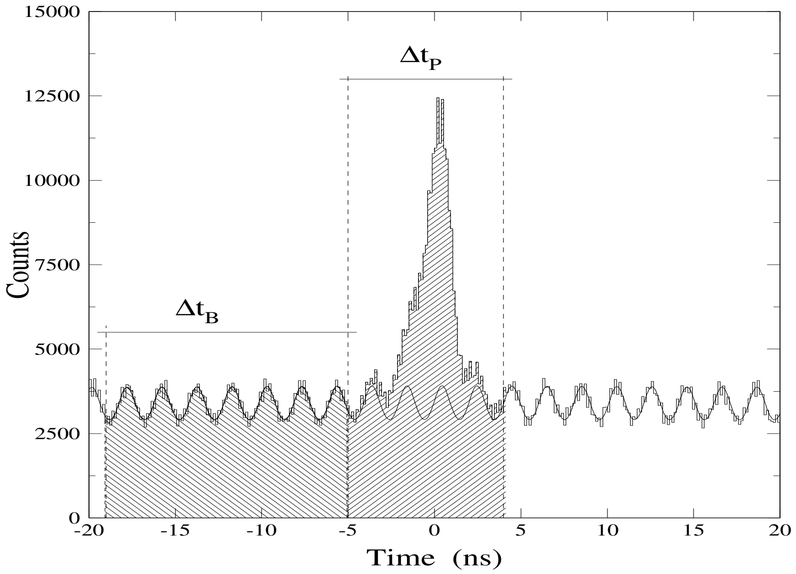

Figure 4.12: TDC spectrum for ^{238}U. The hatched areas define the coincidence peak and the random region that was fitted. The vertical lines define the time intervals Δt_P and Δt_B for the two regions.

Chapter 5

Normalization

In Sec. 3.3.3 we defined the *tagging efficiency* and we also described the way in which we did the measurements during the tagging-efficiency runs. A tagging-efficiency run was carried out on an approximately daily basis in order to study possible variations of this normalization factor in time. The available tagging-efficiency runs for each data set are presented in the timeline in Fig 5.1.

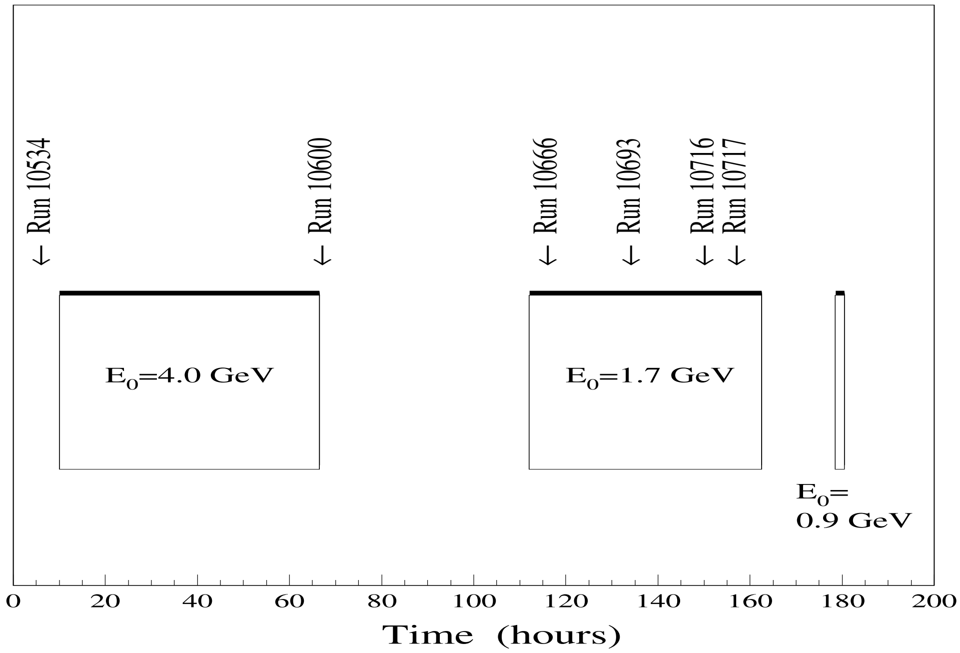

Figure 5.1: Timeline of the experiment, indicating the available tagging efficiency runs.

The lead-glass detector was placed in the photon beam line *at the same position* as the fission chamber. Data from the tagging-efficiency runs were used under the assumption that the lead-glass detector has 100% efficiency for the detection of photons. Thus, the integral of the lead-glass time spectrum, after background subtraction, gives the number of incident photons striking the detector, while the total number of tagging electrons detected in the tagger focal plane corresponding to these bremsstrahlung photons was counted by the T-counter scalers. The ratio of these two numbers gives the tagging efficiency per T-channel. The total photon flux per T-channel was then obtained by multiplying the tagging efficiency by the number of tagging electrons during a data run.

5.1 Calibration, cuts, background subtraction

5.1.1 Timing calibrations

As mentioned before, the trigger for the tagging-efficiency runs was the Master OR of all the T-counter channels. Thus, the tagger T-counter TDCs were self-triggered, their time spectra being δ-functions widened by electronic noise. In this case the important timing information is contained in the TDC spectrum of the lead-glass detector. The distribution of the raw TDC spectrum versus the raw ADC spectrum for the lead-glass detector is shown in Fig. 5.2, where data from all of the T-counters were added together.

The timing peak is quite wide (FWHM $\approx$ 4 ns), which is mainly due to the differences among individual T-channels, requiring a timing correction given by the T-counter alignment. Also, the energy dependence of the timing peak shows the necessity of the discriminator-walk correction. These two timing calibrations were done in the same way as for the data runs (see Sec. 4.1). Thus, the final timing for the k^{th} tagger channel is given by:

$$\Delta t(k) = t_{LG}(k) * conv - \Delta t_T(k) - \Delta t_A(i)$$

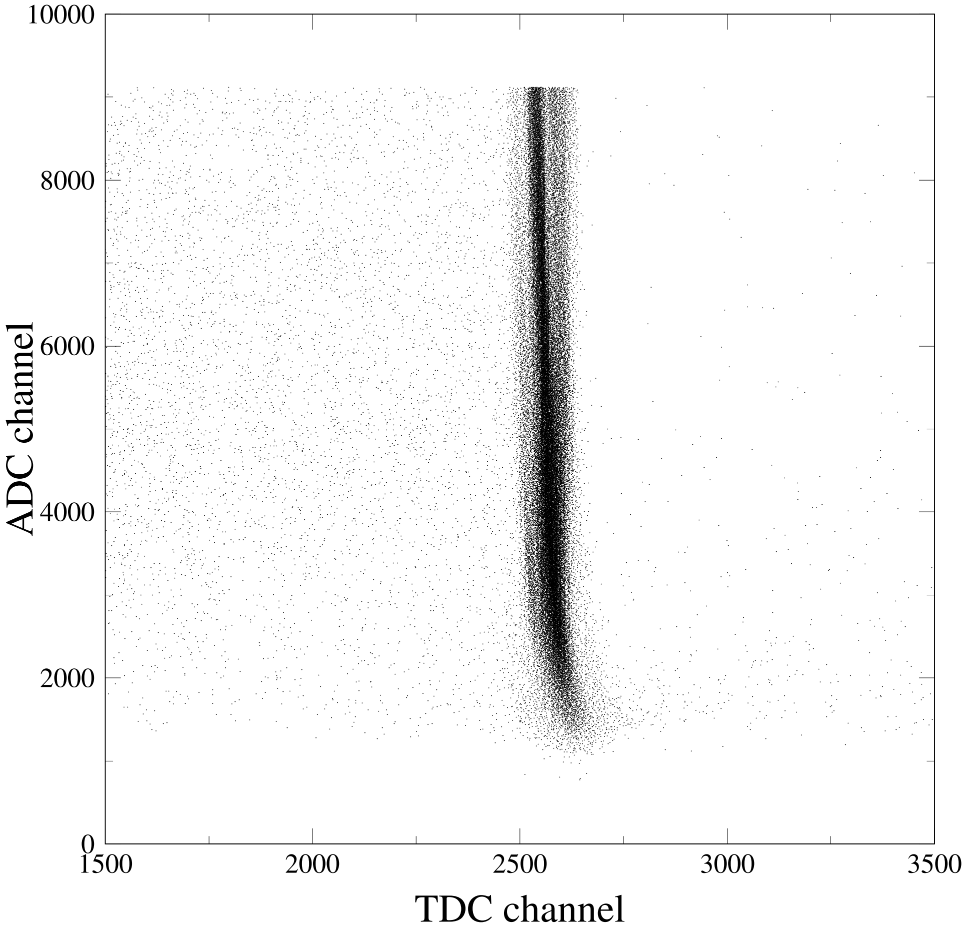

Figure 5.2: Lead-glass raw ADC spectrum versus raw TDC spectrum for all T-counters.

where $t_LG(k)$ is the raw lead-glass TDC channel; $\Delta t(k)$, conv, $\Delta t_T(k)$, and $\Delta t_A(i)$ have the same meaning as in Sec. 4.1. The effect of the two timing corrections is shown in Fig. 5.3. Fig. 5.3(a) represents the raw lead-glass TDC spectrum for all tagger channels, while Fig. 5.3(b) represents the same spectrum after the corrections have been applied, demonstrating that the resulting time resolution (FWHM $\approx$ 2 ns) is compatible with the lead-glass/tagger T-counter system.

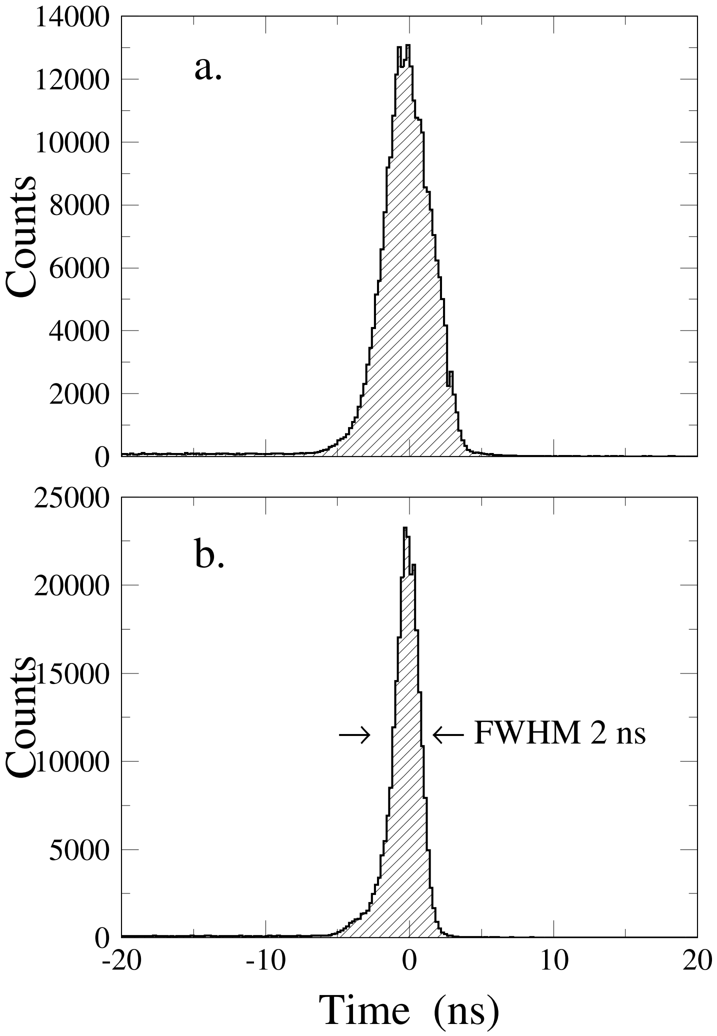

Figure 5.3: Lead-glass TDC spectrum for all T-counters (a) before and (b) after applying the timing corrections.

5.1.2 Basic cuts

To obtain the proper normalization, it is necessary to treat both the production and the tagging-efficiency data in exactly the same way. In other words, the events kept for further analysis have to be defined using exactly the same cuts. The cuts applied to the data were the requirements to have

- an event in both the left and right T-counters,
- a corresponding E-counter hit for each T-counter hit, correlated both geometrically and in time.

Thus, by considering only events which satisfy the left-right cut and the E-T matching requirement, both for the data and for the tagging-efficiency runs, we did not have to apply any further corrections, *e.g.*, for the events which had a left or right signal *only*, or to compensate for the inefficiency of the E-counters. Furthermore, we checked that if we do apply the L-R corrections (see Sec. 4.2.3) for both the data runs and the tagging-efficiency runs, we get similar results, below T-channel 48, as if we do not apply them. For the higher T-channels, where higher background rates are present, the L-R correction helps to reduce this background by at least 10%.

5.1.3 Background subtraction

Figure 5.4(a) shows the corrected coincidence time spectrum over the dynamical range of the TDC, using an expanded ordinate scale. The events occurring after the time peak are due to random background (caused by cosmic rays, *etc.*). These events have to be subtracted from the total number of events seen by the detector. This was done by assuming a flat background distribution to the right of the peak, used to determine the number of counts per ns. This level of background was then subtracted from the entire spectrum. The result is shown in Fig. 5.4(b), where one can see that the background level to the right of the peak is essentially zero. Also, to the left of the coincidence peak, the stolen events (discussed in the next section) have the expected distribution of Poisson statistics.

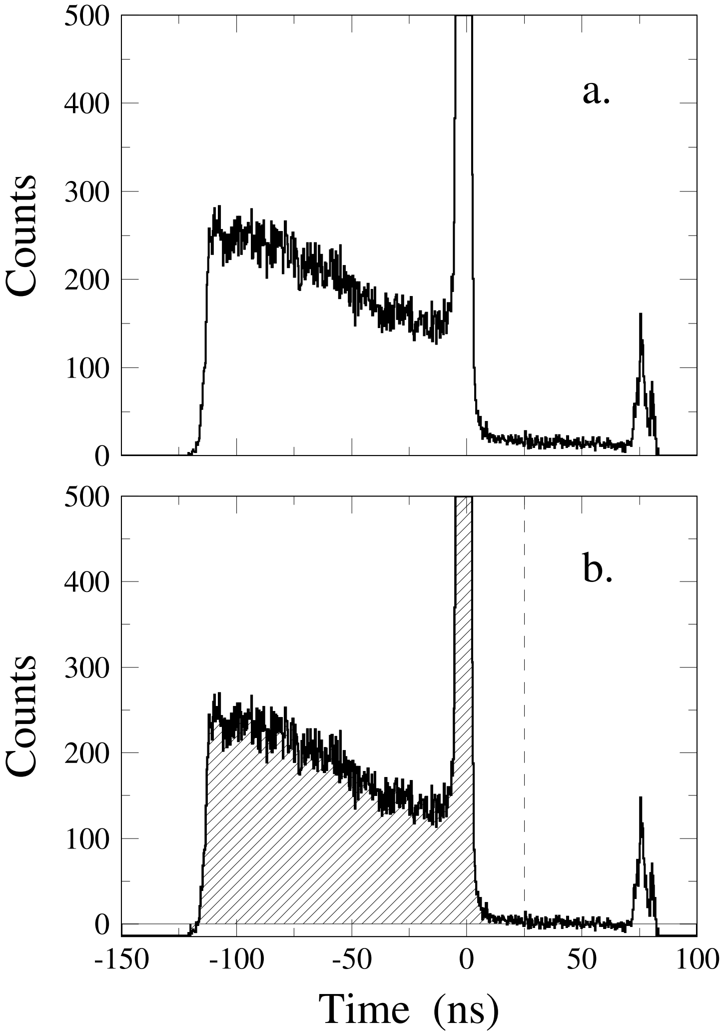

Figure 5.4: Lead-glass TDC spectrum for all T-counters: a. before, and b. after background subtraction. The integral of the hatched area (defined by events prior to the dashed line), gives the number of photons counted by the lead glass. The ordinates were suppressed by a factor of 100. The maximum value of the peak extends up to 4×10^4 counts.

5.2 Photon flux determination

5.2.1 Photon count

The number of photons per T-channel counted by the lead glass is given by the integral of the TDC spectrum to the left of the dotted line in Fig. 5.4b. The events prior to the coincidence peak are referred to as *stolen coincidences*. They occur when the STOP signal in the lead-glass TDC is generated by a photon corresponding to an earlier accidental electron which was not detected in the focal plane. The TDC, being already stopped, cannot record the photon signal which would have been under the coincidence peak, and whose associated electron was detected by the tagger (and counted by the tagger scalers).

5.2.2 Correction of scaler readings

The number of electrons detected in the tagger focal plane was counted using the tagger T-counter scalers. The scalers are read and cleared every 10 s. If the operating conditions had been stable, *i.e.*, constant electron beam current, emittance, background, *etc.*, then there would have been no time variation of the scaler readings per T-channel. This was not the case, as one can see in Fig. 5.5, in which is plotted the scaler reading as a function of time for the six available tagging efficiency runs. Assuming stable conditions for the individual T-counters, the time dependence presented in Fig. 5.5 reflects the variation in the electron beam intensity.

The number of physical events registered in the 10-s interval between two scaler readings should ideally scale with the scaler readings, and this dependence should be described by a line passing through the origin with a slope equal to the prescaling factor corrected for double hits due to the T-counter overlap. In the present case, one expects a slope of $300 \cdot 1.22 = 366$, where 300 is the prescaling factor, and the 22% reflects the overlapping of the T-counters [Sob00]. Moreover, if the electron beam current were approximately constant, most of the points would be concentrated in a restricted area. In Fig 5.6 we present the scaler readings versus the number of

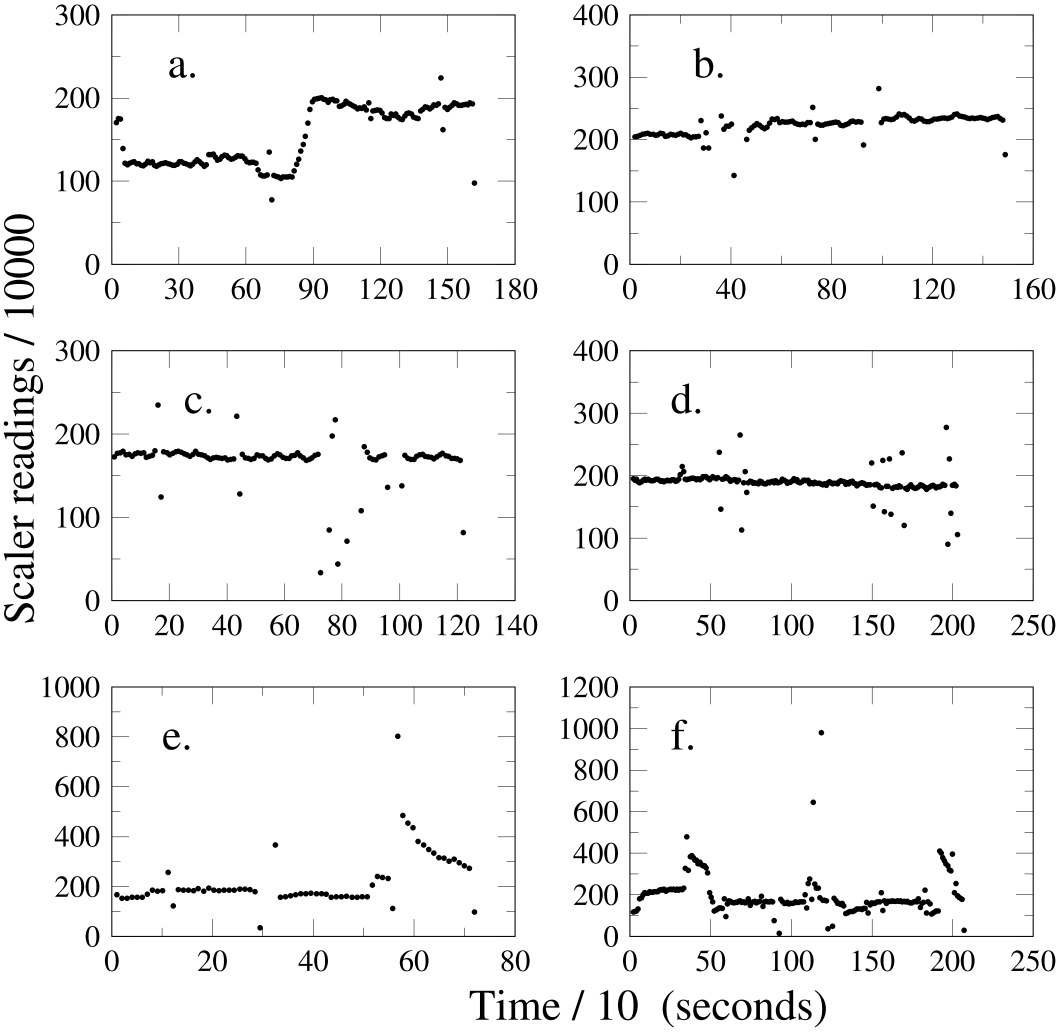

Figure 5.5: Time dependence of the integrated scaler readings over the tagger focal plane for the six available tagging efficiency runs. The spikes in (e) and (f) reflect instabilities in the intensity of the incident electron beam.

events read in the same time interval for a 1.7-GeV tagging-efficiency run, when a sudden large increase in the beam current occurred towards the middle of the run (see Fig. 5.5(f)). Due to the limited data-acquisition rate capability, the rate of recorded events remains more or less constant, while the scalers still count all of the incoming electrons. Dead-time effects on a smaller scale are corrected in hardware by gating the T-scalers on a "computer-live" signal. However, in the case of a large beam burst, this technique underestimates the dead time. The solution is to correct the scalers such that they scale with the number of events for each tagging-efficiency run and for each T-counter.

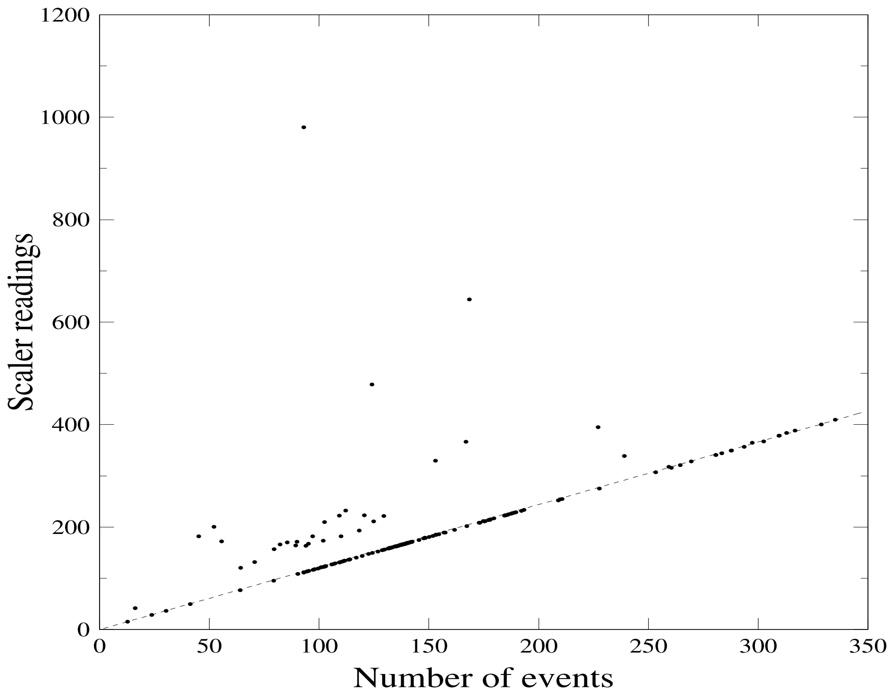

Figure 5.6: Scaler readings versus the number of events read in between these reading for the last 1.7-GeV tagging efficiency run.

Figure 5.7 shows the ratios between tagging efficiencies for the two 4-GeV runs (Fig. 5.7 (a)), and similarly for the four 1.7-GeV runs (Fig. 5.7 (b,c,d)), taking as reference the first 1.7-GeV run. The hatched and cross-hatched histograms represent the tagging-efficiency ratios before and after the scaler corrections have been applied,

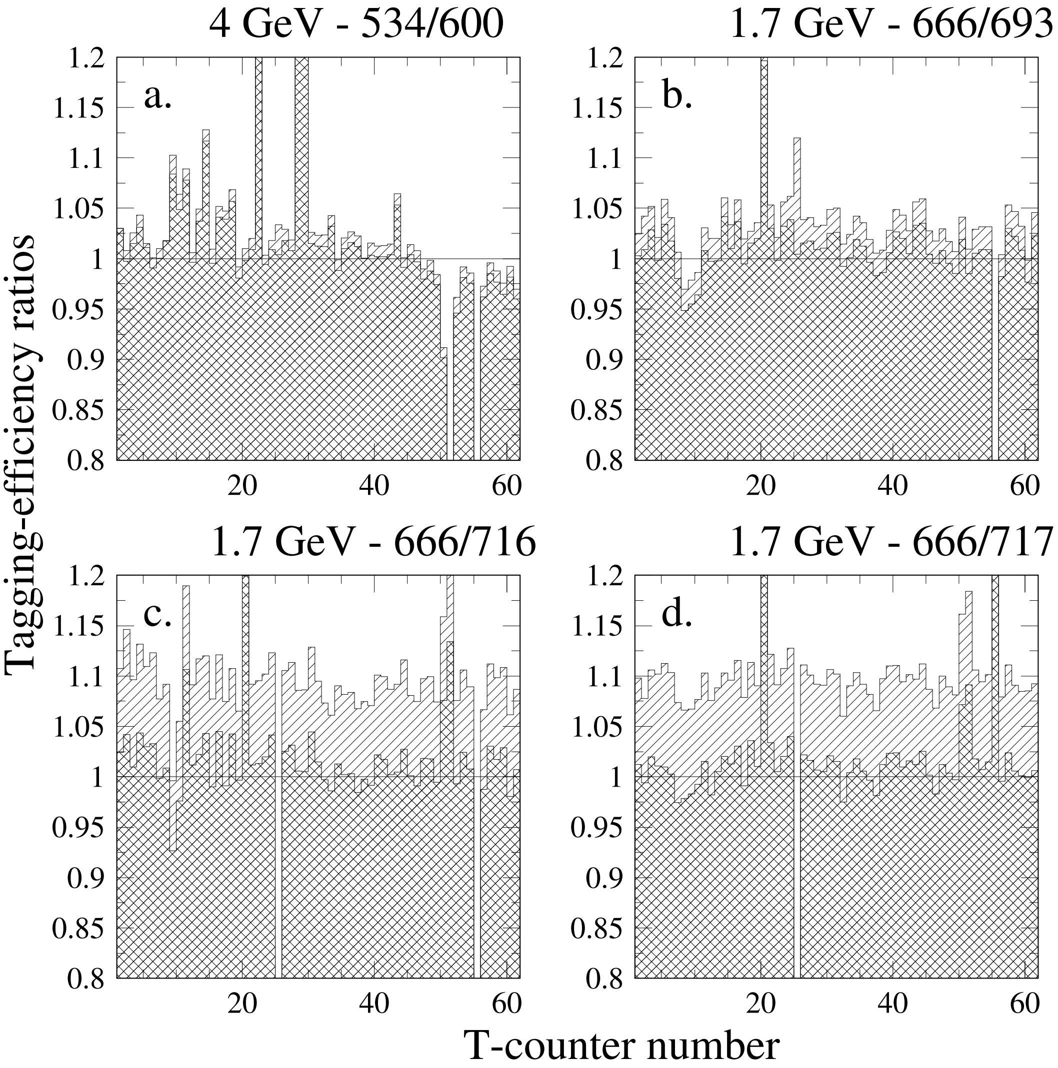

Figure 5.7: Ratios between tagging efficiencies for the two 4.0-GeV runs (a), and for the four 1.7-GeV runs (b,c,d), taking as reference the first 1.7-GeV run. The hatched and cross-hatched histograms represent the tagging-efficiency ratios before and after the scaler corrections have been applied, respectively.

respectively. One can see that the latter ratios are stable to within 2%. This allows the use of an average tagging efficiency value per energy bite.

5.2.3 Tagging efficiency

For the k^{th} tagger channel, the total number of photons N_γ detected by the lead-glass detector was divided by the number of electrons N_e detected in the tagger focal plane (corrected, if necessary), to give the tagging efficiency ϵ_T

$$\epsilon_T(k) = \frac{N_\gamma(k)}{N_e(k)} \, .$$

Although ideally, without collimation, as in this case, this ratio should be unity (or close to unity), there are several reasons why it can be less than unity. In our case, the beam-related background present at low photon energies (high T-counter number) caused a greatly increased number of electrons (for the same number of photons). This reduced the tagging efficiencies for the last 13 T-channels to values of ~0.6, as shown in Fig. 5.8. The lower values at the other end of the spectrum (high photon energies, or low T-counter number) are due to the presence of Møller electrons (which do not produce bremsstrahlung photons). Additionally, there can be local problems related to particular photomultiplier tubes and their associated hardware. These kinds of problems are more common for the E-counters. Although the distribution of the tagging efficiencies presented in Fig 5.8 is not smooth as a function of T-counter number, we proved in the previous section that the behavior for each T-channel is stable in time at the 2% level.

5.2.4 Comparison with calculation

Monte-Carlo simulations [Sob98], using the measured magnetic-field maps, were carried out for our particular beam energies. These calculations were used to determine the number of counts in each individual hodoscope scintillator and its energy boundaries, as well as the possible coincidence combinations between the E- and T-counters.

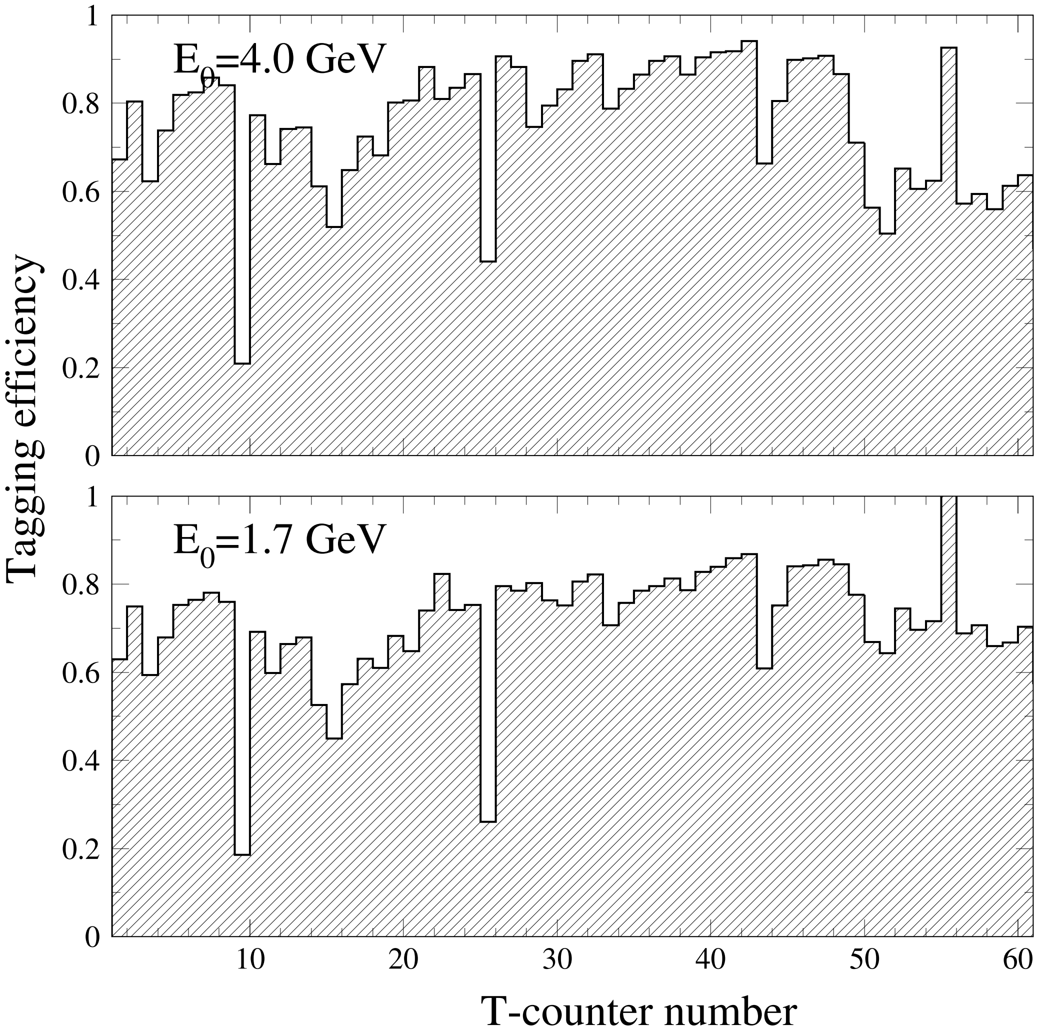

Figure 5.8: Tagging efficiency for $E_0 = 4.0\ GeV$ and $E_0 = 1.7\ GeV$.

As a consistency check, we calculated the ratio between the measured and the calculated values of $N_\gamma(k)$ and $N_e(k)$, respectively. The results are presented in Fig. 5.9 (a) and (b) for one tagging-efficiency run at each of the incident beam energies of 4.0 and 1.7 GeV, respectively. Histograms A (hatched) and B (cross-hatched) represent the ratios $N_\gamma(k)^{meas}/N_\gamma(k)^{calc}$ for the cases when we do and do not require a T-E coincidence, respectively. Histograms C (open) represent the ratios $N_e(k)^{meas}/N_e(k)^{calc}$. In Fig. 5.9 (c) and (d) we show the corresponding tagging efficiency $\epsilon_T(k) = N_\gamma(k)^{meas}$ / $N_e(k)^{meas}$ for the cases when we do and do not require a T-E coincidence, respectively.

For histograms A in Fig 5.9 (a) and (b) the agreement between data and calculation is remarkably good up to a given T-channel (no. 48 for $E_0 = 4.0$ GeV and no. 40 for $E_0 = 1.7$ GeV). This in turn demonstrates a good understanding of the bremsstrahlung spectrum and a correct way of describing it in the computational code. On the other hand, it also points out the background present at low photon energies (high T-counter number). This problem is solved by requiring the T-E coincidence, as proved by the histograms B. Histograms C, while confirming the presence of background at low photon energies, also reflect the presence of the Møller electrons at high electron energies.

5.2.5 Tagging efficiency for the 0.9-GeV run

Not having a normalization run for the 0.9-GeV data, the tagging efficiency in this case was deduced using the tagging efficiency for the 1.7-GeV data and taking into account both a change in the energy dependence across the focal plane and a change in the absolute value of the tagging efficiency.

The procedure was first checked by calculating the normalization for the 1.7-GeV data starting from the 4-GeV one, and comparing it with the measured 1.7-GeV tagging efficiency

$$[\epsilon_T(k)]^{meas}_{1.7GeV} = \left[\frac{N_\gamma(k)}{N_e(k)}\right]_{1.7GeV} . \tag{5.1}$$

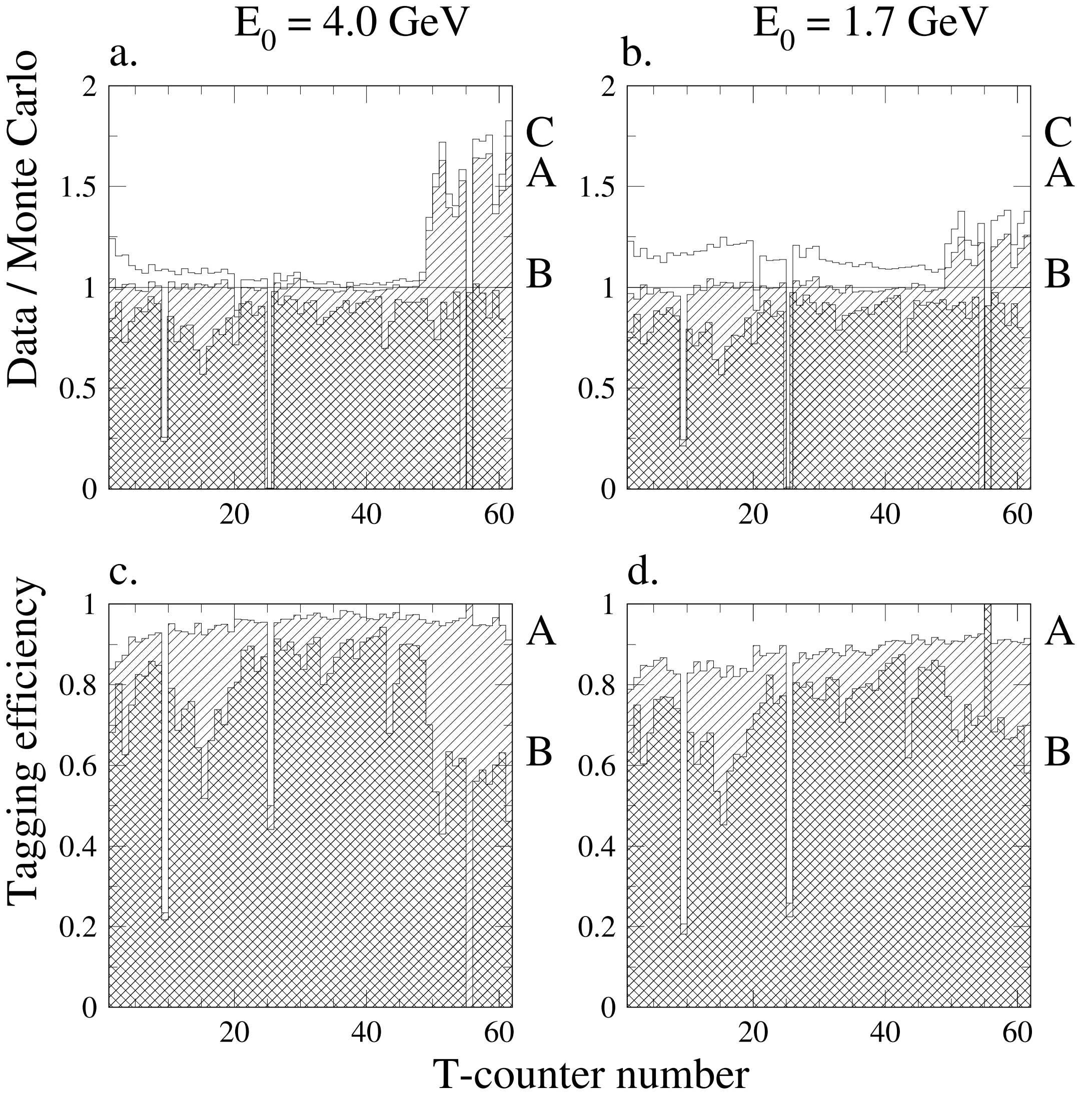

Figure 5.9: (a) and (b) show ratios between data and Monte-Carlo calculations: $N_\gamma(k)^{meas}/N_\gamma(k)^{calc}$ without (hatched) and with (cross-hatched) the T-E coincidence, and $N_e(k)^{meas}/N_e(k)^{calc}$ (open). (c) and (d) corresponding tagging efficiency ratios without (hatched) and with (cross-hatched) the T-E coincidence.

The calculated 1.7-GeV tagging efficiency was expressed as

$$[\epsilon_T(k)]^{calc}_{1.7GeV} = [\epsilon_T(k)]^{meas}_{4GeV} \cdot R^4_{1.7} \cdot F^4_{1.7} \tag{5.2}$$

where $F^4_{1.7}$ is the absolute value scaling factor. $R^4_{1.7}$ takes into account the change in the energy dependence over the focal plane, and is expressed as the ratio between counts in the random background region at two beam energies during the data runs

$$R^4_{1.7} = \left[\frac{N^{4GeV}_{ran}}{N^{1.7GeV}_{ran}}\right]^{data} . \tag{5.3}$$

The use of this ratio is based on the assumption that the change in the energy dependence is not due to the bremsstrahlung spectrum, but to other effects like the extra background or the Møller effect. This assumption is based on the fact that the bremsstrahlung spectrum is well known (see histograms A in Fig. 5.9(a) and (b) for comparison with Monte-Carlo calculations), and that its energy dependence across the focal plane does not change significantly for different beam energies.

The measured 1.7-GeV tagging efficiency, the ratio $R^4_{1.7}$, the calculated 1.7-GeV tagging efficiency, and the ratio between the measured and calculated efficiencies are presented in Fig. 5.10. The differences are of the order of a few percent, with the exception of a few T-channels, including the ones excluded from the data analysis for other reasons.

The 0.9-GeV tagging efficiency was then calculated in a similar way

$$[\epsilon_T(k)]^{calc}_{0.9GeV} = [\epsilon_T(k)]^{meas}_{1.7GeV} \cdot R^{1.7}_{0.9} \cdot F^{1.7}_{0.9} \tag{5.4}$$

where

$$R^{1.7}_{0.9} = \left[\frac{N^{1.7GeV}_{ran}}{N^{0.9GeV}_{ran}}\right]^{data} . \tag{5.5}$$

The measured 1.7-GeV tagging efficiency, the ratio $R^{1.7}_{0.9}$ of random background count, and the calculated 0.9-GeV tagging efficiency are shown in Fig. 5.11. The scaling factor $F^{1.7}_{0.9}$ was obtained by requiring good agreement of the measured cross

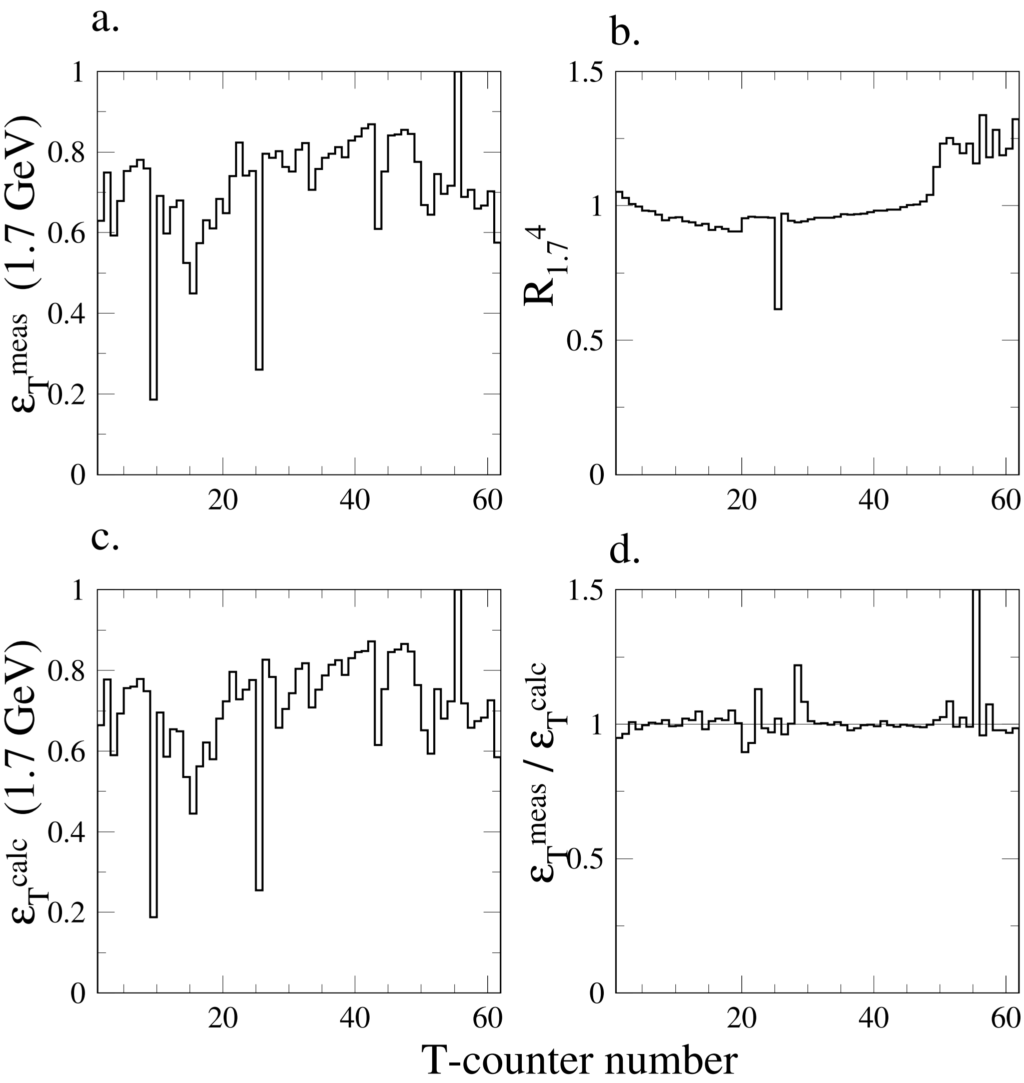

Figure 5.10: (a) Measured 1.7-GeV tagging efficiency; (b) ratio $R_{1.7}^4$ of random counts in data runs at the two beam energies; (c) calculated 1.7-GeV tagging efficiency; (d) ratio of the measured and calculated 1.7-GeV tagging efficiencies.

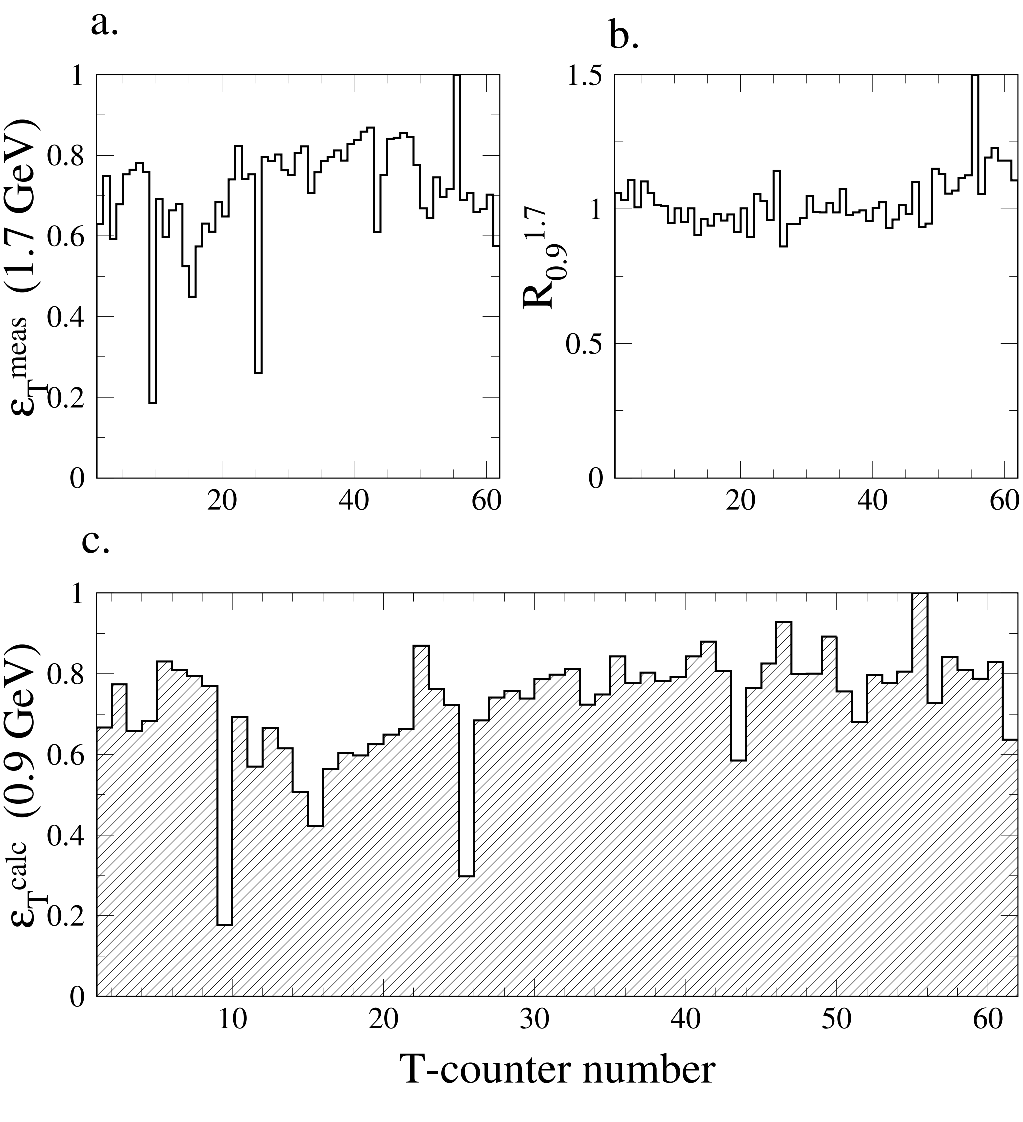

Figure 5.11: (a) Measured 1.7-GeV tagging efficiency; (b) ratio $R_{0.9}^{1.7}$ of random counts in data runs at the two beam energies; (c) calculated 0.9-GeV tagging efficiency.

	$\sigma_{\gamma F}/A$ (μb) [0.36-0.83 GeV]		
Isotope	1.7 GeV	0.9 GeV	$F_{0.9}^{1.7}$
^{237}Np	280.48 $\pm$ 0.87	218.49 $\pm$ 3.45	1.28 $\pm$ 0.02
^{233}U	242.50 $\pm$ 1.63	203.31 $\pm$ 6.46	1.19 $\pm$ 0.04
^{235}U	243.08 $\pm$ 0.84	196.37 $\pm$ 3.35	1.24 $\pm$ 0.02
^{238}U	232.18 $\pm$ 0.60	175.06 $\pm$ 2.37	1.33 $\pm$ 0.02
^{232}Th	144.48 $\pm$ 0.37	115.02 $\pm$ 1.48	1.26 $\pm$ 0.02
^{nat}Pb	18.61 $\pm$ 0.12	16.17 $\pm$ 0.45	1.15 $\pm$ 0.03

Table 5.1: Cross section per nucleon per target isotope averaged in the overlap region of the 1.7- and 0.9-GeV data, and the scaling factor $F_{0.9}^{1.7}$.

sections in the overlap region. The average cross sections per nucleon per isotope were calculated for the 360-830-MeV region and a scaling factor was found for each isotope. These values are listed in Table 5.1. The differences in the scaling factors for various nuclei are explained by the presence of nonuniformities in the target thicknesses, and the fact that larger target areas are sampled for 0.9 GeV than for 1.7 GeV.

Chapter 6

Data Analysis

6.1 Photofission cross section

In the following analysis, the data from the three PPADs of the same isotope were combined. For each isotope (labeled j) and for each tagger channel (labeled k), the experimental photofission cross section was calculated from the expression

$$\sigma_{\gamma F}(j,k) = \frac{Y_F(j,k)}{N_\gamma(k)} \frac{f_{sto}(k)}{\epsilon_{acc}(j)\ \epsilon_{det}(j)} \frac{A(j)}{N_0\ t(j)} \tag{6.1}$$

where:

$Y_F(j,k)$ is the fission fragment yield,

$N_\gamma(k)$ is the tagged photon flux,

$f_{sto}(k)$ is the stolen-coincidence correction,

$\epsilon_{acc}(j)$ is the detection acceptance,

$\epsilon_{det}(j)$ is the detection efficiency,

$A(j)$ is the target mass number (g/mole),

N_0 is Avogadro's number (1/mole),

$t(j)$ is the target thickness (g/cm^2),

$j = 1, 6$ is the isotope identification, and

$k = 1, 61$ is the tagger channel.

The above quantities will be discussed in the following subsections.

6.1.1 Fission-fragment yield

The fission-fragment yield for each actinide isotope and each tagger T-counter channel was determined as the area under the coincidence peak after background subtraction and after a cut on the fission-fragment peak in the ADC spectrum, as described in Sect. 4.3. For the case of lead, a different technique was used, which is described in Sect. 6.2.2.

6.1.2 Tagged photon flux

The tagged photon flux is determined using the electron flux and the tagging efficiency. The electron flux is registered by the T-counter scalers, which are read every 10 seconds. For one experimental run, the electron count is given by the sum of the scaler readings over the duration of a run. The total electron flux $N_e(k)$ is then given by the sum of the scaler readings for all of the runs at a given incident electron energy.

Scaler dead-time correction

The correction applied to the scaler readings for the tagging-efficiency runs, such that they scale with the number of events, was described in Sec. 5.2.2. Again, this was necessary not for small dead-time effects, which were corrected for in hardware, but for the cases when sudden and large increases in the beam current would take place. A similar situation was encountered for the data runs. The correction procedure is described below.

The time dependence of the scaler readings for a 1.7-GeV run with such a problem is shown in Fig. 6.1(a), while the time dependence of the dead time during that particular run is shown in Fig. 6.1(c). The correspondence between the same scaler readings and the number of counts is shown in Fig. 6.1(b). Ideally, this should be a line *not* passing through the origin because there will be events recorded (due to the natural radioactivity of the targets) even when the scaler count is zero.

The ratio scalers/(events-offset) was plotted and fitted with a Gaussian function. The scaler corrections for the data runs were made for values more than four standard deviations from the fit, which were corrected to the mean value of the Gaussian

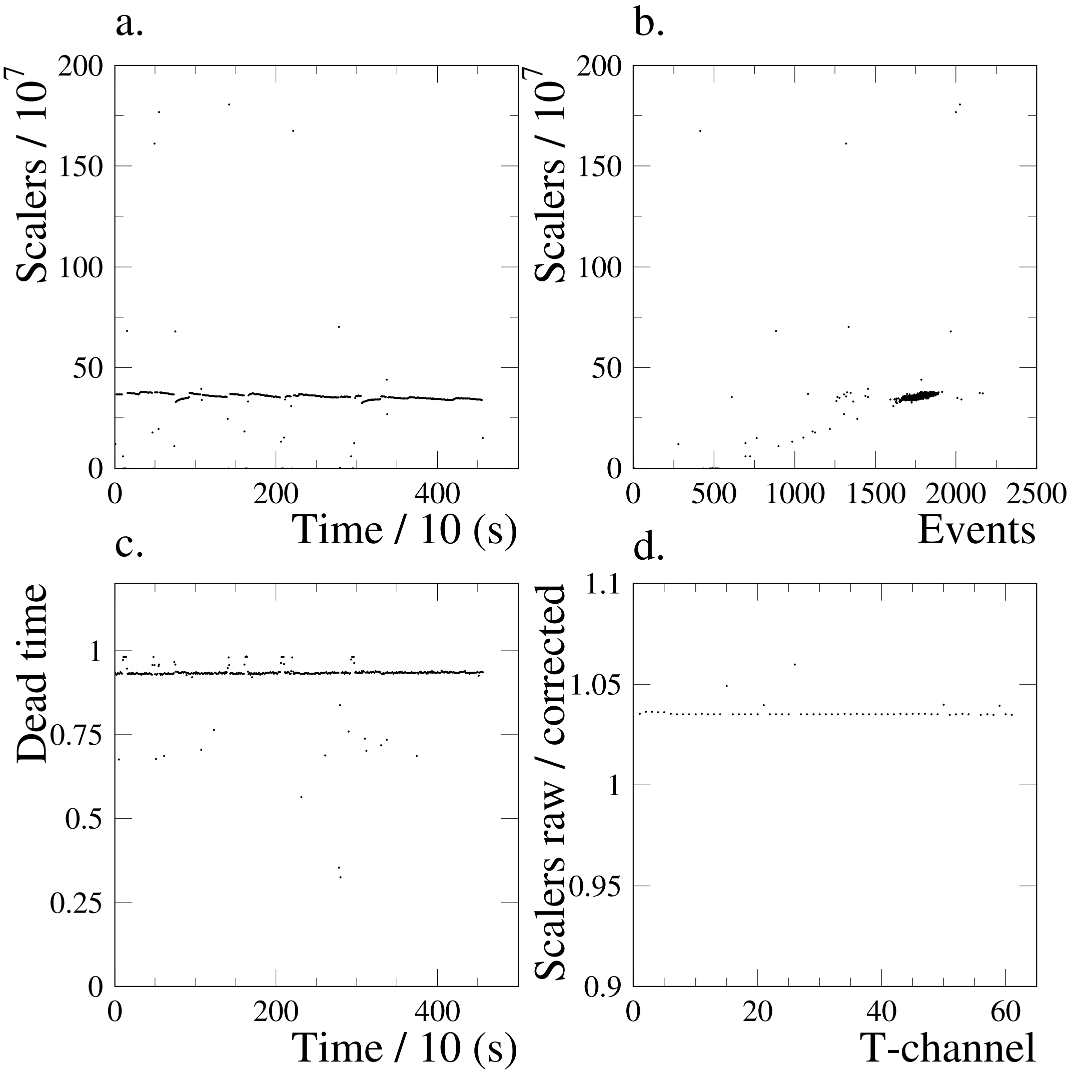

Figure 6.1: (a) Scaler readings as a function of time. (b) Scalers versus recorded events. Scalers in (a) and (b) are summed over the tagger focal plane. (c) Dead time as a function of time; (d) Ratio of raw scalers to corrected scalers as a function of T-counter number. All data are for a 1.7-GeV run.

Beam energy (GeV)	Scaler correction (%)
4.0	3.5
1.7	2.0
0.9	3.5

Table 6.1: Scaler dead-time corrections averaged over the tagger focal plane for the three data sets.

distribution. The ratio of the raw scalers and the corrected ones over the tagger focal plane is shown in Fig. 6.1(d), showing a flat distribution with the exception of a few T-counters. The overall corrections for the three sets of data are presented in Table 6.1.

In Fig. 6.1(a,b) the sum of the scalers over the tagger focal plane for one run is presented, but the correction was done for each experimental run and for each T-counter channel. The distribution of the corrected scaler readings over the tagger focal plane is shown in Fig. 6.2(a) and (b) for all of the 4-GeV and the 1.7-GeV data.

Not all of the tagged-bremsstrahlung photons reach the reaction target. Thus the electron flux has to be corrected by the tagging efficiency $\epsilon_{tag}(k)$ (defined in Sect. 5.2.3) to give the tagged photon flux $N_\gamma(k)$ striking the target

$$N_\gamma(k) = N_e(k) \cdot \epsilon_{tag}(k) = N_e(k) \cdot \frac{N_\gamma(k)^{norm}}{N_e(k)^{norm}} \, .$$

These new distributions are presented in Fig. 6.2(c) and (d). The structure in these latter distributions is different from that in the scaler distributions because they include the ratio of scaler counts during normalization and data runs. Therefore, the high T-counter-number background cancels to a large extent.

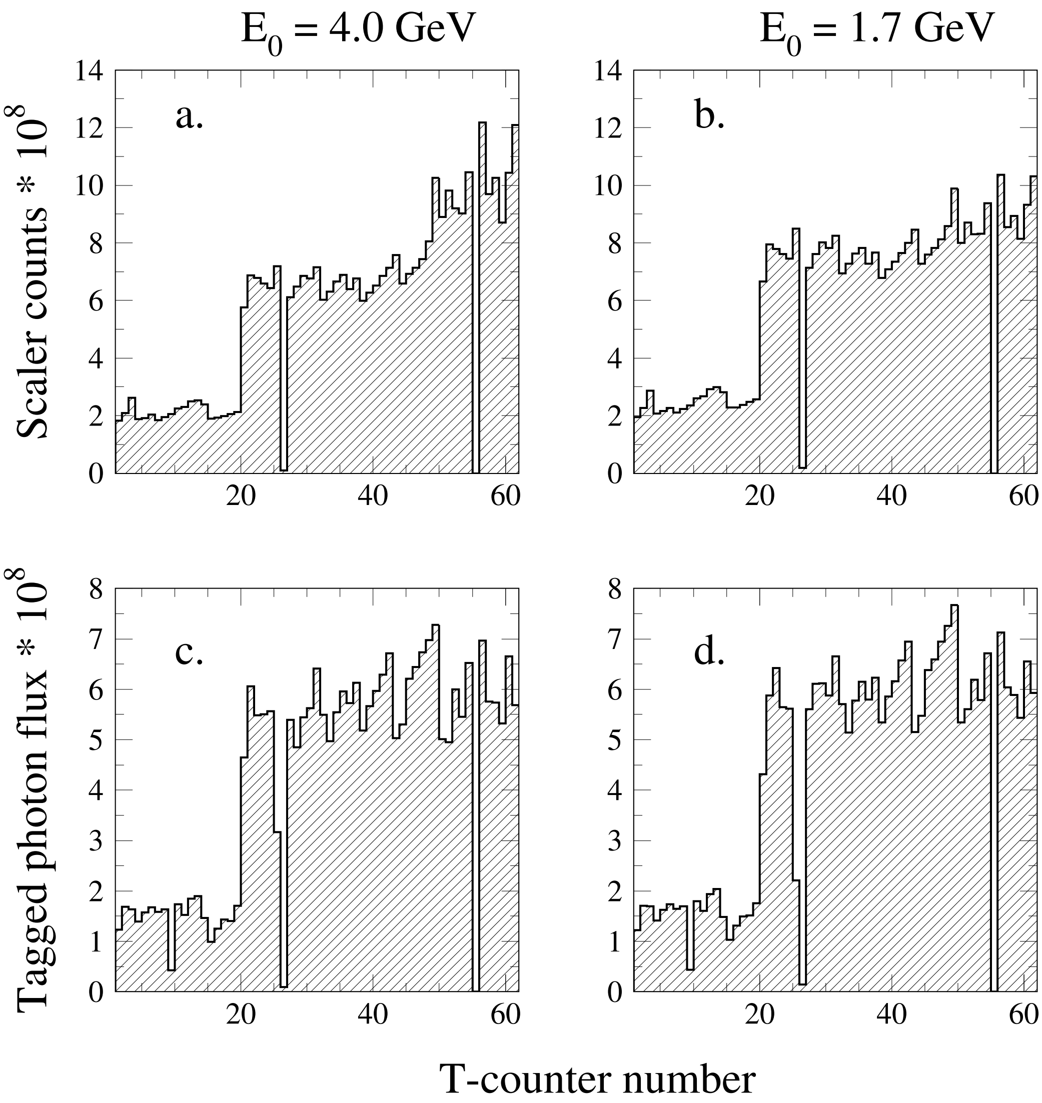

Figure 6.2: (a) and (b) Scaler counts N_e per T-channel for two electron beam energies. (c) and (d) Corresponding tagged photon flux N_γ, obtained by correcting the scaler counts by the tagging efficiency ϵ_{tag}.

6.1.3 Stolen-coincidence correction

The concept of *stolen* events was introduced in Sec. 5.2.1 related to normalization runs. They are events which should fall in the coincidence peak but do not because the TDC has been stopped by an earlier uncorrelated electron hitting the tagger focal plane within the tagger time gate. The stolen events are counted by the scalers, and thus the fission-fragment yield derived from the tagger TDC coincidence peak has to be corrected in order to account for these events. In the tagger TDC spectra, the stolen events would show up as an increased background level to the left of the time-coincidence peak (*i.e.* at earlier times).

The stolen-coincidence correction $f_{sto}(k)$ for the k^{th} tagger channel and a given run is given by [Owe90]

$$f_{sto}(k) = exp[R_e(k)\ t_{cen}(k)]$$

where $R_e(k)$ is the electron rate in the k^{th} tagger channel and $t_{cen}(k)$ is the time interval from the start of the time gate to the center of the coincidence peak. The electron rate is in turn expressed using the scaler counts $N_{sca}(k)$ in the k^{th} tagger channel during one run and the live time T_{live} of the run.

$$R_e(k) = \frac{N_{sca}(k)}{T_{live}}\ .$$

The final correction which includes data from all of the experimental runs was then obtained as a weighted average, where the weight for each run is given by the area under the coincidence peak after background subtraction.

For a typical electron rate of $R_e(k) \simeq 0.5 \times 10^6\ events/s$ and with $t_{cen} \simeq 100\ ns$, the stolen coincidence correction is of the order of 5%.

6.1.4 Geometrical acceptance

The geometrical acceptance of the target-detector combinations is the fraction of the 4π solid angle in which fission fragments produced in the target can be detected by the corresponding PPAD. This effective solid angle was estimated using a Monte-Carlo calculation [San98]. The calculation takes as input variables the incident beam energy, the beam-spot divergence, the type of bremsstrahlung radiator, the photon-tagger tagging range, as well as the positions, shapes, and sizes of the beam, radiator, fission target, collimator, and detector. It takes into account the angular distribution of the bremsstrahlung and it assumes an isotropic distribution of the fission fragments emitted by the target. The results for the geometrical acceptance are

$$\begin{aligned} \epsilon_{acc} &= 0.385 \pm 0.0036 \;\; (a) \\ \epsilon_{acc} &= 0.854 \pm 0.0034 \;\; (b) \end{aligned}$$

where (a) stands for the combinations which include a collimator and are placed perpendicular to the beam line, and (b) for those without collimator and tilted by 45° with respect to the beam line.

6.1.5 PPAD detection efficiency

At our operating conditions (15 Torr and 750 V) the PPADs have a very high efficiency for detecting fission fragments. The small inefficiency is due to the fact that the anode wire plane is not completely transparent to fission fragments. If a fission fragment hits a wire, it does not produce a signal in the detector.

$$\begin{aligned} \epsilon_{det} &= 0.975 \;\; (a) \\ \epsilon_{det} &= 0.948 \;\; (b) \end{aligned}$$

where (a) and (b) have the same meaning as in the previous paragraph. In case (a), the incident angle of the fission fragments entering the gap of the detector is limited by the collimator, and the inefficiency is given by the fractional solid angle subtended by the anode wires. The lower efficiency in case (b) is due to the fact that the fission fragments can enter at oblique angles, and thus the effective area covered by the wires is increased.

6.1.6 Target thickness

Since all of the actinide fission targets have natural α activity, their thickness and isotopic composition were determined by measuring their α-activity rates and energy spectra. The measurements, described in detail in Ref. [San00c], were done in a vacuum chamber using a silicon surface-barrier detector. A collimation system was also installed in order to restrict the α-particle emission angle, because a wide angle implies a larger energy loss in the target itself. For the energy calibration, additional measurements were done with ^{210}Po, ^{241}Am, and ^{252}Cf sources.

The measured ADC spectra are quite complex. The contributions of various isotopes in the ADC spectra were determined using Monte-Carlo simulations. The α-particle rates for ^{232}Th, ^{238}U, and ^{237}Np were obtained by integrating the parts of the ADC spectra corresponding to the given isotope. The thicknesses of these three targets were then deduced from the α-particle rates.

For the ^{235}U and ^{233}U targets, the presence of ^{238}U and ^{234}U requires the use of another method. The target thicknesses for these two isotopes were determined using correlations between thickness and ADC-spectrum width, the latter being due to the α-particle energy loss in the target itself. These correlations were determined using the ADC spectra and the known thicknesses for ^{232}Th, ^{238}U, and ^{237}Np.

For the ^{235}U targets, the amount of ^{238}U was estimated according to the composition percentage given by the manufacturer. For the case of the ^{233}U targets, the thickness was determined using the energy-loss method, while the amount of ^{233}U was determined from the counting rate. The amount of ^{238}U was then given by the difference in thickness obtained by the two methods.

All seven ^{nat}Pb targets were cut from the same big sheet. The thickness of ^{nat}Pb deposited on the Mylar substrate was given by the manufacturer (Sheldahl Corp.). The results for the 15 actinide target thicknesses (and the ^{238}U contamination if relevant), as well as those for the seven lead targets are given in Table 6.2.

Isotope	Method	Thickness	^{238}U contamination
		(mg/cm^2)	(mg/cm^2)
^{232}Th	counting rate	1.25 ± 0.02	
		1.23 ± 0.02	
		1.23 ± 0.02	
^{238}U	counting rate	1.48 ± 0.03	
		1.61 ± 0.03	
		1.23 ± 0.02	
^{237}Np	counting rate	0.94 ± 0.02	
		0.99 ± 0.02	
		0.93 ± 0.02	
^{235}U	energy loss and counting rate	0.893 ± 0.031	0.101 ± 0.010
		0.930 ± 0.033	0.105 ± 0.010
		1.066 ± 0.037	0.120 ± 0.010
^{233}U	energy loss and counting rate	0.620 ± 0.022	0.217 ± 0.008
		0.645 ± 0.023	0.235 ± 0.008
		0.566 ± 0.020	0.215 ± 0.008
^{nat}Pb	manufacturer	0.965 ± 0.097	

Table 6.2: Target thicknesses and the methods used to determine them. For ^{235}U and ^{233}U the ^{238}U contamination is given in the last column.

6.1.7 Photon energy

For each incident-electron beam energy and corresponding tagger-magnet current, there are 61 tagger T-counter channels, and they are used to determine 61 photon-energy channels. Each tagger T-counter channel covers a given fraction of the energy range of the incident photon beam $E(k) = [f_1(k) - f_2(k)]\ E_0$, where, for the k^{th} T-channel, $f_{1,2}$ are the fractions of the incident beam energy corresponding to the edges of the scintillator. These fractions are given by the Monte-Carlo program that simulates the photon-tagger optics. The corresponding photon energy for the k^{th} tagger channel is taken to be in the middle of the energy range covered by each T-counter, $E_\gamma(k) = 0.5\ [f_1(k) + f_2(k)]\ E_0$.

6.2 Special cases

6.2.1 The ^{235}U and ^{233}U targets

As was mentioned earlier, in these two types of targets, we found a non-negligible amount of ^{238}U. Consequently, the measured cross sections for both ^{235}U and ^{233}U include a contribution from the ^{238}U contamination, and had to be corrected accordingly. The procedure to derive this correction is given in Appendix A. The resulting cross sections for ^{235}U and ^{233}U were determined from

$$\sigma_i = \left(1 + \frac{A_i}{A_{238}} \frac{t_{238}}{t_i}\right) \sigma_i^{meas} - \frac{A_i}{A_{238}} \frac{t_{238}}{t_i}\, \sigma_{238}^{meas} \tag{6.2}$$

where the index i signifies either ^{235}U or ^{233}U, σ and σ^{meas} are the corrected and the measured cross sections, t and A are the thicknesses and mass numbers, and σ_{238}^{meas} is the cross section for ^{238}U obtained in the present experiment.

6.2.2 The ^{nat}Pb targets

Due to the small values of the lead photofission cross section the ^{nat}Pb data needed to be treated differently from the actinide targets. The ADC spectra for these targets indicate, as shown in Fig. 6.3, that the contribution of coincident α particles (from the (γ, α) reaction) underneath the fission-fragment peak is significant. Furthermore, in Fig. 6.3 the ADC spectrum of the Mylar substrate is superimposed upon that of ^{nat}Pb, showing that its contribution is non-negligible.

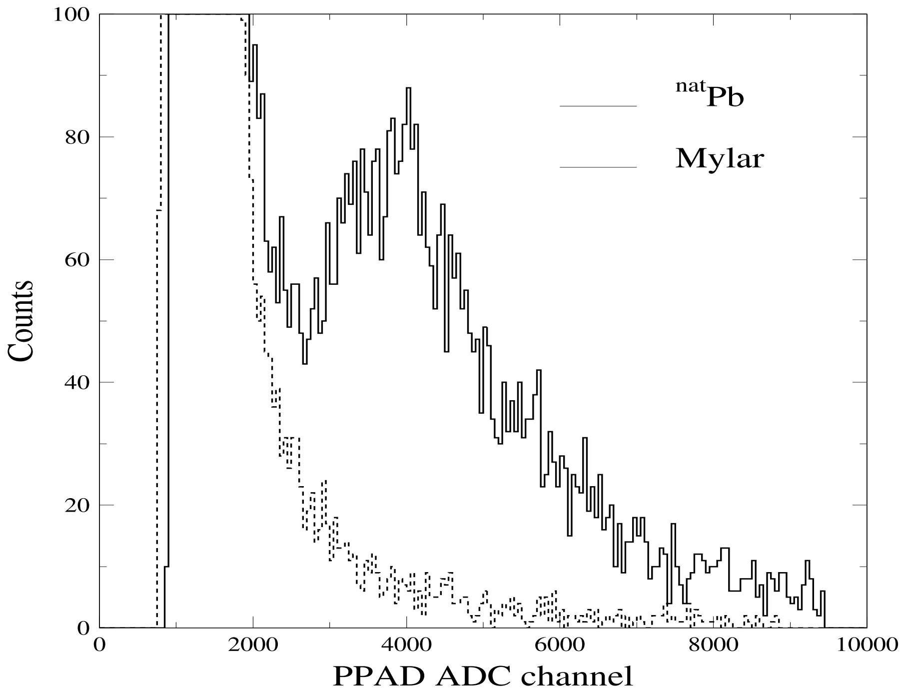

Figure 6.3: ADC spectra for ^{nat}Pb and Mylar.

The coincidence peak in the TDC spectrum therefore includes, besides fission events, both Pb(γ, α) events and events coming from the Mylar backing. Here, the reaction yield is determined from the PPAD ADC spectra, while the TDC spectra were used only to evaluate the contribution from the random background. The main assumption was that the shape of the α spectrum is the same as that for the Mylar. This is plausible, since the main contribution from the Mylar is the (γ, α) yield from the ^{12}C and ^{16}O in Mylar.

In order to compare the ADC spectra of each Pb target with that of the Mylar, and also to combine the data from all seven Pb targets, we need to know the pedestals and the gains of the ADCs recording the pulse-height distributions of the PPADs, but unfortunately these data were not recorded. In this situation, we adopted a compromise solution. We chose a region of the α-particle distribution, far enough from the fission peak so that we could assume that no fission events would be in that part of the distribution. Using this region, we shifted the ADC spectra from the seven lead targets to match the Mylar spectrum both in height and slope.

We then determined, for each lead target, the scaling factor representing the ratio of random events in the TDC coincidence peak and in a given region outside the peak. For this, data from all 61 T-channels were used. The background was fitted as described in Sec. 4.3, the fit was interpolated in the region of the coincidence peak, and finally the ratio of the areas under the fit function for regions B and C shown in Fig. 6.4 was taken, so that $S = B_{fit} \,/\, C_{fit}$.

Next, for each lead target and for Mylar, and for each T-channel, we found the ADC spectra corresponding to the two TDC regions: the coincidence peak including randoms (regions A+B in Fig. 6.4), and the randoms under the time coincidences (region B). The latter was obtained by scaling region C by the scaling factor S. We then subtracted the ADC spectra representing the contribution of random background (Fig. 6.5 (b)) from the ones representing the coincidence peak including randoms (Fig. 6.5 (a)). This was done for each T-channel, both for the combined data from the seven Pb targets and for Mylar. The resulting ADC spectra per T-channel represent the true time coincidences for lead (Fig. 6.5 (c)) and Mylar (Fig. 6.5 (d)). This last Mylar ADC spectrum (scaled by seven for the seven lead targets) was then subtracted from the combined lead spectrum. The fission-fragment yield per T-channel is then given by the events in the hatched area in Fig. 6.6, that is, events above ADC channel 2000. Also included in the yield are the events in the overflow channel of the ADC spectrum, not shown in Fig. 6.6. The statistical uncertainty corresponding to the lead yield per T-channel is calculated in Appendix B.

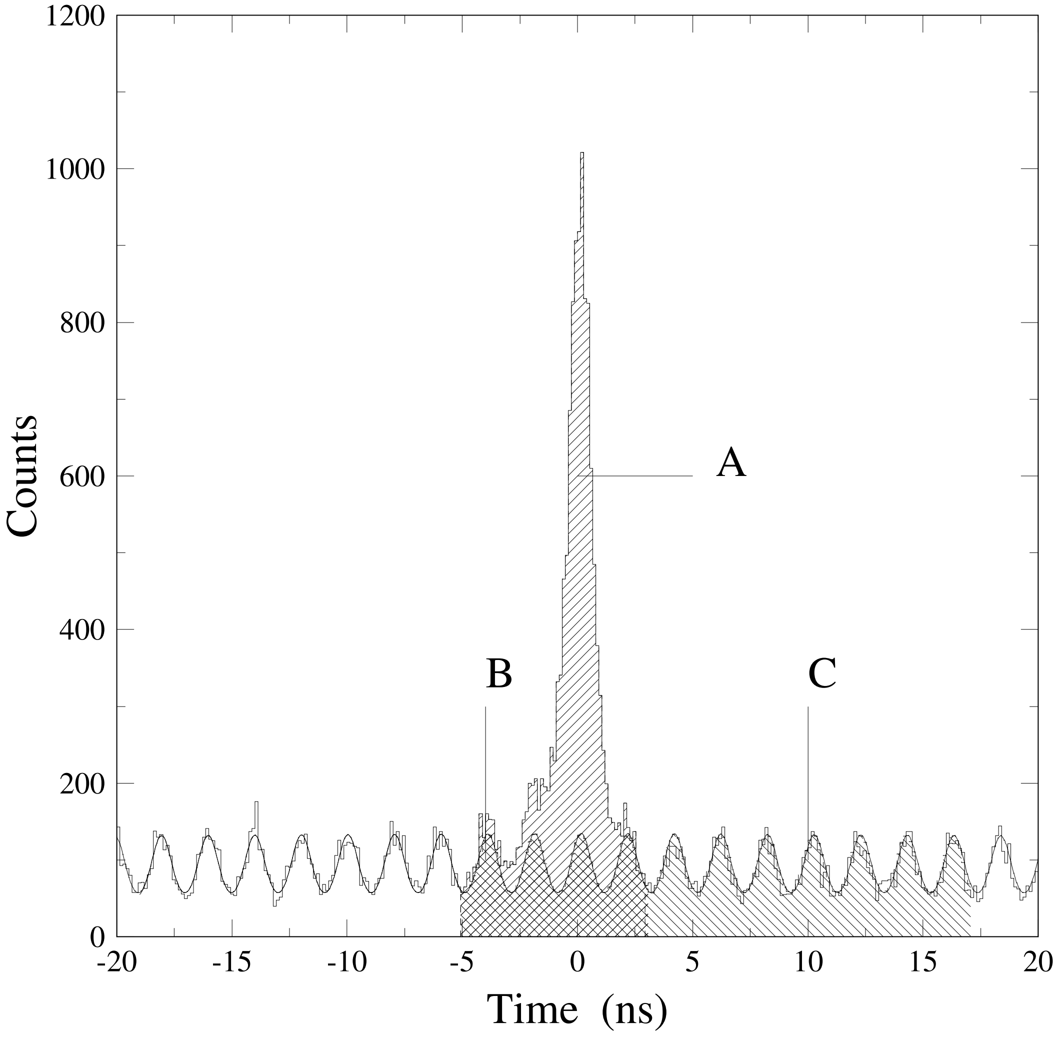

Figure 6.4: TDC spectrum for one of the Pb targets and all 61 T-channels. Region A defines the real fission-fragments, region B are the random events underneath the coincidence peak, and C is the region where the fit was done for the random background.

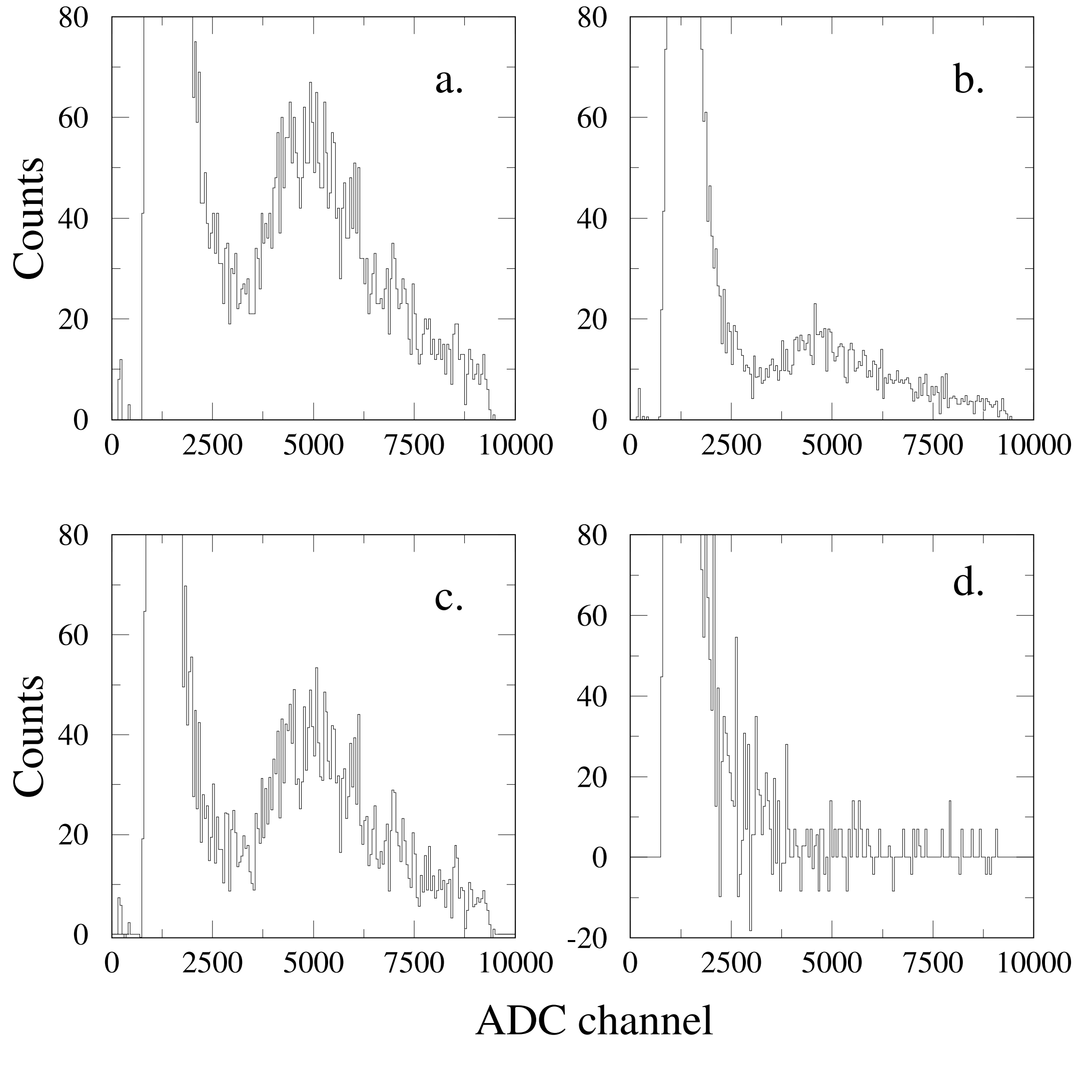

Figure 6.5: ADC spectra for: (a) Lead coincidence peak (regions A+B in Fig. 6.4); (b) Lead background under the coincidence peak (region B); (c) Lead coincidence peak after background subtraction, that is, spectrum (a) after subtracting spectrum (b) (region A); (d) Mylar, same as (c) for lead.

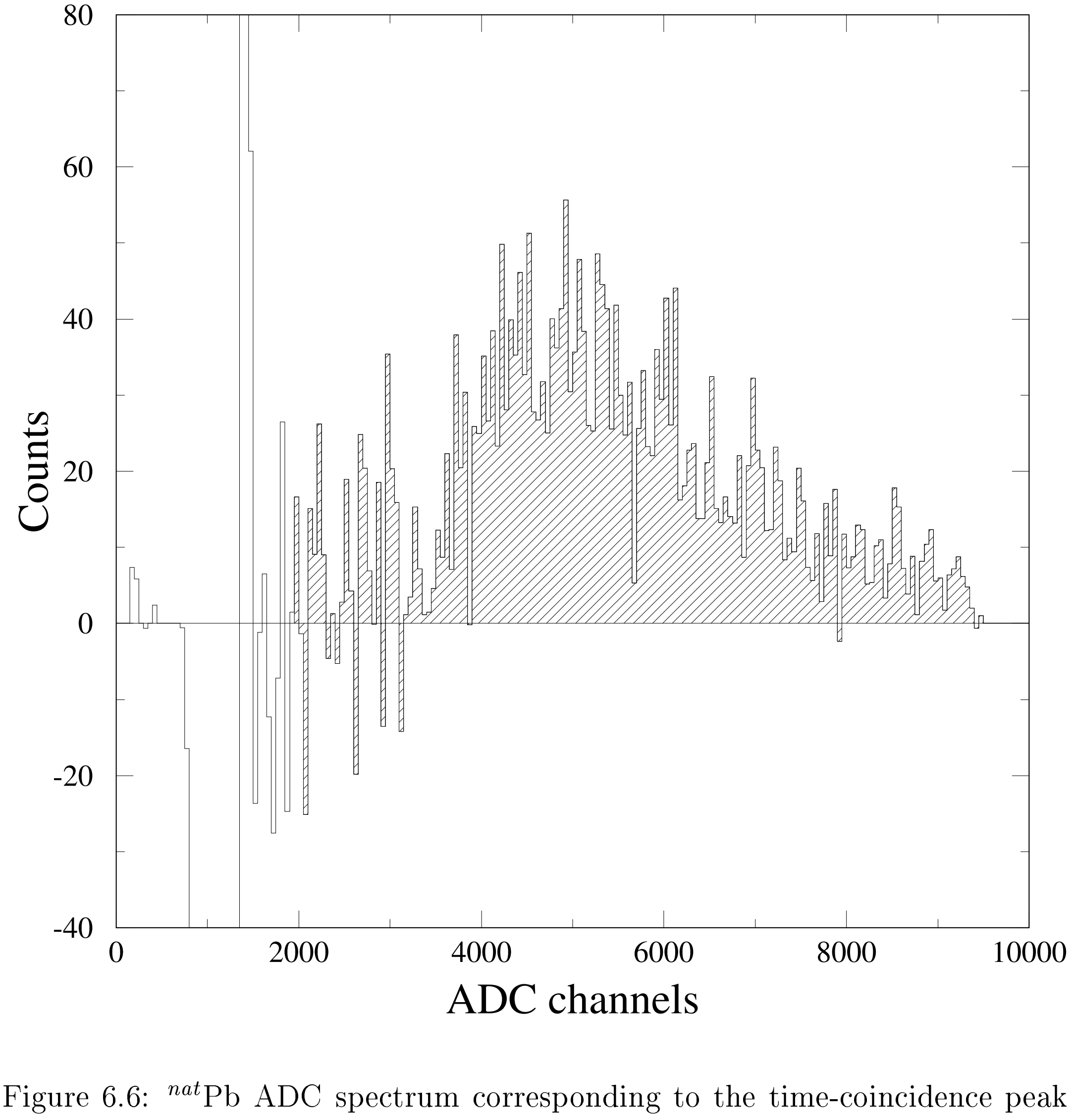

Figure 6.6: ^{nat}Pb ADC spectrum corresponding to the time-coincidence peak after subtraction of random background and of (γ, α) events and contributions from the Mylar substrate. This spectrum corresponds to T-counter 43 and E_0=1.7 GeV.

6.3 Various checks

This section includes the description of several consistency checks performed on the data. They include establishing the necessity for a dead-time correction, studying the level of beam-related background, checking the stability of the fission-fragment yield in time, proving that the cross-section results do not depend on applying the E-T correlation requirement, and checking the consistency of the fission cross section for the PPADs of the same isotope and the consistency in the photon-energy overlap regions for incident electron energies of 1.7 and 4 GeV.

6.3.1 Dead time

As mentioned earlier, an overall dead-time correction was not applied to the data because the experiment was run with the T-counter scalers inhibited in hardware by a "busy" signal from the data-acquisition readout electronics. If the dead-time effects are hardware corrected, then the number of events recorded for each run should be proportional to the number of scaler readings summed over the tagger focal plane. Because of the high background level present at low photon energies (high T-counter number), the scaler readings were integrated only up to the 47^{th} T-channel. Figure 6.7 shows this scaler sum versus the number of events recorded for each run for both $E_0 = 4\ GeV$ and $E_0 = 1.7\ GeV$. Both data sets show a linear correlation, although that trend is more apparent for the 1.7-GeV data, when the experimental conditions were much more stable.

6.3.2 Stability of yield in time

Figure 6.8 shows the time variation, over the two experimental run periods for 4 GeV and 1.7 GeV, of the average normalized yield per run. A weighted average was taken over the whole tagger focal plane and over all of the actinide fission targets. There are peak-to-peak variations within 12% and 9% of the mean for the 4-GeV and 1.7-GeV data, respectively.

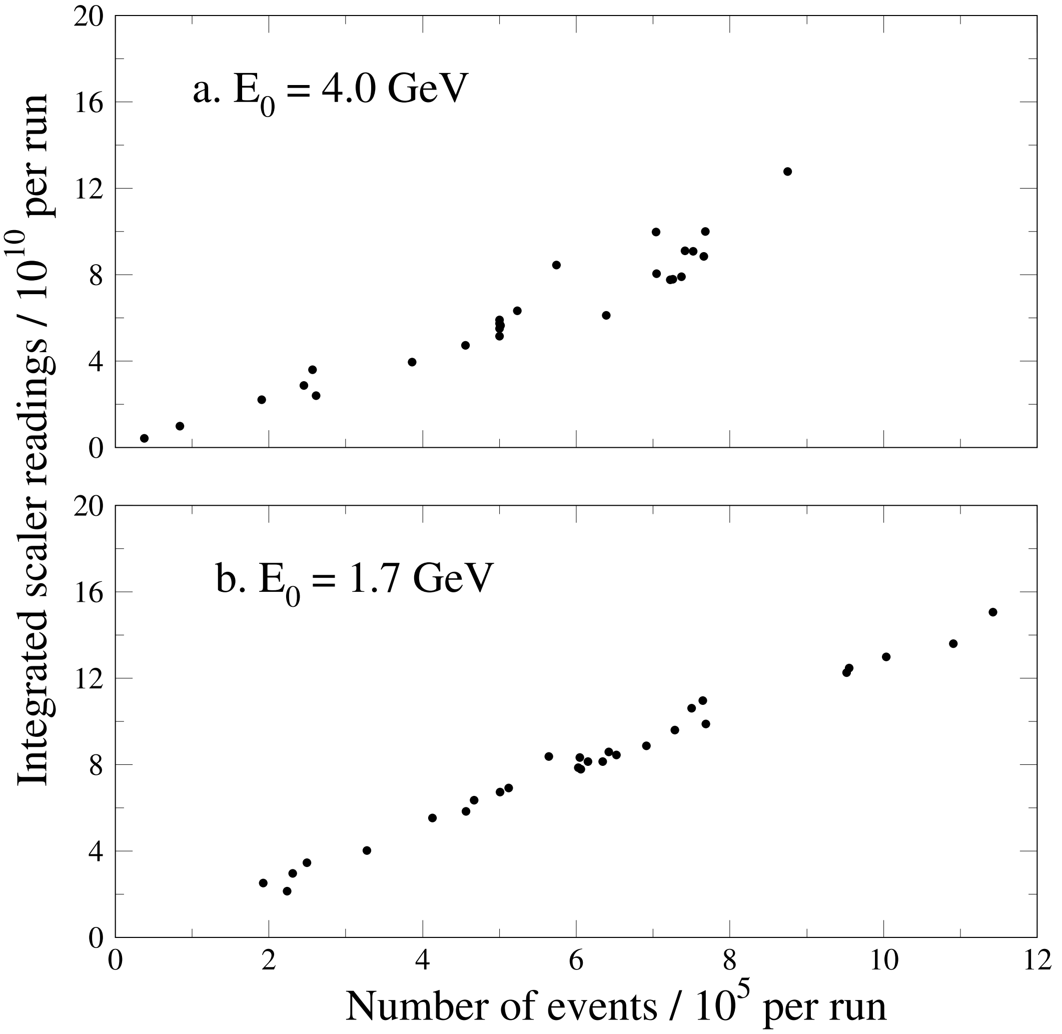

Figure 6.7: Integrated scaler readings versus recorded number of events for (a) E_0 = 4.0 GeV and (b) E_0 = 1.7 GeV.

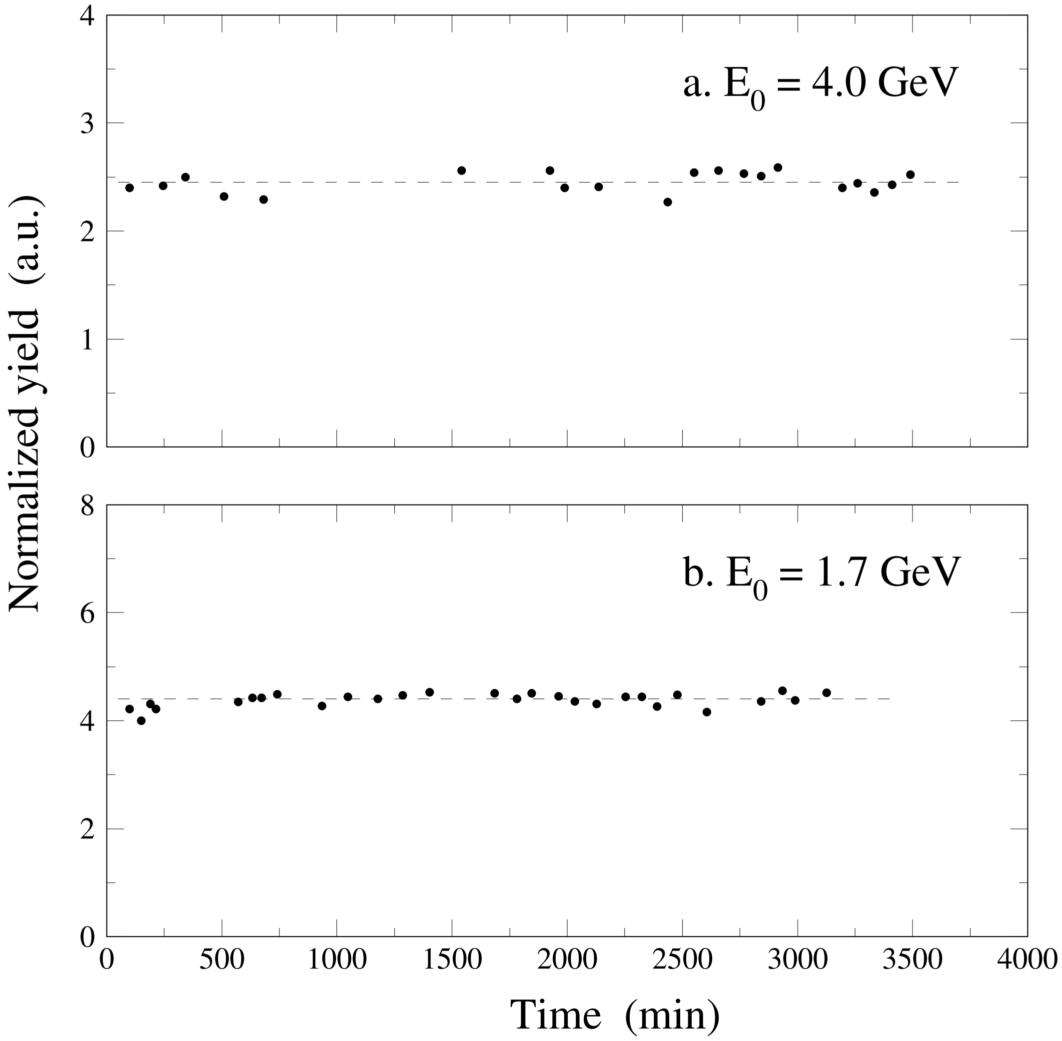

Figure 6.8: Time dependence of the average normalized yield per run for (a) E_0 = 4.0 GeV and (b) E_0 = 1.7 GeV. Statistical uncertainties are smaller than the symbol size.

6.3.3 Sample-out and radiator-out backgrounds

In order to check the sources and the levels of various kinds of backgrounds in the presence of beam during the experiment, runs under various conditions were recorded: Fission chamber IN / Radiator OUT; Fission chamber OUT / Radiator IN; and Fission chamber OUT / Radiator OUT. Additionally, runs with Beam OFF were also recorded. For the first two types of runs and for the Beam-OFF run, the ADC spectra for a PPAD with a ^{233}U target (having the highest alpha radioactivity) are shown in Fig 6.9. For comparison, the spectra are overlayed on the ADC spectrum for the same PPAD but for a regular fission run, taken before the background runs. All spectra were normalized to the duration of this data run. The background runs result in similar yields as the Beam-OFF run, when only natural radioactivity is present. This proves that the levels of beam-related backgrounds are negligible. The last plot in Fig 6.9 is the time spectrum for the Radiator IN / Chamber OUT run. The flat distribution shows that a coincidence peak is *not* present when the reaction chamber is *not* in the beam line, even with the radiator in its regular place.

6.3.4 E-T versus T-only results

The aim of requiring the E-T geometrical and time coincidence (see Sec. 4.2.4) was to correct for the beam-related background present at low photon energies. However, this cut should not affect the absolute value of the cross sections. In order to prove this statement, we calculated, for a given isotope, the ratios of the cross sections before and after requiring the E-T coincidence for $E_0 = 4\ GeV$ and $E_0 = 1.7\ GeV$. The results are presented in Fig. 6.10; they are consistent with unity in the regions where the high-T-counter background is not observed.

6.3.5 Consistency per isotope

For each target-detector combination and for each incident electron energy, we obtained an average cross section by combining the data from all 61 T-channels. The results are presented in Table 6.3, together with the ratios of the individual cross sec-

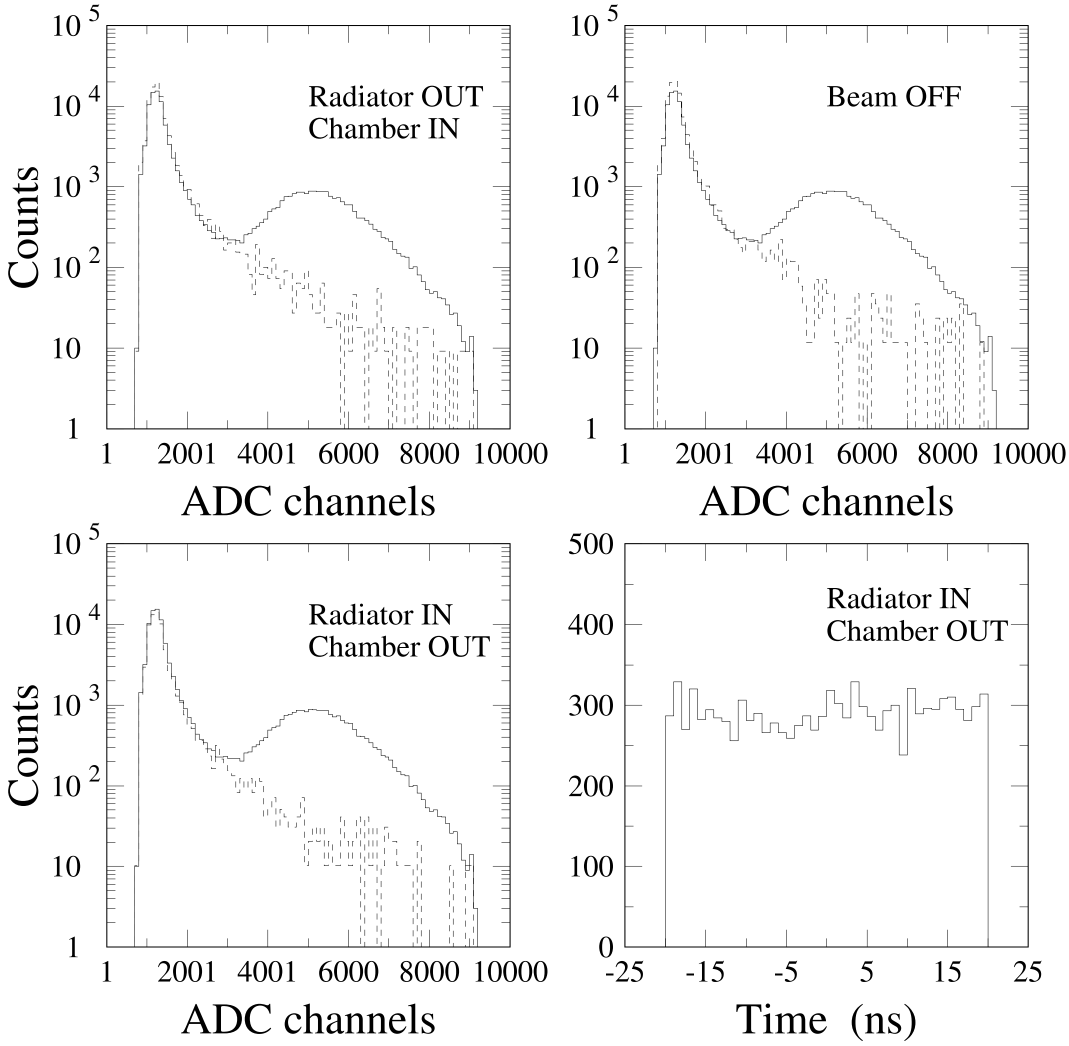

Figure 6.9: ADC spectra for a PPAD with a ^{233}U target for three types of background runs (dashed) compared with the same PPAD ADC spectrum for a regular fission run (solid). All background runs are normalized to the data run. The last plot is the time spectrum for the Radiator IN / Chamber OUT run, showing that a coincidence peak is *not* present.

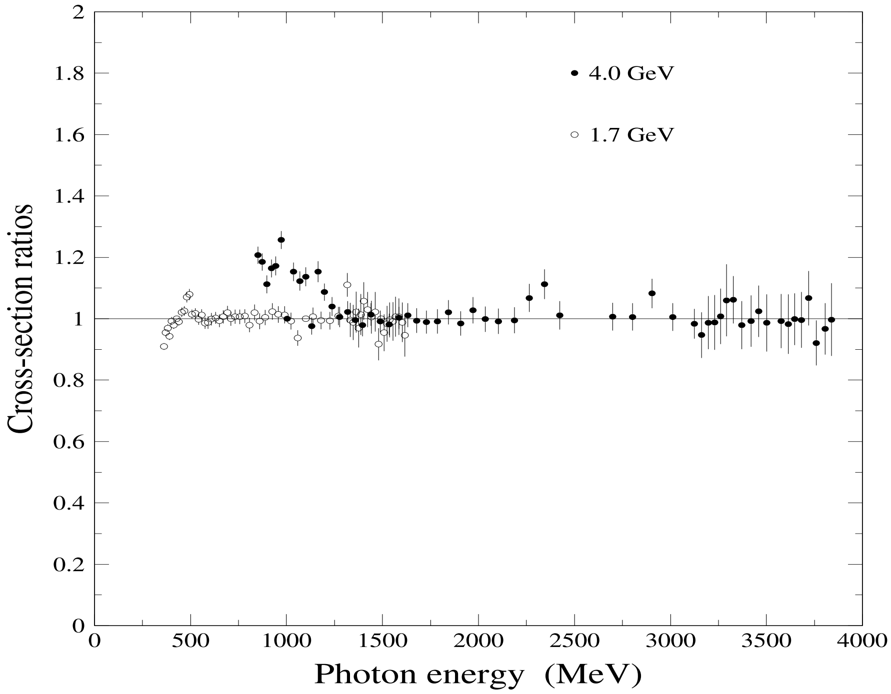

Figure 6.10: Ratios of cross sections without and with the E-T requirement for ^{238}U.

tions to the weighted average per isotope. For the actinide isotopes the ratios to averages are approximately the same for the two incident beam energies, implying that the differences within one isotope are most probably due to target-thickness variations. Among the actinides, the highest variations ($\approx 5-19$ %) are exhibited by ^{232}Th, while the lowest ones ($\approx 1-5$ %) by ^{238}U. If we consider all of these data for the actinides to be a set of 12 data points and assume that the deviations from the mean value are random, we get RMS values of $\sigma = 0.082$ and $\sigma = 0.076$ for the $E_0 = 4.0\ GeV$ and $E_0 = 1.7\ GeV$ data sets, respectively. And since for each actinide we had three targets, the deviation per actinide isotope will be $\sigma = 0.082/\sqrt{(3)} = 0.047$ at 4 GeV and $\sigma = 0.076/\sqrt{(3)} = 0.044$ at 1.7 GeV. For ^{nat}Pb, these values are $\sigma = 0.032$ and $\sigma = 0.029$, respectively.

	$\sigma_{\gamma F}/A$ (μb)		Ratio to average	
Isotope	4.0 GeV	1.7 GeV	4.0 GeV	1.7 GeV
^{237}Np	126.49 ± 1.07	213.88 ± 1.06	1.052	1.036
	131.02 ± 1.05	221.51 ± 1.05	1.090	1.073
	103.26 ± 1.05	184.26 ± 1.04	0.859	0.893
^{235}U	108.53 ± 1.06	195.09 ± 1.07	1.042	1.049
	107.29 ± 1.06	187.63 ± 1.03	1.030	1.009
	98.23 ± 0.93	177.58 ± 0.94	0.943	0.954
^{238}U	99.63 ± 0.71	179.83 ± 0.71	1.009	1.021
	102.01 ± 0.68	180.71 ± 0.68	1.033	1.026
	93.38 ± 0.77	166.24 ± 0.77	0.946	0.927
^{232}Th	62.58 ± 0.56	115.74 ± 0.58	1.049	1.089
	71.23 ± 0.60	125.61 ± 0.61	1.194	1.182
	55.89 ± 0.30	98.59 ± 0.31	0.937	0.937
^{nat}Pb	6.75 ± 0.07	10.25 ± 0.07	1.009	0.962
	6.61 ± 0.07	10.34 ± 0.07	0.988	0.970
	6.62 ± 0.07	11.05 ± 0.07	0.989	1.037
	7.02 ± 0.07	11.01 ± 0.07	1.050	1.033
	6.56 ± 0.07	10.55 ± 0.07	0.980	0.989
	6.37 ± 0.07	10.53 ± 0.07	0.953	0.988
	6.95 ± 0.07	10.94 ± 0.07	1.039	1.027

Table 6.3: Mean cross sections per target-detector combination and their ratios to their average for different beam energies.

6.3.6 Consistency in the overlap energy regions

The overlap energy region between the 4.0- and the 1.7-GeV data extends from 850 MeV to 1.6 GeV. Of course, the absolute cross sections obtained with the two beam energies must agree in the overlap region. Figure 6.11 shows the photofission cross sections obtained at E_0=4.0 GeV and E_0=1.7 GeV. For each of the six nuclei, the agreement between the two sets of data is excellent. For all of our target nuclei this agreement is expressed quantitatively in Table 6.4 by the average cross sections per nucleon in the overlap region.

	$\sigma_{\gamma F}/A$ (μb) [0.85-1.6 GeV]		
Isotope	4.0 GeV	1.7 GeV	Ratio
^{237}Np	148.01	150.63	0.983
^{233}U	131.83	134.49	0.980
^{235}U	125.14	126.22	0.991
^{238}U	120.81	122.13	0.989
^{232}Th	71.41	71.32	1.001
^{nat}Pb	10.84	10.47	1.035

Table 6.4: Photofission cross section per nucleon per target nucleus averaged in the overlap region of the 4.0- and 1.7-GeV data, and their ratios.

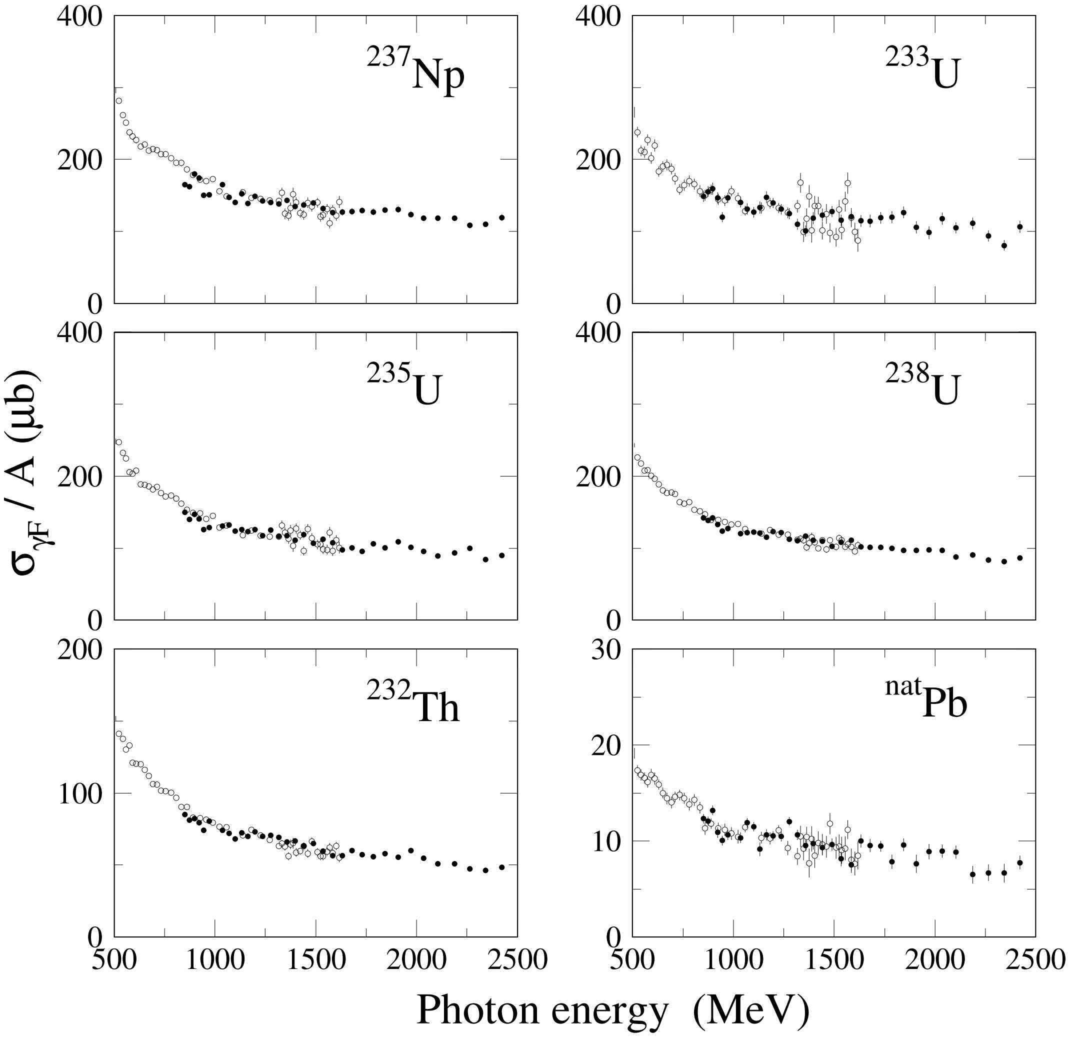

Figure 6.11: Photofission cross sections per nucleon, showing the overlap region between data at (•) $E_0 = 4.0\,GeV$ and (◦) $E_0 = 1.7\,GeV$.

6.4 Statistical and systematic uncertainties

The uncertainty in the total photofission cross section $\delta\sigma$ is the combined uncertainty from statistical and systematic uncertainties.

The *statistical uncertainty* $\delta\sigma^{sta}$ in the cross section is dictated by the statistical uncertainty δY_{FF} in the fission-fragment yield

$$\delta\sigma^{sta} \propto \delta Y_{FF} \, .$$

For the actinides, δY_{FF} was calculated as described in Sect. 4.3. The statistical uncertainty for lead is derived in Appendix B.

The *systematic uncertainty* $\delta\sigma^{sys}$ in the cross section is the combined effect of uncertainties in determining the fission-fragment yield, the tagged-photon flux, the PPAD geometrical acceptance, and the target thickness. The latter gives the highest contribution, which is about 5%. The uncertainty in determining the fission-fragment yield is in turn due to uncertainties introduced by the cuts used as event-selection criteria. A discussion of each of the possible sources of error mentioned above follows.

• *Choice of the ADC threshold.* This affects the difference between the alpha counts included in the fission yield and the fission counts excluded from the fission yield. This difference was evaluated to be less than 1% of the total yield.

• *Left-right cut.* To check this effect, we evaluated the ratio between the counts with both L and R and with either L or R. We then compared these distributions for data runs with the similar distributions for normalization runs. The agreement is within 1% for T-channels below 48. For the higher T-channels, the differences are bigger, but this can be attributed not to the L-R cut, but to the extra background present in this region of the focal plane.

• *E - T matching.* The fraction of events excluded by requiring a geometric and timing correspondence between E- and T-counters is not negligible. However, the fraction of counts excluded by this cut from the fission yield is the same as that excluded from the photon flux used for normalization. Thus, the overall error is insignificant.

•*Photon flux determination.* The tagging efficiency was calculated as an average, using all of the available data, as mentioned in Sect. 5.2.2. The differences between individual runs give an estimate of the systematic uncertainty associated with the tagging efficiency. These differences, averaged over the tagger focal plane, are listed in Table 6.5 for the two beam energies.

•*PPAD geometric acceptance.* The detector acceptance was calculated numerically. The positions of various detectors in the chamber, as well as small variations in relative positions within the target-detector assembly, result in acceptance differences smaller than 1%.

•*Target thickness.* The actinide target thicknesses were measured to an accuracy of about 3%, the exact values being listed in Table 6.2. For the lead foil, the manufacturer gave an uncertainty of 10%. However, the results presented in Table 6.3 for the average cross sections per detector, show larger than 3% variations for the actinides and smaller than 10% variations for lead. As described in Sect. 6.3.5, the values to be attributed as systematic uncertainties due to target thickness are summarized in Table 6.5.

$\delta\sigma^{sys}$	4.0 GeV		1.7 GeV	
Tagging efficiency	$\sim 4\%$		$\sim 2\%$	
	Actinides	Lead	Actinides	Lead
Target thickness	4.7%	3.2%	4.4%	2.9%
Total	6.2%	5.1%	4.8%	3.5%

Table 6.5: Systematic uncertainties due to tagging efficiency, target thickness, and the combined uncertainties for the actinide and lead targets, for the 4-GeV and 1.7-GeV data.

Chapter 7

Results and Interpretation

7.1 Photofission cross sections

7.1.1 Absolute cross sections

Photofission data have been collected for photon energies from 0.17 to 3.84 GeV, using three incident electron energies. The good agreement in the overlap region between the two energy bites was presented in Sect. 6.3.6. The difference between the 4.0- and the 1.7-GeV actinide data in the overlap region is 2% or less, proving good absolute normalization for the two data sets. Data in the overlap regions for two incident electron energies were combined by taking a weighted average. Data were then rebinned in equal-energy bins according to Table 7.1. The bin sizes were chosen taking into account both the shape of the cross section as a function of incident photon energy and the size of the statistical uncertainties. Thus, in the region of the Δ resonance, where the cross section varies rapidly with energy, the bins are narrow (20 MeV). Above 1 GeV, the cross section is almost energy independent, so the bins are wider (150 MeV). Also, more narrow bins in this energy region would have resulted in higher statistical uncertainties than the present 4% (for all of the actinides, except ^{233}U).

Figure 7.1 shows our results for the absolute photofission cross sections per nucleon $\sigma_{\gamma F}/A$ as a function of the incident photon energy for all six nuclei. The error bars reflect statistical uncertainties only. The tables containing the values for the photon

E_γ (GeV)	ΔE (MeV)
0.18-0.55	20
0.55-1.00	65
1.00-3.84	150

Table 7.1: Energy bins ΔE used when rebinning the data after combining data in the overlap regions.

energies, fission cross sections, and associated statistical uncertainties are presented in Tables C.1 and C.2 in Appendix C.

In Fig. 7.1, data for neptunium and the three uranium isotopes are shown with the same scale on the vertical axis. The photofission cross section per nucleon for ^{237}Np has the highest absolute value, significantly higher than that for ^{238}U. One can also notice small differences between the three uranium isotopes; the cross section per nucleon for ^{233}U is higher than that for ^{235}U, which in turn is higher than that for ^{238}U. The cross section for ^{232}Th is markedly lower than the other actinides, as expected from previous measurements [Arr95, San00b]. The cross section for ^{nat}Pb is about an order of magnitude lower than those for the actinides.

The energy dependence for all of these cross sections is similar. The Δ resonance is clearly seen, and has about the same position and width for each of the actinide isotopes. As expected from most previous data, the present photofission cross sections exhibit no prominent resonance structure above the Δ resonance, and they slowly decrease with increasing photon energy. There does appear to be weak structure for Np, ^{235}U, and Pb, and possibly ^{233}U, in the energy region between about 500 and 900 MeV.

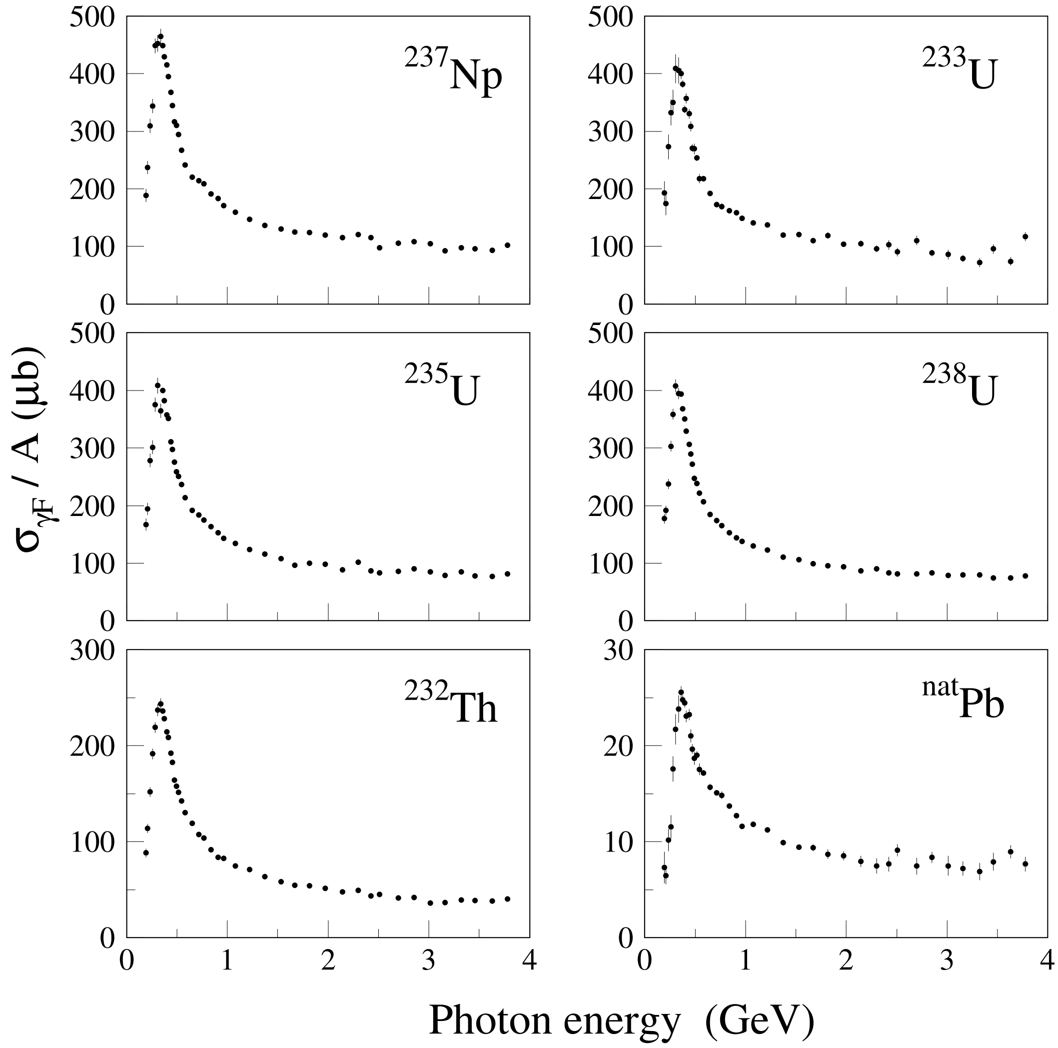

Figure 7.1: Absolute photofission cross sections per nucleon as a function of the incident photon energy.

7.1.2 Relative cross sections

Using the highest cross section as a reference, namely that for ^{237}Np, we show in Fig. 7.2 the photofission cross sections per nucleon relative to that for ^{237}Np, as a function of the incident photon energy. The tables containing the values for the photon energies, relative fission cross sections, and associated statistical uncertainties are presented in Tables D.1 and D.2 in Appendix D. One can see that the probability for ^{238}U to undergo fission is about 20% *smaller* than that for ^{237}Np. This confirms the previous low-energy measurements at Novosibirsk [Ilj92a] and SAL [San00b]. The other two uranium isotopes also have fissilities lower than ^{237}Np (about 85%, slightly higher for ^{233}U). Since all three uranium isotopes undergo fission with a lower probability than Np, we can conclude that our results contradict the assumption that any of these uranium isotopes has a photofissility of 100% over this entire energy range.

7.2 Comparison and interpretation

7.2.1 Comparison with previous photofission data

The previously existing photofission data for the six nuclei are summarized in Sect. 1.2.1. Figure 7.3 shows our data up to 1.2 GeV for ^{235}U, ^{238}U, and ^{232}Th, for which the previous photofission data extend up to 800 and 1200 MeV, respectively. The present data are in good agreement at low energies with the data from Refs. [Ilj92a, San00b]. Our ^{238}U data agree well with the average of the Mainz [Fro94] and the Frascati [Bia93b] data from the Δ-resonance region up to about 800 MeV. The agreement is not as good between our ^{232}Th data and the Frascati [Bia93a] data.

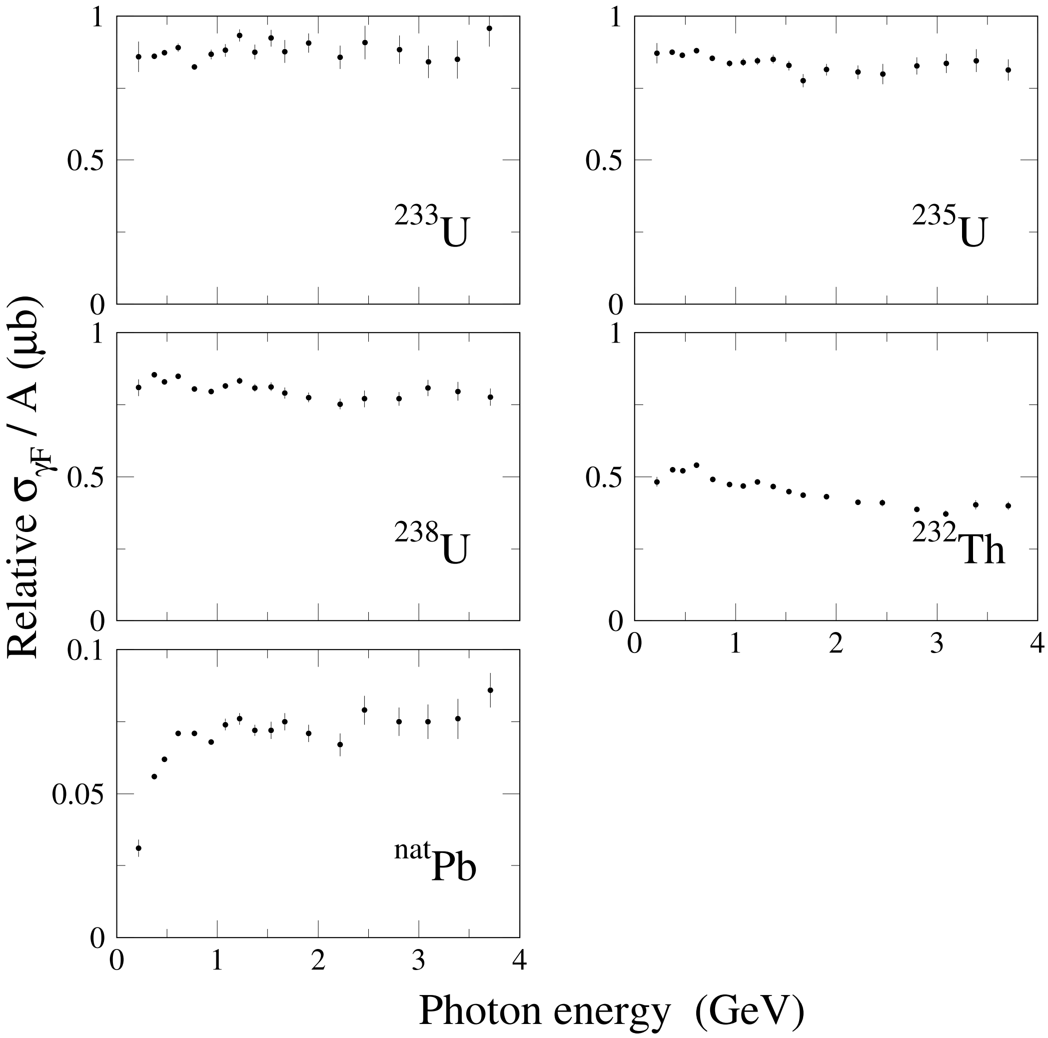

Figure 7.2: Photofission cross sections per nucleon relative to ^{237}Np as a function of the incident photon energy.

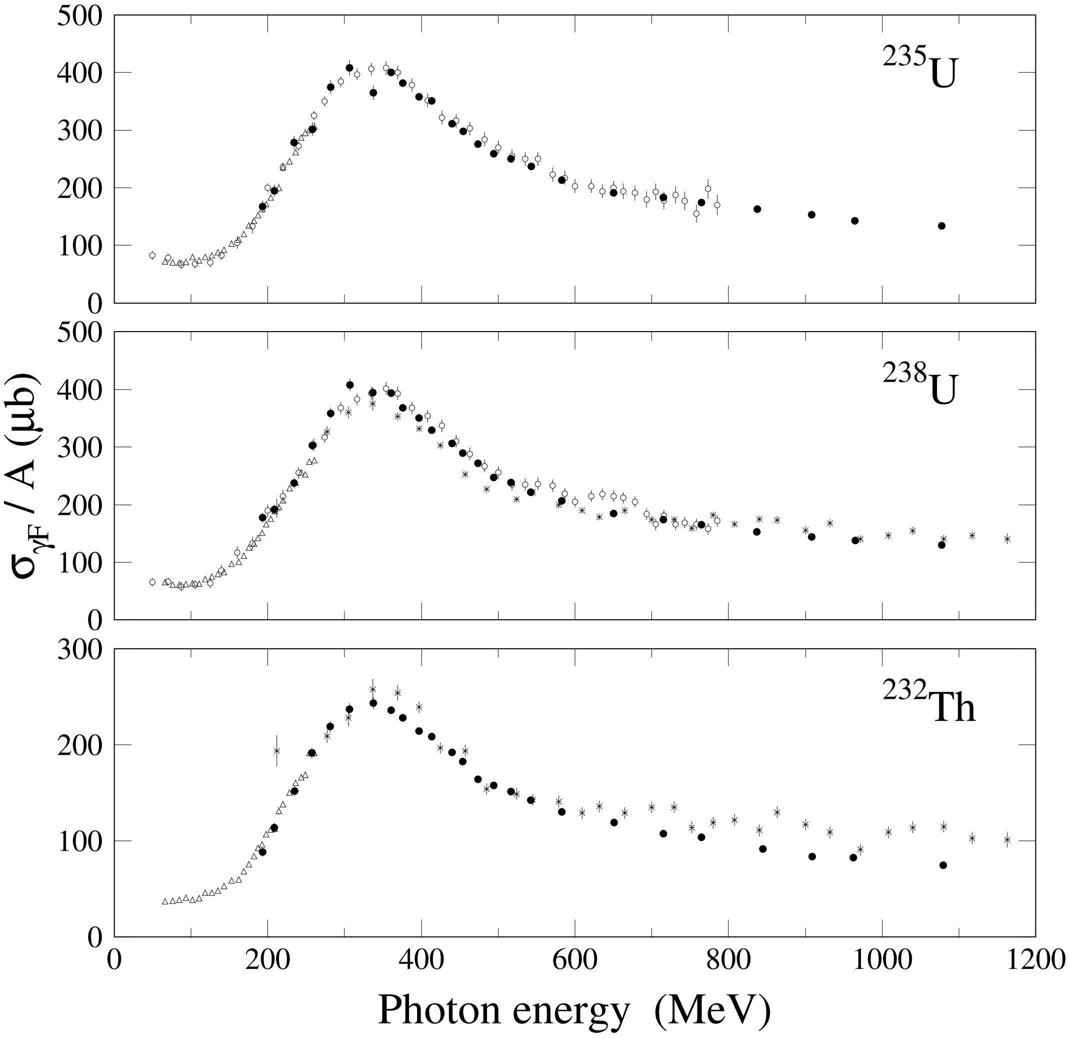

Figure 7.3: Comparison of our absolute photofission cross sections per nucleon for ^{235}U, ^{238}U, and ^{232}Th. with previous photofission data: ($\triangle$) [San00c], ($\circ$) [Fro94], ($*$) [Bia93a, Bia93b].

7.2.2 Comparison with previous photoabsorption data

Comparison with $^1H(\gamma, tot)$ data

In Fig. 7.4 we present our photofission data for ^{238}U together with the available photoabsorption data on the proton from [Arm72, Mac96]. A logarithmic scale for the abscissa allows for a better comparison at lower energies. In the region of the Δ resonance our measurements confirm the previous results in showing a broadening of the Δ peak inside the nuclear medium, compared with the case of the proton. As we saw in Sect. 1.2.2, this feature has been proven experimentally for many nuclei, and has been explained theoretically using the Δ-hole model [Car92]. The higher D_{13} and F_{15} resonances, clearly seen in the photoabsorption cross section for the proton (and

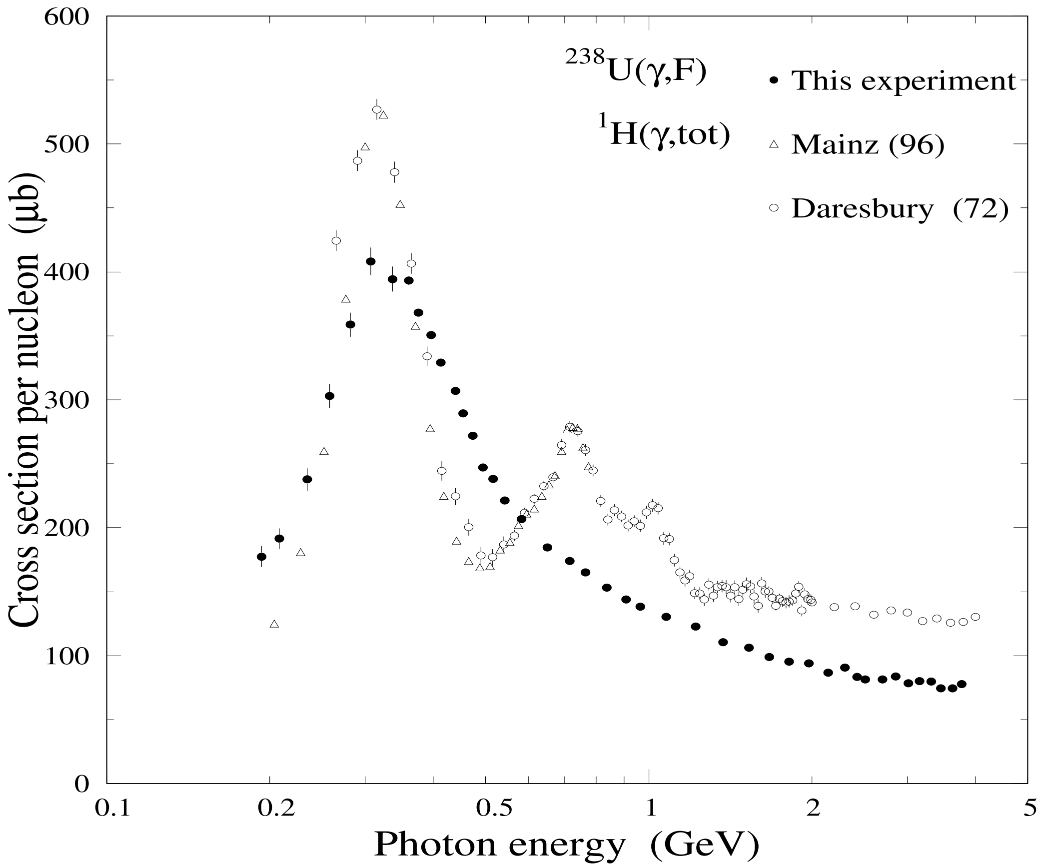

Figure 7.4: Comparison of our absolute photofission cross section per nucleon for ^{238}U with previous photoabsorption data on the proton ($\triangle$) [Mac96], ($\circ$) [Arm72].

for the deuteron), are not observed in our photofission cross sections, as expected from previous data.

Comparison with $A(\gamma, tot)$ data

The most recent photoabsorption data on C and Pb [Muc99] is shown in Fig. 7.5, together with our highest photofission cross section, which is the one for ^{237}Np. Above 1 GeV there is good agreement among these data sets. The first conclusion would then be that the photofission cross section for ^{237}Np exhausts the total photoabsorption cross section almost completely. This statement will be confirmed by results presented in following sections. Secondly, since there is not much variation in cross sections per

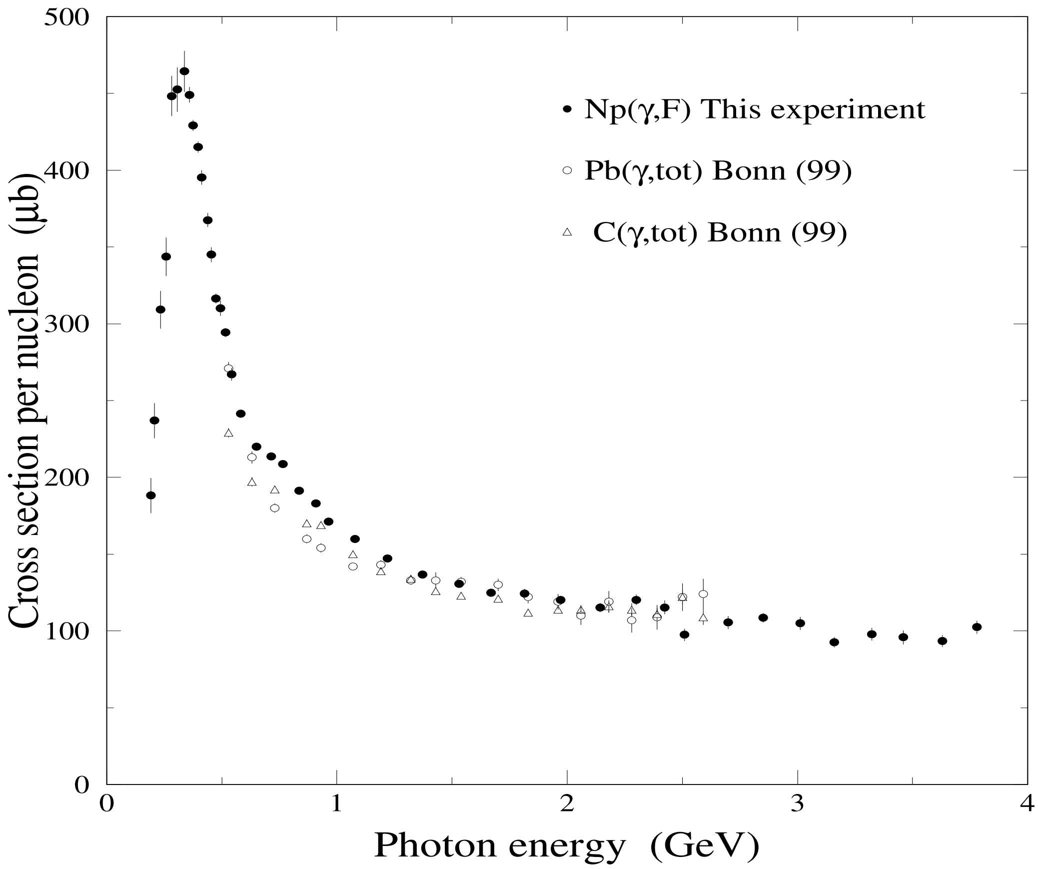

Figure 7.5: Photofission cross sections per nucleon for ^{237}Np compared with previous photoabsorption data [Muc99] for (○) Pb and (△) C.

nucleon from A=12 to A=237, we can infer that the concept of "universal behavior" is confirmed in general, if not in fine detail.

A more comprehensive comparison is attempted in Fig 7.6, in which we present the photofission data for ^{237}Np, ^{238}U, and ^{232}Th and the existing Pb photoabsorption data [Muc99, Cho83, Bia96, Bro73]. The photofission data include the present data as well as previous data from [Ilj92a, San00b, Fro94, Bia93b, Bia93a]. Both $\sigma_{\gamma F}$ and $\sigma_{\gamma A}$ data were fitted using a modified Breit-Wigner formula:

$$f(x) = a + \frac{bx^c}{(x-d)^2 + e}$$

where the values of the five fitting parameters are given in Table 7.2.

	a	b	c	d	e
^{237}Np	47.22	59.70	1.79	0.27	0.017
^{238}U	38.99	48.05	1.75	0.27	0.017
^{232}Th	4.74	46.87	1.78	0.26	0.022
Pb	58.17	48.46	1.83	0.28	0.016

Table 7.2: Fitting parameters for the presently existing photofission data (including the present one) for ^{237}Np, ^{238}U, and ^{232}Th, as well as for the photoabsorption data data for Pb.

The data used for the fit and the corresponding fitted functions for Pb are shown in Fig. 7.6 (a). The band widths in Fig. 7.6(b) represent the uncertainties in the fits. The energy scale is again logarithmic, for clarity at the lower energies. We note that the only low-energy data on Pb [Cho83] should be regarded as a lower limit since it includes only (γ, xn) cross sections, where $x \geq 2$, and hence does not include any of the (γ, n), (γ, p), (γ, α), (γ, pn), or $(\gamma, \alpha n)$ channels. One can see that $\sigma_{\gamma F}/A$ for ^{237}Np is a few percent higher than $\sigma_{\gamma A}/A$ for Pb only below the Δ peak, and is in very good agreement at higher energies, indicating again that $\sigma_{\gamma F} \simeq \sigma_{\gamma A}$ for ^{237}Np.

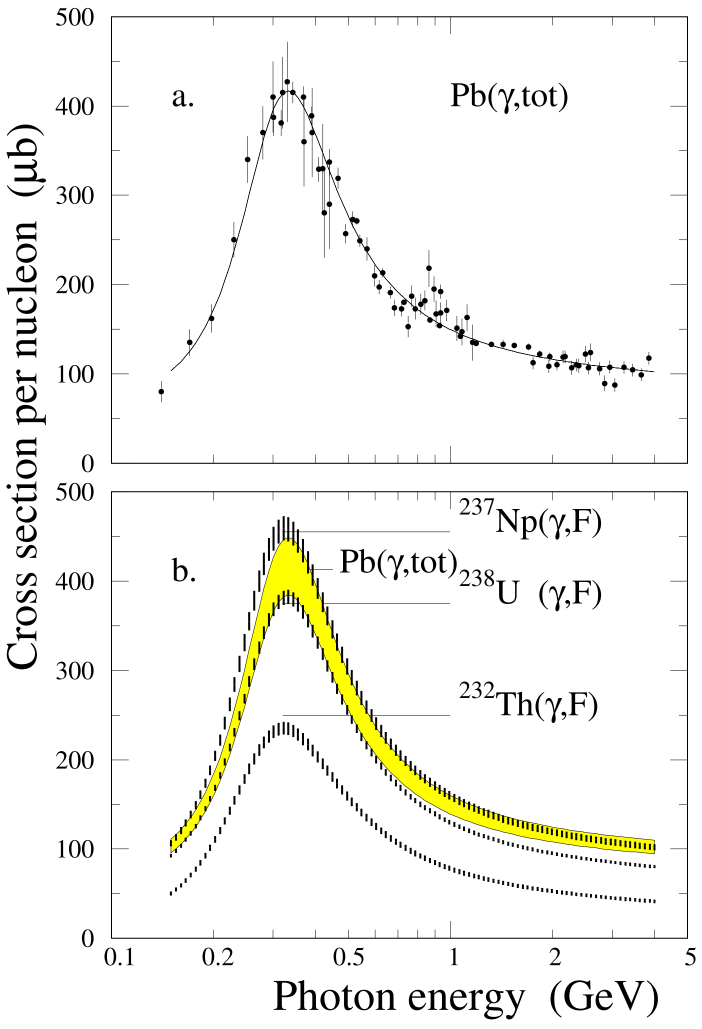

Figure 7.6: (a) Fit to the existing photoabsorption data on Pb. (b) Comparison of photofission cross sections per nucleon for ^{237}Np, ^{238}U, and ^{232}Th (bar bands) with previous photoabsorption data on Pb (gray band). The bands represent fits to the existing data (see text).

7.2.3 Energy dependence of the relative cross sections

For the actinide isotopes and for Pb above 1 GeV, the energy dependence of the relative cross sections appears to be almost flat (see Fig. 7.2). ^{232}Th, which fissions with about half the probability of ^{237}Np, seems to have a fissility slowly decreasing with energy. For ^{nat}Pb the fissility relative to ^{237}Np increases rapidly below 1 GeV, then seems to be slowly reaching an asymptotic value of ~ 0.75 towards 4 GeV.

For a given nucleus, the photofission probability after is mainly reflecting, according to Eqn. 2.9, the change of the excitation energy E^* with respect to the incident photon energy E_γ. Thus, an energy-independent photofissility indicates that E^* is proportional to E_γ.

The almost constant energy dependence of the relative photofission cross sections suggests that a common mechanism is responsible for the photofission process. This suggests in turn that the two-step cascade-evaporation model described in Sect. 2.1 and used to explain the fission process at intermediate energies (up to about 1 GeV) is also valid in the 1-4 GeV region.

7.2.4 $\mathbf{Z^2/A}$ dependence of the relative cross sections

Using the liquid-drop model, Bohr and Wheeler [Boh39b] have defined a *fissility parameter* as half of the ratio the Coulomb energy $E_c(0)$ and the surface energy $E_s(0)$ of the undeformed nucleus of radius R_0

$$x = \frac{E_c(0)}{2\ E_s(0)} \sim \frac{Z^2/R_0}{R_0^2}$$

By fitting experimental nuclear masses and yields, this parameter can be expressed as

$$x \simeq \frac{1}{50}\,\frac{Z^2}{A}$$

According to the liquid-drop model, the parameter x serves as a rough indicator of the ability of a nucleus to fission spontaneously. Better estimates have to account for quantum mechanical barrier penetration and for the permanent equilibrium deformation of nuclei in the region around uranium. In the following discussion we will call the fissility parameter only the ratio Z^2/A.

Figure 7.7 depicts these relative cross sections as a function of the fissility parameter Z^2/A. The vertical bars represent the range spanned by the relative cross sections over the energy range of the present experiment. The Z^2/A values seem to follow a monotonically increasing curve. If this curve approaches an asymptotic value of 1.0, we can deduce that the fission probability approaches unity. This means that for ^{237}Np the fission probability, while perhaps not reaching unity, probably is close to it.

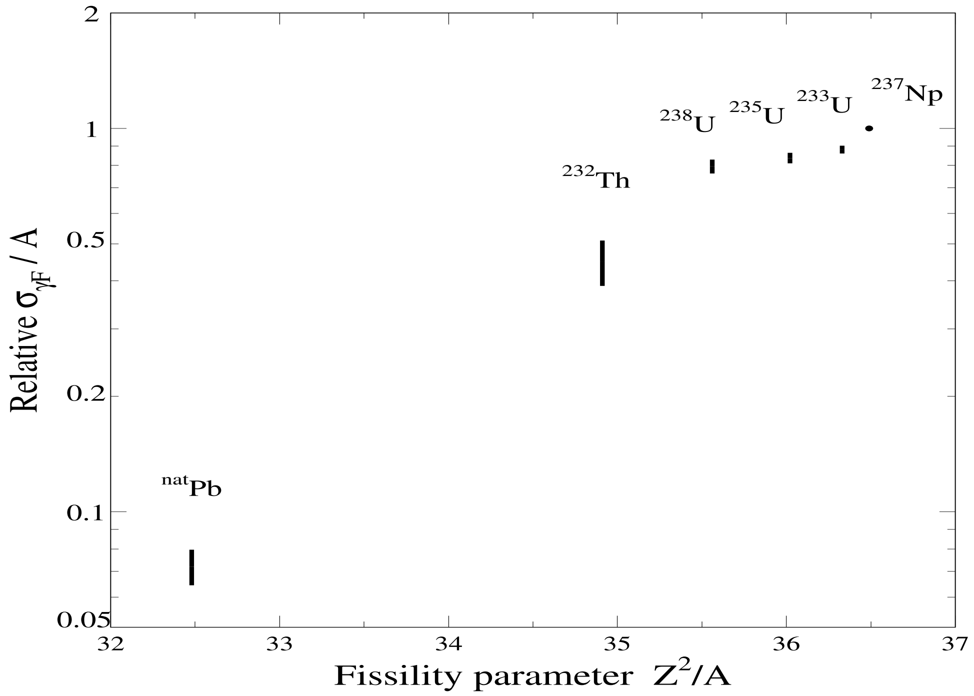

Figure 7.7: Photofission cross sections per nucleon relative to ^{237}Np as a function of the fissility parameter Z^2/A.

7.2.5 Shadowing

Figure 7.8 shows the ratios of the photofission cross sections for ^{237}Np, ^{238}U, and ^{232}Th and the corresponding cross sections for the sum of the protons and neutrons [Arm72] in each of these nuclei. The photon absorption cross section for the neutron was deduced from those for proton and deuteron. Two data points [Mic77] for the photoabsorption cross section for ^{238}U are shown for comparison.

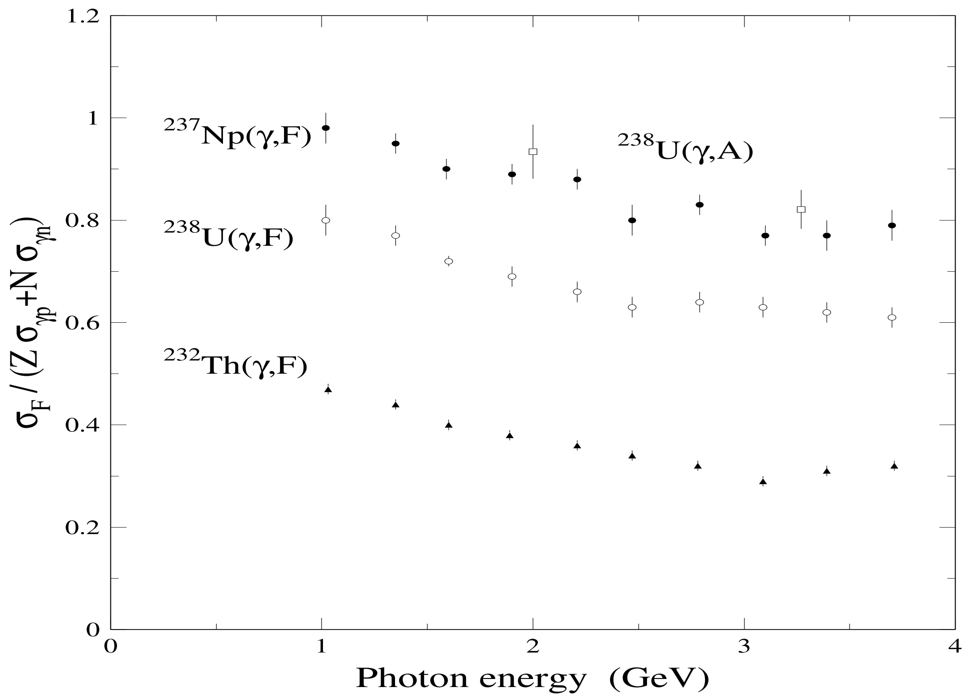

Figure 7.8: Ratio of the photofission cross sections for ^{237}Np, ^{238}U, and ^{232}Th and the corresponding total cross sections for the sum of the protons and neutrons [Arm72] in each of these nuclei. Two data points (open squares) [Mic77] for the total photoabsorption cross section for ^{238}U are shown for comparison.

We have seen that $\sigma_{\gamma F}$ is smaller than $\sigma_{\gamma A}$ for the three uranium isotopes, for Th, and for Pb. Thus, we cannot use the photofission cross section to measure the shadowing effect, except perhaps for the case of ^{237}Np (if we assume that its photofission probability is equal to unity, as suggested by Figs. 7.5 and 7.6). If we make this assumption, we observe the onset of shadowing below 1.5 GeV, such that

A_{eff}/A decreases to less than 80% at 3.5 GeV, as shown in Fig. 7.8. It is also clear that $\sigma_{\gamma F}$ for ^{238}U is much less than $\sigma_{\gamma A}$, while $\sigma_{\gamma F}$ for ^{237}Np is not. This trend supports the hypothesis that the fission probability for ^{237}Np is close to 100%, and is quite consistent with the relative fission cross sections of Fig. 7.7, which appear to be approaching an asymptote near the Z^2/A value of ^{237}Np.

An estimate of the shadowing for the other five nuclei besides ^{237}Np can be obtained if we estimate their total absorption cross sections. If, again, we assume that the fissility W_F of ^{237}Np is close to unity, then the fissilities for the other nuclei are given by their fission cross sections relative to that of ^{237}Np (see Eqn. 1.2). The averages of the fissilities over the entire energy range were calculated, and then the photoabsorption cross sections were estimated by the ratios of the photofission cross sections and the corresponding average fissilities. A_{eff} was then calculated, and the results are presented in Fig. 7.9. Except for ^{232}Th, the other five nuclei show a very similar behavior, with $\mathrm{A}_{eff}/\mathrm{A}$ values of approximately 0.8 at 4 GeV, while for ^{232}Th this value is only about 0.65.

One attempt to explain the different behavior of thorium as compared to the other heavier actinides was based on the possibility that ^{232}Th would be more transparent than the uranium isotopes [Arr95]. The difference in nuclear transparency, *i.e.* in the mean free path of nucleons inside the nucleus, can be due in turn to a difference in the imaginary part of the optical potential, though there is no explanation yet for which aspect of the nuclear structure might dictate this difference. Another approach is to describe the compound nucleus formation process by taking into account the clustering aspects of the nucleus, with the pre-formed clusters interfering in the intranuclear cascade process [Dep96]. The difference between Th and U would then be explained by their different cluster pre-formation probabilities.

Some of the results presented here are published in a Physical Review Letters paper [Cet00], while a more detailed paper will be sent for publication in Physical Review C.

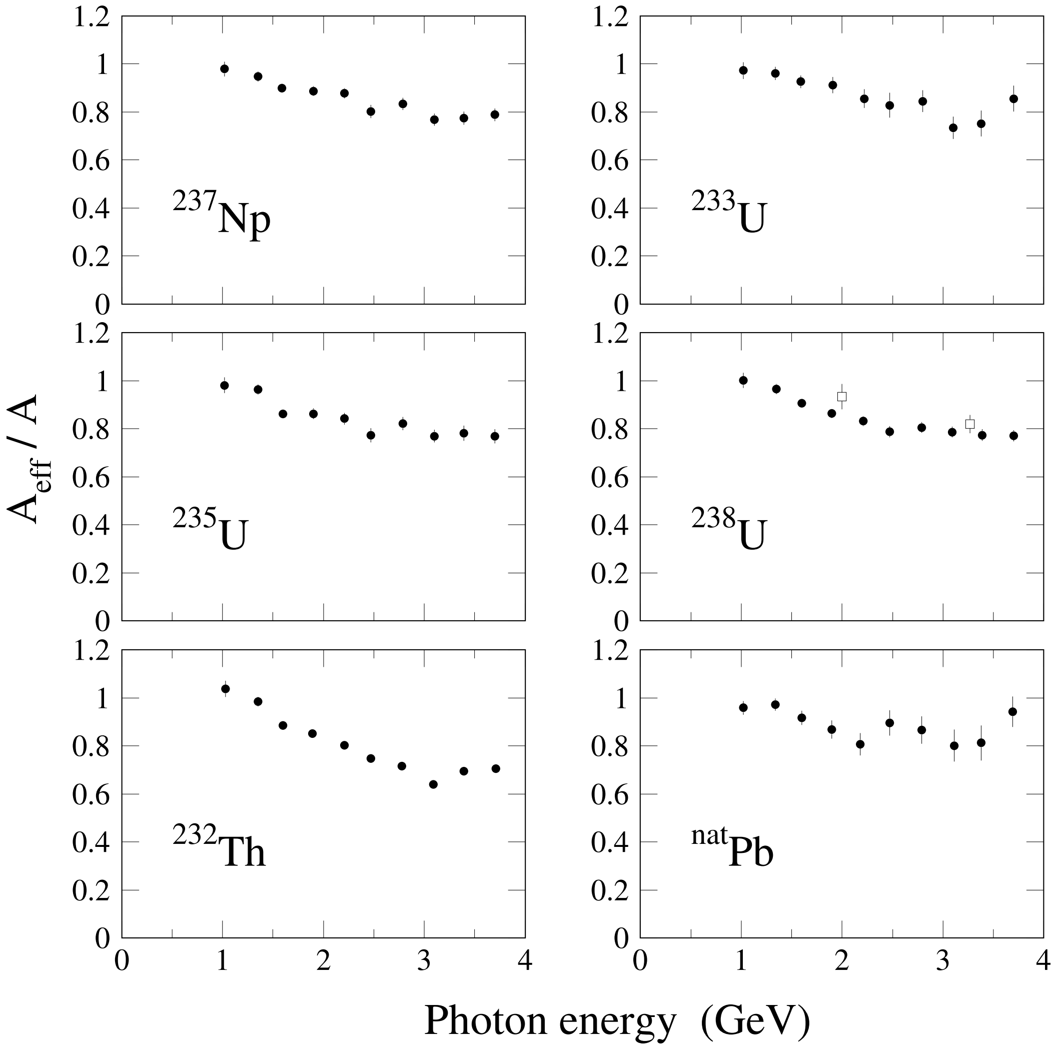

Figure 7.9: Estimate of the effective number of nucleons seen by the incident photon for the six nuclei studied (see text for details). The open squares for ^{238}U are data of [Mic77].

Chapter 8

Summary and Outlook

In summary, we have performed *simultaneous* measurements of the total photofission cross sections $\sigma_{\gamma F}$ for five actinide nuclei (^{237}Np, ^{233}U, ^{235}U, ^{238}U, and ^{232}Th), and for one preactinide nucleus (^{nat}Pb). The tagged-photon beam was produced by the photon-tagging spectrometer in Hall B at Jefferson Lab, and the photon energy range of this experiment was from 0.17 to 3.84 GeV. Our results have a statistical uncertainty of $\sim 3\%$ (varying from 1 to 6% across the energy range), and a systematic uncertainty of $3.5 - 6.2\%$ (depending on nucleus and energy).

8.1 Conclusions

Absolute photofission cross sections per nucleon

There are a few conclusions that can be drawn from our results for the absolute photofission cross sections per nucleon and from their comparison with other data.

- Of the six isotopes, the largest photofission cross section per nucleon is that for ^{237}Np.
- By comparing the ^{237}Np photofission cross section per nucleon with previous photoabsorption data on other nuclei we can tell that
  - The ^{237}Np photofission cross section is close, if not equal, to its photoabsorption cross section.

  - The concept of "universal behavior" is basically confirmed, within the limits of statistical and systematic uncertainties in the experimental data.

- The same comparison between fission and absorption for the other actinide nuclei shows that their fission cross sections are susstantially lower than their absorption cross sections. Thus, contrary to previous belief, the photofission reaction alone cannot be used as a substitute for the photoabsorption one.

- The nuclear-medium modifications of the Δ resonance produce, as expected, a lower and broader peak than the ones for the proton and the deuteron.

- The higher D_{13} and F_{15} resonances are not observed clearly in heavy nuclei, again as expected. However, there seems to be a slight increase in the cross sections for ^{237}Np, ^{235}U, and ^{nat}Pb, between about 0.5 and 1 GeV.

- Above the resonance region, the fission cross sections show a slowly decreasing energy dependence.

- If we assume that the fission probability for ^{237}Np is close to 100%, we can infer a shadowing effect starting below 1.5 GeV and slowly becoming more important with increasing energy.

Relative photofission cross sections per nucleon

The photofission cross sections relative to ^{237}Np show that

- The fission probability for ^{238}U after absorption of a photon having energy up to 4 GeV, often assumed to be equal to unity, is in fact only about 80% of that for ^{237}Np (with no strong dependence on the incident photon energy up to 4 GeV). This implies that, besides fission, there are other important competing processes taking place when a few-GeV photon interacts with an actinide nucleus. The same is true for two other uranium isotopes, but with a fissility of $\sim 85\%$.

- The almost flat energy dependence of the probability with which these heavy nuclei undergo fission indicates that a common mechanism is responsible for the photofission process, independent of whether the photon is in the few-GeV region or in the hundred-MeV region. This mechanism is described by the intranuclear-cascade-evaporation model.

- Insofar as the dependence of the relative cross sections on the fission parameter Z^2/A approaches an asymptotic value logarithmically, one can infer that the fission probability of ^{237}Np approaches unity.

8.2 Future plans

The directions for the future can be delimited into two categories, theoretical calculations and experimental work. In the near future, in collaboration with a theory group, Monte-Carlo calculations will be performed, based on the intranuclear cascade-evaporation model presented in Sec. 2.1. Using the formulas from Sec. 2.2 we aim to get theoretical estimates for the photofission cross sections for the six nuclei studied in this experiment. It would be interesting to see if these calculations will predict the same difference in fissility between neptunium and uranium and among the various uranium isotopes as has been found experimentally. Additionally, good agreement between the calculated and measured cross sections would validate the assumptions of the model.

We saw that our results invalidate the use of the photofission reaction alone to determine the total photoabsorption cross section for heavy nuclei. To do this, we would need to measure all the hadronic particles emitted after photoabsorption, and these measurements could be done using a thin-walled fission chamber placed inside the CLAS. Such a detailed investigation of all the exit channels following photoabsorption would lead to a much better understanding of the microscopic mechanism governing this process. Alternatively, a less complex experimental arrangement could be used at TUNL at energies up to 225 MeV.

Another experimental investigation is planned for the summer of 2001 at TUNL. The aim is to verify the results of the Novosibirsk measurements [Iva92] that report that a substantial fraction of the photofission events are accompanied by the emission of light and usually charged particles in the forward direction. The fraction of fission events in coincidence with these light forward particles ranges from $\sim 5\%$ at 50 MeV to $\sim 15\%$ at 6 GeV, while the QED calculations for the (γ, e^+e^-) process near 100 MeV predict this fraction to be a factor of 200 smaller. This experiment can be done using our existing equipment (fission-fragment detectors and reaction chamber) and the pair spectrometer available at TUNL.

Lastly, an approved experiment at the Gatchina synchrotron in St. Petersburg will measure the fission cross sections induced this time by *protons*. These measurements will provide accurate data for a variety of nuclei (two preactinides and six actinides), over a broad range of incident energies (from 0.2 to 1.0 GeV). Comparison with our results for photon-induced fission, as well as with intranuclear-cascade-evaporation calculations, will help us to understand the role of the incident probe, and ultimately will lead towards a better understanding of the microscopic mechanism governing the fission process.

Part III

Appendices

Appendix A

Correction for ^{238}U contamination

The expression 6.2 was derived under the asumption that, for the ^{235}U and ^{233}U targets, the measured fission cross section is a combination due to the contribution of both ^{235}U or ^{233}U and to the corresponding ^{238}U contamination, so that

$$\sigma_i^{meas} = C\, Y_i^{meas} \;\div\; \left(\frac{t_i}{A_i} + \frac{t_{238}}{A_{238}}\right) \tag{A.1}$$

where C is a normalization factor independent of the nature of the target material, and Y_i^{meas} is the measured fission-fragment yield. All the other symbols involved have the same meaning as in expression 6.2.

One can then express the measured yield Y_i^{meas} as the sum of the two yields, that is from the actual target and from its ^{238}U contamination

$$Y_i^{meas} = Y_i + Y_{238} \tag{A.2}$$

where

$$Y_i = \frac{\sigma_i}{C}\,\frac{t_i}{A_i} \tag{A.3}$$

$$Y_{238} = \frac{\sigma_{238}}{C}\,\frac{t_{238}}{A_{238}}\,. \tag{A.4}$$

By replacing the expressions A.2, A.4 and A.4 into A.1, one obtains the equivalent of the expression 6.2

$$\frac{\sigma_i}{A_i} = \frac{\sigma_i^{meas}}{A_i}\left(1 + \frac{t_{238}}{t_i}\frac{A_i}{A_{238}}\right) - \frac{\sigma_{238}}{A_{238}}\frac{t_{238}}{t_i} \; . \tag{A.5}$$

By writing A.1 as

$$\sigma_i^{meas} = \frac{C\;Y_i^{meas}}{t_i}\,\frac{1}{1 + \frac{t_{238}}{t_i}\frac{A_i}{A_{238}}} \tag{A.6}$$

and replacing it in A.5, we get

$$\frac{\sigma_i}{A_i} = \frac{C\;Y_i^{meas}}{t_i} - \frac{\sigma_{238}}{A_{238}}\frac{t_{238}}{t_i} \; . \tag{A.7}$$

which is the formula actually used for calculating the cross sections for ^{235}U and ^{233}U, using the previously determined ^{238}U cross section.

Appendix B

Statistical uncertainties for ^{nat}Pb

The fission-fragment yield per T-channel for ^{nat}Pb was obtained from the ADC spectra in the way described in Section 6.2.2. The corresponding statistical uncertainty per T-channel was derived as presented below.

The total number of counts Y^P in the ADC spectra corresponding to the coincidence peak before background subtraction (regions A + B in Fig. 6.4) for the seven lead targets is

$$Y^P = \sum_{i=1}^{7} N_i^P \tag{B.1}$$

$$\delta Y^P = \sqrt{\sum_{i=1}^{7} N_i^P} \tag{B.2}$$

where N_i^P are the count in the seven individual detectors. The total number of background counts Y^B under the coincidence peak (region B in Fig. 6.4) were obtained using the background counts N_i^B in the random region away from the coincidence peak (region C in Fig. 6.4), scaled by the factors S_i as defined in Section 6.2.2.

$$Y^B = \sum_{i=1}^{7} S_i N_i^B \tag{B.3}$$

$$\delta Y^B = \sqrt{\sum_{i=1}^{7} S_i^2 N_i^B} \tag{B.4}$$

Subtraction of the two quantities defined above gives the "prompt" yield Y from the lead targets, including the contribution of the Mylar backing foil.

$$Y = Y^P - Y^B = \sum_{i=1}^{7}(N_i^P - S_i N_i^B) \tag{B.5}$$

$$\delta Y = \sqrt{\sum_{i=1}^{7}(N_i^P + S_i^2 N_i^B)} \tag{B.6}$$

In a similar way, the peak X^P and background X^B yields are derived from the Mylar spectra, and then subtracted to give 'the 'prompt" yield X from the Mylar target.

$$X^P = M^P \tag{B.7}$$

$$\delta X^P = \sqrt{M^P} \tag{B.8}$$

$$X^B = S_{My} M^B \tag{B.9}$$

$$\delta X^B = \sqrt{S_{My}^2 M^B} \tag{B.10}$$

$$X = X^P - X^B = M^P - S_{My} M^B \tag{B.11}$$

$$\delta X = \sqrt{M^P + S_{My}^2 M^B} \tag{B.12}$$

Subtraction of Eqn. B.12, scaled by a factor of seven for the seven lead targets, from Eqn. B.6, gives the fission-fragment yield Y_{FF} per T-channel for ^{nat}Pb. Its associated statistical uncertainty δY_{FF} is obtained by adding in quadrature Eqn. B.6 and Eqn. B.12 scaled by seven.

$$Y_{FF} = Y - 7X \tag{B.13}$$

$$\delta Y_{FF} = \sqrt{\sum_{i=1}^{7}(N_i^P + S_i^2 N_i^B) + 7^2(M^P + S_{My}^2 M^B)} \tag{B.14}$$

Appendix C

Tables of absolute cross sections

	$(\sigma_{\gamma,F} \pm \delta\sigma_{\gamma,F})/A$ $(\mu b/nucleon)$		
E_γ (MeV)	^{233}U	^{235}U	^{238}U
193	193 ± 21	167 ± 11	177.4 ± 8.2
208	175 ± 20	194 ± 11	191.4 ± 8.1
235	273 ± 21	279 ± 12	237.8 ± 8.7
258	333 ± 23	302 ± 12	303.0 ± 9.2
282	350 ± 22	375 ± 12	358.8 ± 9.4
307	409 ± 25	409 ± 14	408.3 ± 10.7
337	406 ± 23	365 ± 12	394.4 ± 9.8
361	400.0 ± 9.2	400.2 ± 4.9	393.3 ± 3.6
376	381.9 ± 6.7	382.0 ± 3.5	368.0 ± 2.6
397	337.9 ± 6.5	357.5 ± 3.5	350.8 ± 2.5
414	357.1 ± 8.6	351.0 ± 4.5	329.0 ± 3.2
440	330.1 ± 8.4	311.0 ± 4.4	306.9 ± 3.2
454	308.4 ± 9.0	297.6 ± 4.7	289.3 ± 3.4
474	271.0 ± 6.2	275.7 ± 3.3	271.9 ± 2.4
494	269.4 ± 9.0	259.2 ± 4.7	246.9 ± 3.4
516	254.0 ± 5.4	250.5 ± 2.8	238.2 ± 2.0
543	217.8 ± 7.8	236.9 ± 4.1	221.4 ± 2.9
583	217.9 ± 4.2	213.6 ± 2.2	206.6 ± 1.6
650	191.9 ± 4.5	191.4 ± 2.3	184.5 ± 1.6
715	172.4 ± 2.9	183.5 ± 1.5	174.1 ± 1.1
765	169.6 ± 5.8	174.9 ± 2.4	165.2 ± 1.7
837	162.1 ± 2.8	163.2 ± 1.4	153.0 ± 1.0
908	158.5 ± 4.2	153.1 ± 2.1	144.0 ± 1.5
965	148.9 ± 3.6	142.9 ± 1.8	138.2 ± 1.3
1077	140.8 ± 3.2	134.2 ± 1.6	130.4 ± 1.1
1219	137.4 ± 2.8	124.3 ± 1.4	122.8 ± 1.0

	$(\sigma_{\gamma,F} \pm \delta\sigma_{\gamma,F})/A$ $(\mu b/nucleon)$		
E_γ (MeV)	^{233}U	^{235}U	^{238}U
1372	119.6 ± 3.1	116.2 ± 1.6	110.5 ± 1.1
1531	120.5 ± 3.4	108.1 ± 1.7	106.2 ± 1.2
1670	109.6 ± 4.4	96.9 ± 2.2	98.9 ± 1.6
1815	119.3 ± 5.9	100.0 ± 2.9	95.2 ± 2.1
1972	104.2 ± 5.0	98.7 ± 2.5	94.1 ± 1.8
2143	105.1 ± 5.7	89.0 ± 2.8	86.8 ± 2.0
2300	96.1 ± 6.3	101.5 ± 3.2	90.7 ± 2.2
2422	102.8 ± 8.5	86.8 ± 4.2	83.4 ± 3.0
2509	90.4 ± 7.5	83.7 ± 3.8	81.4 ± 2.7
2698	110.2 ± 8.4	86.1 ± 4.1	81.3 ± 2.9
2851	88.6 ± 5.9	90.2 ± 3.0	83.8 ± 2.1
3013	85.8 ± 8.0	85.2 ± 4.0	78.5 ± 2.8
3159	79.5 ± 6.3	79.3 ± 3.2	80.2 ± 2.2
3322	72.2 ± 7.9	85.5 ± 4.0	79.7 ± 2.8
3459	95.7 ± 8.6	77.9 ± 4.3	74.6 ± 3.0
3629	74.2 ± 7.6	77.3 ± 3.8	74.5 ± 2.6
3779	117.1 ± 8.2	82.0 ± 4.0	77.7 ± 2.8

Table C.1: Table of photon energies, absolute fphotofission cross sections per nucleon, and associated statistical uncertainties for ^{233}U, ^{235}U, and ^{238}U.

	$(\sigma_{\gamma,F} \pm \delta\sigma_{\gamma,F})/A$ $(\mu b/nucleon)$		
E_γ (MeV)	^{237}Np	^{232}Th	^{nat}Pb
193	188 ± 11	88.4 ± 4.6	7.3 ± 1.6
208	237 ± 11	113.8 ± 4.7	6.5 ± 0.9
235	309 ± 12	151.9 ± 5.1	10.2 ± 1.2
258	344 ± 13	191.6 ± 5.5	11.5 ± 1.2
282	448 ± 13	219.1 ± 5.6	17.6 ± 1.3
307	452 ± 15	237.3 ± 6.4	21.7 ± 1.6
337	464 ± 13	243.3 ± 5.9	23.8 ± 1.4
361	449.1 ± 5.0	236.3 ± 2.2	25.6 ± 0.6
376	429.2 ± 3.6	228.0 ± 1.6	24.8 ± 0.5
397	415.1 ± 3.6	214.5 ± 1.6	24.5 ± 0.5
414	395.3 ± 4.6	208.6 ± 2.0	23.1 ± 0.6
440	367.4 ± 4.6	192.3 ± 2.0	23.2 ± 0.6
454	345.0 ± 4.8	182.4 ± 2.1	21.0 ± 0.7
474	316.4 ± 3.4	164.3 ± 1.5	19.7 ± 0.5
494	310.0 ± 4.9	157.8 ± 2.1	18.7 ± 0.7
516	294.3 ± 2.9	151.3 ± 1.3	19.0 ± 0.4
543	267.1 ± 4.2	142.3 ± 1.8	17.5 ± 0.6
583	241.3 ± 2.3	130.1 ± 1.0	17.1 ± 0.3
650	220.1 ± 2.4	119.3 ± 1.0	15.7 ± 0.3
715	213.7 ± 1.6	107.3 ± 0.6	15.1 ± 0.2
765	208.7 ± 2.5	104.0 ± 1.0	14.9 ± 0.4
837	191.4 ± 1.5	91.5 ± 0.5	13.7 ± 0.2
908	183.2 ± 2.2	83.9 ± 0.7	12.7 ± 0.3
965	171.3 ± 1.9	82.9 ± 0.6	11.6 ± 0.3
1077	159.8 ± 1.7	75.0 ± 0.5	11.8 ± 0.2
1219	147.3 ± 1.5	71.0 ± 0.4	11.2 ± 0.2

	$(\sigma_{\gamma,F} \pm \delta\sigma_{\gamma,F})/A$ $(\mu b/nucleon)$		
E_γ (MeV)	^{237}Np	^{232}Th	^{nat}Pb
1372	136.7 ± 1.6	63.7 ± 0.5	9.9 ± 0.3
1531	130.6 ± 1.8	58.6 ± 0.5	9.4 ± 0.3
1670	124.9 ± 2.3	54.6 ± 0.6	9.4 ± 0.3
1815	124.3 ± 3.1	53.9 ± 0.7	8.7 ± 0.5
1972	120.2 ± 2.6	51.5 ± 0.6	8.5 ± 0.5
2143	115.3 ± 3.0	47.5 ± 0.7	8.0 ± 0.6
2300	120.3 ± 3.3	49.3 ± 0.8	7.5 ± 0.8
2422	115.3 ± 4.5	43.5 ± 1.0	7.7 ± 0.8
2509	97.5 ± 4.0	44.9 ± 0.9	9.1 ± 0.6
2698	105.5 ± 4.4	41.2 ± 1.0	7.4 ± 0.9
2851	108.7 ± 3.1	41.9 ± 0.7	8.4 ± 0.6
3013	104.9 ± 4.2	36.2 ± 0.9	7.5 ± 1.0
3159	92.5 ± 3.3	36.5 ± 0.8	7.2 ± 0.7
3322	97.8 ± 4.2	39.4 ± 1.0	6.9 ± 0.9
3459	95.9 ± 4.5	38.7 ± 1.0	7.9 ± 0.9
3629	93.4 ± 4.0	38.1 ± 0.9	9.0 ± 0.7
3779	102.5 ± 4.3	40.1 ± 1.0	7.7 ± 0.8

Table C.2: Table of photon energies, absolute cross sections per nucleon, and associated statistical uncertainties for ^{237}Np, ^{232}Th, and ^{nat}Pb.

Appendix D

Tables of relative cross sections

	$(\sigma_{\gamma,F} \pm \delta\sigma_{\gamma,F})/A$ relative to ^{237}Np		
E_γ (MeV)	^{233}U	^{235}U	^{238}U
218	0.86 ± 0.05	0.87 ± 0.04	0.81 ± 0.03
372	0.86 ± 0.01	0.88 ± 0.01	0.86 ± 0.00
476	0.87 ± 0.01	0.86 ± 0.01	0.83 ± 0.00
612	0.89 ± 0.01	0.88 ± 0.01	0.85 ± 0.01
769	0.82 ± 0.01	0.85 ± 0.01	0.81 ± 0.00
938	0.87 ± 0.02	0.83 ± 0.01	0.80 ± 0.01
1077	0.88 ± 0.02	0.84 ± 0.01	0.82 ± 0.01
1219	0.93 ± 0.02	0.84 ± 0.01	0.83 ± 0.01
1372	0.88 ± 0.03	0.85 ± 0.01	0.81 ± 0.01
1531	0.92 ± 0.03	0.83 ± 0.02	0.81 ± 0.01
1670	0.88 ± 0.04	0.78 ± 0.02	0.79 ± 0.02
1903	0.91 ± 0.03	0.81 ± 0.02	0.78 ± 0.02
2217	0.86 ± 0.04	0.81 ± 0.02	0.75 ± 0.02
2463	0.91 ± 0.06	0.80 ± 0.04	0.77 ± 0.03
2803	0.88 ± 0.05	0.83 ± 0.03	0.77 ± 0.02
3094	0.84 ± 0.06	0.84 ± 0.03	0.81 ± 0.03
3385	0.85 ± 0.07	0.85 ± 0.04	0.80 ± 0.03
3705	0.96 ± 0.06	0.81 ± 0.04	0.78 ± 0.03

Table D.1: Table of photon energies, photofission cross sections per nucleon relative to ^{237}Np, and associated statistical uncertainties for ^{233}U, ^{235}U, and ^{238}U.

	$(\sigma_{\gamma,F} \pm \delta\sigma_{\gamma,F})/A$ relative to ^{237}Np	
E_γ (MeV)	^{232}Th	^{nat}Pb
218	0.483 ± 0.017	0.031 ± 0.003
372	0.524 ± 0.004	0.056 ± 0.001
476	0.521 ± 0.003	0.062 ± 0.001
612	0.540 ± 0.005	0.071 ± 0.001
769	0.491 ± 0.003	0.071 ± 0.001
938	0.473 ± 0.005	0.068 ± 0.001
1077	0.469 ± 0.006	0.074 ± 0.002
1219	0.482 ± 0.006	0.076 ± 0.002
1372	0.466 ± 0.007	0.072 ± 0.002
1531	0.449 ± 0.007	0.072 ± 0.003
1670	0.437 ± 0.009	0.075 ± 0.003
1903	0.431 ± 0.008	0.071 ± 0.003
2217	0.411 ± 0.009	0.067 ± 0.004
2463	0.410 ± 0.013	0.079 ± 0.005
2803	0.387 ± 0.011	0.075 ± 0.005
3094	0.372 ± 0.012	0.075 ± 0.006
3385	0.403 ± 0.015	0.076 ± 0.007
3705	0.399 ± 0.014	0.086 ± 0.006

Table D.2: Table of photon energies, cross sections per nucleon relative to ^{237}Np, and associated statistical uncertainties for ^{232}Th and ^{nat}Pb.

References

[Ade88] G. D. Adeev *et al.*, Sov. J. Part. Nucl. **19**, 529 (1988).

[Ahr84] J. Ahrens *et al.*, Phys. Lett. **B146**, 303 (1984).

[Ahr85a] J. Ahrens, Nucl. Phys. **A446**, 229c (1985).

[Ahr85b] J. Ahrens and J.S. O'Connell, Comments Nucl. Part. Phys. **14**, 245 (1985).

[Ang93] M. Anghinolfi *et al.*, Phys. Rev. C **47**, 922 (1993).

[Ara90] E. A. Arakelyan *et al.*, Sov. J. Nucl. Phys. **52**, 878 (1990).

[Arm72] T. A. Armstrong *et al.*, Phys. Rev. D **5**, 1640 (1972) and Nucl. Phys. **B41**, 445 (1972).

[Arr81] J. D. T. Arruda-Neto *et al.*, Nucl. Instrum. Methods **190**, 203 (1981).

[Arr86] J. D. T. Arruda-Neto, *Notes on the theory of parallel plate avalanche detectors*, Linac Tech Note 86-56, Nucl. Phys. Lab., Univ. of Illinois at Urbana-Champaign (1986).

[Arr90] J. D. T. Arruda-Neto *et al.*, Phys. Rev. C **41**, 354 (1990).

[Arr95] J. D. T. Arruda-Neto, A. Deppman, N. Bianchi, and E. De Sanctis, Phys. Rev. C **51**, 751 (1995).

[Bau78] T. H. Bauer *et al.*, Rev. Mod. Phys. **50**, 261 (1978).

[Ber86] B. L. Berman *et al.*, Phys. Rev. C **34**, 2201 (1986).

[Ber92] B. L. Berman *et al.*, CLAS Note 92-010 (1992).

[Bia93a] N. Bianchi *et al.*, Phys. Lett. **B299**, 219 (1993).

[Bia93b] N. Bianchi *et al.*, Phys. Rev. C **48**, 1785 (1993).

[Bia96] N. Bianchi *et al.*, Phys. Rev. C **54**, 1688 (1996).

[Bia99] N. Bianchi *et al.*, Phys. Rev. C **60**, 064617 (1999).

[Bla75] M. Blann, Ann. Rev. Nucl. Sci. **25**, 123 (1975).

[Bla83] M. Blann, B. L. Berman, and T. T. Komoto, Phys. Rev. C **28**, 2286 (1983).

[Bof96] S. Boffi, Ye. Golubeva, L. A. Kondratyuk, and M. I. Krivoruchenko, Nucl. Phys. **A606**, 421 (1996).

[Boh39a] N. Bohr, Phys. Rev. **55**, 418 (1939).

[Boh39b] N. Bohr and J. Wheeler, Phys. Rev. **56**, 426 (1939).

[Bon95] J. P. Bondorf *et al.*, Phys. Rep. **257**, 133 (1995).

[Bot88] A. S. Botvina, A. S. Iljinov, and J. N. Mishustin, Phys. Lett. **B205**, 421 (1988).

[Bot90] A. S. Botvina, A. S. Iljinov, and J. N. Mishustin, Nucl. Phys. **A507**, 649 (1990).

[Bre77] A. Breskin and N. Zwang, Nucl. Instrum. Methods **144**, 609 (1977).

[Bro69] S. J. Brodsky and J. Pumplin, Phys. Rev. **182**, 1794 (1969).

[Bro73] G. R. Brooks *et al.*, Phys. Rev. D **8**, 2826 (1973).

[Bun80] E. Bunakov, Part. Nucl. **11**, 1285 (1980).

[Cal80a] J. T. Caldwell *et al.*, Phys. Rev. C **21**, 1215 (1980).

[Cal80b] J. T. Caldwell *et al.*, Nucl. Sci. Eng. **73**, 153 (1980).

[Car84] P. Carlos *et al.*, Nucl. Phys. **A431**, 573 (1984).

[Car85] P. Carlos, in *Proc. of the Int. School of Intermediate Energy Nucl. Phys.*, Verona, 1985, World Scientific, Singapore (1985).

[Car92] R. C. Carrasco and E. Oset, Nucl. Phys. **A536**, 445 (1992).

[Cet00] C. Cetina *et al.*, Phys. Rev. Lett. **84**, 5740 (2000).

[Cho83] C. Chollet *et al.*, Phys. Lett. **B127**, 331 (1983).

[Chr52] J. Christiansen, Z. Angew. Phys. **4**, 326 (1952).

[Dep96] A. Deppman, J. D. T. Arruda-Neto, E. De Sanctis, and N. Bianchi, Nuovo Cimento A **109**, 1197 (1996).

[Dis76] P. Distas and G. Shaw, Nucl. Phys. **B113**, 246 (1976).

[Dre84] J. Drexler *et al.*, Nucl. Instrum. Methods **220**, 409 (1984).

[Eck90] E.-M. Eckert *et al.*, Phys. Rev. Lett. **64**, 2483 (1990).

[Fal00] T. Falter, S. Leupold, and U. Mosel, Phys. Rev. C **62**, 031602 (2000).

[Fro92] Th. Frommhold *et al.*, Phys. Lett. **B295**, 28 (1992).

[Fro94] Th. Frommhold *et al.*, Z. Phys. A **350**, 249 (1994).

[Gar86] P. Garganne, Note CEA-N-2492, Centre d'Etudes Nucleaires de Saclay (1986).

[Gav87] A. Gavron *et al.*, Phys. Rev. C **35**, 579 (1987).

[Gia94] M. M. Giannini and E. Santopinto, Phys. Rev. C **49**, R1258 (1994).

[Gri66] J. J. Griffin, Phys. Rev. Lett. **17**, 478 (1966).

[Got69] K. Gottfried and D. R. Yennie, Phys. Rev. **182**, 1595 (1969).

[Gua87] C. Guaraldo *et al.*, Phys. Rev. C **36**, 1027 (1987).

[Hah39] O. Hahn and F. Strassmann, Naturwiss. **27**, 11 (1939).

[Hem75] G. Hempel *et al.*, Nucl. Instrum. Methods **131**, 445 (1975).

[Hey71] V. Heynen, H. Meyer, B. Naroska, and D. Notz, Phys. Lett. **34B**, 651 (1971).

[Hof94] P. Hofmann *et al.*, Phys. Rev. C **49**, 2555 (1994).

[Ign75] A. V. Ignatyuk, G. N. Smirenkin, and A. S. Tishin, Yad. Fiz. **21**, 485 (1975).

[Ilj89] A. S. Iljinov *et al.*, Phys. Rev. C **39**, 1420 (1989).

[Ilj92a] A. S. Iljinov *et al.*, Nucl. Phys. **A539**, 263 (1992).

[Ilj92b] A. S. Iljinov *et al.*, Nucl. Phys. **A543**, 517 (1992).

[Ilj94] A. S. Iljinov, M. V. Kazarnovsky, and E. Ya. Paryev, *Intermediate Energy Nuclear Physics*, CRC Press, Boca Raton (1994).

[Ilj97] A. S. Iljinov *et al.*, Nucl. Phys. **616**, 575 (1997).

[Iva92] D. I. Ivanov *et al.*, Sov. J. Nucl. Phys. **55**, 1 (1992).

[Kit68] K. Kituchi and M. Kawai, *Nuclear Matter and Nuclear Reactions*, North Holland, Amsterdam (1968).

[Kno82] J. W. Knowles *et al.*, Phys. Lett. **116B**, 315 (1982).

[Lep87] A. Leprêtre *et al.*, Nucl. Phys. **A472**, 553 (1987).

[Luc89] V. Lucherini *et al.*, Phys. Rev. C **39**, 911 (1989).

[Mac96] M. MacCormick *et al.*, Phys. Rev. C **53**, 41 (1996).

[Mac97] M. MacCormick *et al.*, Phys. Rev. C **55**, 1033 (1997).

[Mar90] J. B. Martins *et al.*, Phys. Rev. C **44**, 354 (1990).

[Meu39] L. Meitner and O. R. Frisch, Nature (London) **413**, 239 (1939).

[Mic77] S. Michalowski *et al.*, Phys. Rev. Lett. **39**, 737 (1977).

[Muc99] V. Muccifora *et al.*, Phys. Rev. C **60**, 064616 (1999).

[Owe90] R. O. Owens, Nucl. Instrum. Methods **A288**, 574 (1990).

[Pil95] G. Piller, W. Ratzka, and W. Weise, Z. Phys. A **352**, 427 (1995).

[Rae64] H. Raether, *Electron Avalanches and Breakdown in Gases*, Butterworths, London (1964).

[Rie84] H. Ries *et al.*, Phys. Lett. **139B**, 254 (1984).

[San98] J. C. Sanabria, private communication.

[San00a] J. C. Sanabria *et al.*, Nucl. Instrum. Methods **A441**, 525 (2000).

[San00b] J. C. Sanabria *et al.*, Phys. Rev. C **61**, 034604 (2000).

[San00c] J. C. Sanabria *et al.*, Nucl. Instrum. Methods (in press).

[Sha96] G. Shaw, Phys. Rev. D **47**, R3676 (1996).

[Sob98] D. I. Sober, private communication.

[Sob00] D. I. Sober *et al.*, Nucl. Instrum. Methods **A440**, 263 (2000).

[Spe83] H. J. Specht, Nucl. Phys. **A440**, 430 (1983).

[Van73] R. Vandenbosch and J. R. Huizenga, *Nuclear Fission*, Academic Press, New York (1973).

[Wei74] W. Weise, Phys. Rep. **13**, 53 (1974).